Review

Jolly Xavier*, Deshui Yu*, Callum Jones, Ekaterina Zossimova and Frank Vollmer*

Quantum nanophotonic and nanoplasmonic sensing: towards quantum optical bioscience laboratories on chip

https://doi.org/10.1515/nanoph-2020-0593
Received November 2, 2020; accepted February 3, 2021;
published online March 4, 2021

Abstract: Quantum-enhanced sensing and metrology pave the way for promising routes to fulfil the present day fundamental and technological demands for integrated chips which surpass the classical functional and measurement limits. The most precise measurements of optical properties such as phase or intensity require quantum optical measurement schemes. These non-classical measurements exploit phenomena such as entanglement and squeezing of optical probe states. They are also subject to lower detection limits as compared to classical photodetection schemes. Biosensing with non-classical light sources of entangled photons or squeezed light holds the key for realizing quantum optical bioscience laboratories which could be integrated on chip. Single-molecule sensing with such non-classical sources of light would be a forerunner to attaining the smallest uncertainty and the highest information per photon number. This demands an integrated non-classical sensing approach which would combine the subtle non-deterministic measurement techniques of quantum optics with the device-level integration capabilities attained through nanophotonics as well as nanoplasmonics. In this back drop, we review the underlining principles in quantum sensing, the quantum optical probes and protocols as well as state-of-the-art building blocks in quantum optical sensing. We further explore the recent developments in quantum photonic/plasmonic sensing and imaging together with the potential of combining them with burgeoning field of coupled cavity integrated optoplasmonic biosensing platforms.

Keywords: biosensors; nanophotonics; plasmonics; quantum optics; quantum photonics; quantum sensing.

1 Introduction—quantum-optical bioscience on a chip

Biosensing and information processing with non-classical quantum optical devices using entangled photons or squeezed light hold the key for realizing quantum optical bioscience devices which could be integrated and miniaturized to chip level. Single-molecule sensing with such non-classical sources of light would be a forerunner to attaining the unprecedented detection limit and the highest information per photon number. It would enable one to realize compact, highly precise and non-invasive probing tools for fragile biomolecules which are often photosensitive with ultralow photo-thermal damage thresholds [1, 21]. Nature probably already holds very peculiar examples of fundamental biological processes involving quantum mechanical principles. In the recent past, there has been a keen interest to unravel the role played by quantum mechanics and quantum phenomena operating as decisive mechanisms in simple and complex biological processes (see Box 1). Though these studies, inferences and speculations are debated by and large within the scientific community, they also shed light to explore the fundamental mechanisms behind these phenomena and how they could be mimicked to develop novel quantum technologies for sensing and metrology. In his lecture series *What is Life*, Schrödinger in a way gives a foretaste of the molecular basis of heredity, predicting the functional features of DNA [18]. Glimpses of a few non-classical quantum processes which are inferred to play a crucial role behind

Jolly Xavier, Deshui Yu, Callum Jones, Ekaterina Zossimova, and Frank Vollmer contributed equally to this work.

***Corresponding authors: Jolly Xavier, Deshui Yu, and Frank Vollmer**, Department of Physics and Astronomy, Living Systems Institute, University of Exeter, EX4 4QD, Exeter, UK,
E-mail: j.xavier@exeter.ac.uk (J. Xavier), d.d.yu@exeter.ac.uk (D. Yu), f.vollmer@exeter.ac.uk (F. Vollmer). https://orcid.org/0000-0001-8931-9365 (J. Xavier)
Callum Jones and Ekaterina Zossimova, Department of Physics and Astronomy, Living Systems Institute, University of Exeter, EX4 4QD, Exeter, UK

Box 1

Quantum mechanical phenomena and processes in the biological world

One wonders how this biological world comprising of so called warm, wet and noisy environments with fluctuating spatial background and large time scale events could support very subtle and controlled quantum mechanical processes such as quantum tunnelling and entanglement. Given this dilemma, as quantum nanophotonic sensing would make use of quantum coherent states and the underlying principles to surpass the limits of classical approaches, it will be worthwhile to explore whether nature uses such quantum mechanical processes in realizing unprecedented efficiency in some of the most basic biological events (Figure 1). This ranges from photosynthesis to enzyme catalysis and even to the magnetoreception of Earth's magnetic field by birds for their meticulous annual navigation [2–5]. Understanding the link between natural biological processes and their non-trivial quantum effects will also unfold different probes to develop effective non-classical sensing schemes and an insight into the different variables involved. The mathematical physicist and Nobel laureate Sir Roger Penrose hypothesizes that quantum mechanics plays a role in understanding our brain and human consciousness [6]. Some photoreceptor biomolecules such as the visual opsins even respond to single photons with a conformational change that is speculated as triggering a signalling cascade in our brain [7]. Considering atoms and ions as constituent materials with definite equilibrium properties governed by quantum principles and phenomena, all animate as well as inanimate materials could be considered as quantum mechanical in its fundamental sense [8]. The crux lies in understanding and connecting the macroscopic length and time scales of biological events to their microscopic counterparts in the quantum world. So, one has to rely on quantum dynamical processes at the molecular level and the involved interplay between respective time and length scales in quantum biology [4, 8].

One of the very prominent biological processes is enzyme catalysis which is central to cellular functioning. The conventional understanding of enzyme catalysis lies in the process of proteins lowering the activation energy in order to surpass the low reaction rates of biochemical reactions [2]. But recent studies highlight the possibility of quantum tunnelling in enzyme-catalysed multiple-hydrogen transfer by means of coupling of electrons and protons to control the charge transport [2, 9, 10] (Figure B1a). The radical pair mechanism in avian magnetoreception is another area of biological processes looking for a quantum explanation [2, 11, 12]. As shown in Figure B1b, the process is thought to be occurring within cryptochromes which are proteins residing in the retina of birds such as the European Robin. The process of using a quantum coherent compass in migrating birds is initiated by the photoexcitation causing electron transfer and radical pair formation, subsequently the singlet and triplet electron spin states interconvert due to external and internal magnetic couplings [2, 13]. Thereafter, the singlet and triplet radical pairs recombine into biologically observable singlet and triplet products [2]. In a very interesting observation Cai et al. noted that the relation between quantum coherence or entanglement and the magnetic field sensitivity has high significance when radical pair life time is not long enough in comparison to the coherence time or else it has less relevance [14]. This makes one to speculate the possible interplay between quantum coherence and the environmental noise as a decisive factor to play a crucial role behind the exemplary magnetic sensitivity in the avian compass [4].

The primary stage of photon harvesting in plants (Figure B1c) and certain microbes is another interesting biological process where quantum coherence is explored to understand the near 100% quantum yield in the electron generation at the reaction centre for every photon absorbed and transferred by the light harvesting antenna [2, 3, 15, 16]. It was Fleming and co-workers who in 2007 demonstrated the quantum coherent energy transfer in the Fenna–Matthews–Olson (FMO) complex of green sulphur bacteria [15]. The recent studies on two-dimensional electronic spectroscopy have shed light on quantum mechanical excitation energy transfer as one of the possible mechanisms by probing the decay of coherent superpositions of vibrational and vibronic states of light harvesting complexes (Figure B1d).

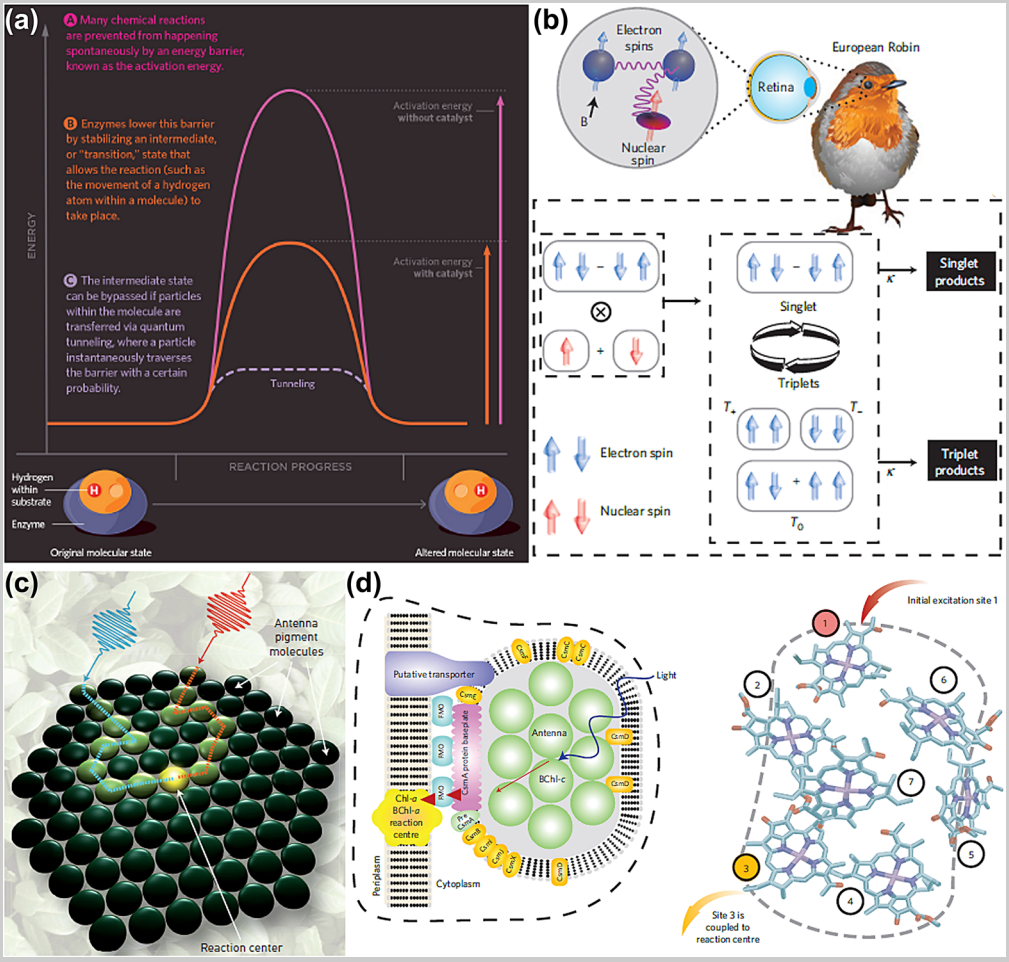

Figure B1: (a) Schematic of enzyme catalysis process with possible quantum tunnelling as an activation energy lowering mechanism. Adapted with permission from Lucy Reading-Ikkanda from the study by Offord [10]. (b) The schematic of the avian quantum compass involving the possible radical-pair mechanism in avian magnetoreception in birds such as European robin. Reprinted by permission from Springer Nature: Nature Physics [2], copyright (2012). (c) A semiclassical scheme of the route of an exciton towards the reaction centre where the exciton is stimulated by a photon from sunlight. The coherence observed in two-dimensional spectroscopy experiments points to the quantum picture in the primary stage of photosynthesis process involving electronic vibrational resonances facilitating the energy transfer. Adapted with permission from Phil Saunders from the study by Wills [17]. (d) FMO complex in the light-harvesting apparatus of green-sulphur bacteria shows signatures of quantum coherent energy transfer. Left: The photosynthetic apparatus depicting its antenna, energy-conducting baseplate and FMO complexes, as well as reaction centre. Right: An X-ray diffraction diagram of the BChl-a arrangements of one of the FMO pigment-protein complexes. Reprinted by permission from Springer Nature: Nature Physics [2], copyright (2012).

some of the very fundamental biological processes are schematically shown in Figure 1 [2, 17]. Inspired by this intriguing sensing and processing found in nature, the application of quantum light and information processing in quantum-enhanced single-molecule sensors would allow us to build biosensors that operate at possible fundamental limits of detection. The analysis of photon-correlations could be applied to reveal new functional information about living matter and biophotons. Single-photon correlations have already been used to improve image contrast at low light intensity [19, 20].

Classical optical measurements are ultimately limited to uncertainties scaling as $1/\sqrt{N}$ (the shot-noise limit), where N is the number of photons used to probe a system, whereas non-classical quantum metrology schemes for instance with path entangled photons are envisaged to attain $1/N$ scaling [1, 21]. Although quantum metrology schemes often work with precisely constructed optical states of relatively few photons, even high intensity states can be squeezed so that fluctuations in a given quadrature are reduced below the vacuum level. The second-generation LIGO gravitational wave

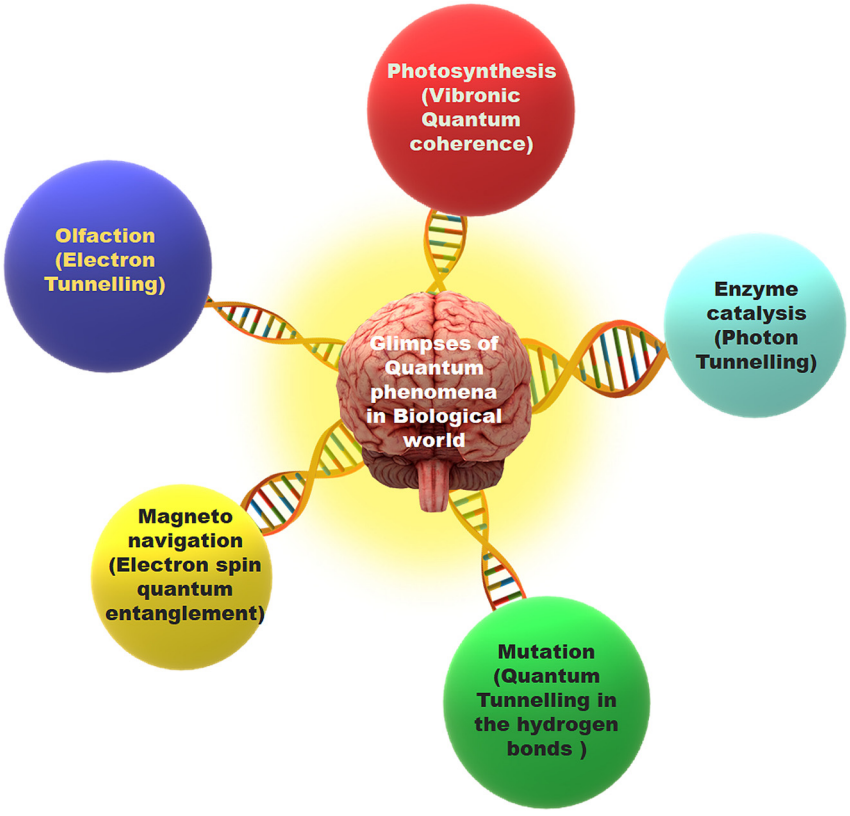

Figure 1: A few prominent biological functions and their correspondingly studied underlying quantum processes/phenomena [17].

detectors use non-classical squeezed light interferometry in combination with other advanced optical techniques in order to measure the displacements on the order of $10^{-21} m/\sqrt{\text{Hz}}$ at 100 Hz, a length scale of the order of less than a billionth of atomic dimension $\sim 10^{-10}$ m [22, 23]. On the other hand, there has been unprecedented progress in the field of integrated quantum technologies in the recent past [24]. Integrated quantum chips began with a simple demonstration of a single logic operation of quantum interference and controlled-NOT gate operating on a single qubit [25]. Within a decade, it has made a quantum leap by demonstrating both multi-dimensional quantum entanglement realized in a large-scale integrated chip [26] as well as on-chip multiphoton entanglement of multi-qubit operation in a reprogrammable linear-optic quantum circuit [27]. Due to the recent advances in demonstrating single, heralded and entangled photon sources as well as the availability of many different low-noise single photon detectors and cameras, quantum optical measurement techniques are becoming more prominent and they are entering new application areas. One of the very exciting new areas for the application of quantum imaging and sensing is biology and biosensing.

To achieve the vision of quantum optical bioscience laboratories on chip will require a sustained and multi-disciplinary research effort. It requires integration of single photon sources with single-molecule sensors and single photon detectors on micro- and nano-structured biochips. It requires the application of advanced optical measurement techniques together with quantum optical measurement protocols to probe various forms of biologically and/or optically active biomatter, as well as single biomolecules in their various functional forms in a suitable (liquid) environment. It requires the application of advanced nano-chemical techniques to spatially and temporally control chemical activity at the level of single molecules and single photons. It requires advances in biophysics to link classical biophysical methods, models and mechanisms to novel, non-classical probing of biophysical activities observed at the levels of single photons and single biomolecular states. It will require the application of quantum-optical analysis techniques to light emitted by biomatter and single molecules in particular. The aim of this review is to provide

researchers entering into this exciting multi-disciplinary field with an overview of the state-of-the-art in the various areas of quantum optics research that will need to come together to apply quantum optical methods to biological systems. We will review the areas of research that we have identified as the most relevant for achieving quantum optical bioscience laboratories on a chip: quantum optics, single molecule techniques, nanophotonics and plasmonics, and quantum mechanics of biomatter.

2 Quantum sensing underlying principles and protocols

Current biosensing applications mainly make use of the direct/indirect interface between light waves and the *static* dipole moment of biomolecules, where the presence/absence of single biomolecules perturbs the dynamics of the light field. Such a far-off-resonance coupling is weak, limiting the sensitivity. Replacing the static dipole moment with a *dynamic* one, i.e., the electric dipole transition between two electronic states, can significantly enhance the light–molecule interaction under the resonant-coupling condition. In addition, for sensing at the ultimate single-molecule level, one biomolecule or photon added to or removed from the system may give rise to an apparent variance in energy. Consequently, quantum effects must be taken into account, leading to quantum sensing [28]. The classical/quantized electromagnetic field interacting with the dipole transitions of quantum emitters is the central topic of *Quantum Optics*.

2.1 Quantum sensing protocol

Quantum sensing makes use of features of quantum mechanics, such as quantized energy levels, the superposition principle and entanglement, to measure a physical quantity or enhance measurement sensitivity beyond the classical limit. The sensing process involves an object, a detector and a readout system, where the detector interacts with the object and generates a response signal that is measured by the readout device. The size of the object may vary from microscopic (single quantum emitters like atoms, ions, molecules, quantum dots and nitrogen-vacancy centres, and light quanta/photons) to universal (e.g. the gravitational wave produced by the collision of two black holes) in scale. The detectors could be either classical (such as microwaves, optical light and cavities/resonators) or quantum (for instance: internal energy levels of emitters, quantum states of superconducting circuits, and non-classical properties of light). The response signal from the detector must be converted into a physical quantity that is measurable to the readout system. For example, the population of emitters in a certain internal state is indirectly measured by mapping it onto the light power (the number of photons) that can be read out by a photodetector.

As illustrated in Figure 2, the quantum sensing process has three typical steps [28]: **(i) Preparation.** Due to the nature of quantum mechanics, the full picture of a physical observable associated with the object cannot be captured via a single measurement. Only the expectation value of the observable is meaningful to the measurement. Thus, the detection process should be performed repeatedly under the same preparation conditions many times; **(ii) Interaction.** Ideally, the detector interacts with the object in a coherent way and the wave function of the coupled system is predictable via the Schrödinger equation. However, in practice, the coherent object-detector interaction is inevitably interrupted by environmental fluctuations, limiting the detection speed and accuracy. Hence, the object-detector coupling strength should be large enough that an efficient response signal is obtained well before the dissipation takes effect; and **(iii) Measurement.** Fundamental fluctuations are unavoidable and influence the readout outcomes, for which the signal-to-noise ratio must be sufficiently high. Quantum noise, such as photon shot noise and quantum projection noise of emitters, imposes the standard quantum limit (SQL, which scales as $1/\sqrt{N}$ with the number N of photons or emitters) on measurements [1, 30, 31]. Entangling a small quantum system with a large one can efficiently suppress the SQL by means of quantum non-demolition (QND) measurements [32]. Moreover, the SQL of a quantum system composed of N emitters may be overcome by using entangled states of emitters [33–35]. The ultimate uncertainty of measurements arises from Heisenberg's uncertainty principle and scales as $1/N$ [36, 37].

2.2 Measurement of photon characteristics

Environmental perturbations inevitably influence the phase ϕ_L (frequency ω_L) and number N_p (intensity) of light quanta. Mapping the photon state onto the density matrix, fluctuation in ϕ_L (ω_L) is related to the non-diagonal elements, which primarily determine the so-called coherence (temporal/spatial correlation) of photons. Enhancing the coherence generally relies on a feedback control loop. In

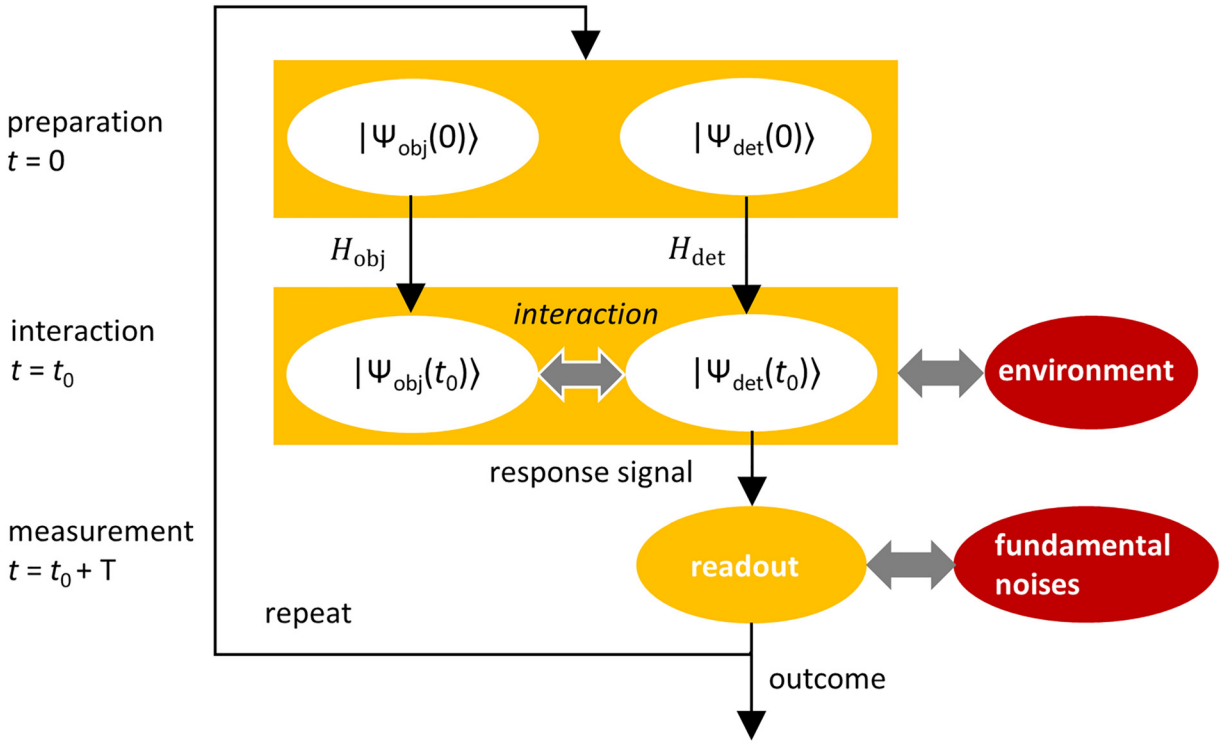

Figure 2: Quantum sensing process.
The object and detector are isolated and initialized in the known states $|\psi_{obj}(0)\rangle$ and $|\psi_{det}(0)\rangle$, respectively, at $t = 0$. Then, the two states evolve freely for a time duration t_0 and arrive at the prepared states $|\psi_{obj}(t_0)\rangle = e^{-iH_{obj}t/\hbar}|\psi_{obj}(0)\rangle$ and $|\psi_{det}(t_0)\rangle = e^{-iH_{det}t/\hbar}|\psi_{det}(0)\rangle$ with the respective Hamiltonians H_{obj} and H_{det}. Afterwards, the detector interacts with the object for a duration T. The inevitable environmental fluctuations interrupt the coherent object–detector interaction. Finally, the response signal produced by the detector is measured by a readout device, whose sensitivity is fundamentally limited by quantum mechanics. The sensing process needs to be performed repeatedly to obtain the expectation value of the associated physical observable. Adapted from the study by Vollmer and Yu [29].

contrast, fluctuation in N_p mainly affects the diagonal elements. Flying single photons enable quantum communication between remotely separated objects. However, fluctuations in ϕ_L and N_p strongly restrict the fidelity of quantum information processing (QIP). Various methods have been exploited to measure both ϕ_L and N_p [1, 21, 28].

Measuring the photon phase ϕ_L: Generally, we measure the light frequency ω_L, instead of ϕ_L, by using a frequency reference which possesses a higher stability and accuracy. The mostly common references are optical resonators. By applying the well-known Pound-Drever-Hall technique [38], the light coherence time can be extended to over 10^2 s, as shown in the reported studies [39, 40]. However, the resonator's long-term frequency drift limits the measurement of the slowly varying fluctuation components in ϕ_L. To address this issue, the transition between two internal states of quantum emitters, such as atoms and ions, is usually applied as the frequency reference since the interstate energy spacing is determined by nature. The light beam is coupled to a pair of emitters' internal states, inducing the emitters to transfer between these two states, i.e. Rabi oscillation. The fluctuation in ω_L can be derived from measuring the population distribution of emitters. Two approaches, Rabi and Ramsey [41] measurements, are commonly used in the modern optical detection. The sensitivity of such an emitter-population measurement is eventually limited by quantum mechanical principles, i.e. the so-called quantum projection limit (QPL), which is proportional to $1/\sqrt{N_e}$ with the number of quantum emitters N_e (see Box 2). It is worth noting that the QPL can be mitigated down to the fundamental Heisenberg limit ($\propto 1/N_e$) by using entangled emitters [47]. The population distribution of emitters needs to be converted into a measurable physical quantity, which is usually the light power (i.e. photon number). The standard quantum limit to photon detection is the so-called shot noise, leading to the measurement sensitivity scaling as $1/\sqrt{N_p}$. In many cases, the light signal is too weak to be measured. Homodyne and heterodyne methods [30], where the weak signal is mixed with a strong local oscillating wave, are generally applied to enhance the signal-to-noise ratio. The fundamental limit of photon-phase measurements is also set by the

Box 2

Measurement limit

Quantum projection noise (QPN) limit. The fundamental limit on the measurement precision based on the resonant light-emitter interaction should be determined by the quantum emitter itself. For a two-level emitter, which is initially prepared in the ground state $|g\rangle$, its wave function at the time t is given by $|\Psi(t)\rangle = \cos\frac{\Omega t}{2}|g\rangle - i\sin\frac{\Omega t}{2}|e\rangle$. The probability of the emitter in the excited state $|e\rangle$ is associated with the observable operator $P_e = |e\rangle\langle e|$, which projects $|\Psi(t)\rangle$ onto $|e\rangle$. Indeed, the measurement result obtained in experiment corresponds to the expectation value $\langle P_e\rangle = \langle\Psi(t)|P_e|\Psi(t)\rangle = \sin^2\frac{\Omega t}{2}$. The optimal measurement point is located at the maximum-slope spot, $\langle P_e\rangle = 1/2$, i.e. the $\pi/2$-pulse. However, this is only a part of story since the quantum mechanics imposes a variance in the measurement, $(\Delta P_e)^2 = \langle(P_e - \langle P_e\rangle)^2\rangle = \langle P_e\rangle(1 - \langle P_e\rangle)$. The maximum uncertainty also occurs at $\langle P_e\rangle = 1/2$ while $(\Delta P_e)^2$ is minimized at $\langle P_e\rangle = 0$ or 1. The similar result holds for the system composed of N_e independent emitters. The measurement signal is proportional to $N_e\langle P_e\rangle$ while the QPN is $\sqrt{N_e\langle P_e\rangle(1-\langle P_e\rangle)}$, resulting in $(S/N)^{-1} = 1/\sqrt{N_e}$ with $\langle P_e\rangle = 1/2$ [42]. This QPN limit has been proven in experiment [31], and the stability of single-ion clocks has already hit on the QPN limit [43].

Shot noise limit. In photodetection, the incident light (frequency ω_L) power is given by $P = IA$ with the light beam's intensity I and area A. The photodetector converts the optical signal into the current signal $i_0 = ge\eta(P/\hbar\omega_L)$ with the gain g and the quantum efficiency η. The noise in photodetector fluctuates the current around i_0, i.e. $i(t) = i_0 + \Delta i(t)$ with $\langle\Delta i(t)\rangle = 0$. The rms (root mean square) noise current consists of two main parts: the shot noise given by Schottky formula $\overline{i_{\rm sn}^2} = 2egi_0\Delta f$ and the thermal noise power $\overline{i_{\rm th}^2} = (4k_BT/R)\Delta f$ with the detection circuit's bandwidth Δf, temperature T and input impedance R. In the limit of $\overline{i_{\rm sn}^2} \gg \overline{i_{\rm th}^2}$, one obtains the measurement sensitivity $(S/N)^{-1} = \overline{i_{\rm sn}^2}/i_0^2 = 1/\sqrt{N_p}$ with $\eta = 1$ and the number of collected photons $N_p = (P/\hbar\omega_L)\Delta t$ within the integration time $\Delta t = 1/2\Delta f$. Another measurement limit which is commonly discussed is the **quantum noise limit**. While the shot noise limit defines the best possible sensitivity in a perfect ($\eta = 1$) setup, the quantum noise limit gives the achievable sensitivity for a given experiment with a total quantum efficiency η_{tot} along the optical path, including detector efficiency. This sensitivity is $(S/N)^{-1} = 1/\sqrt{\eta_{tot}N_p}$ [1].

Heisenberg Limit. The phase estimation may be implemented from the atomic spectroscopy. An N_e-emitter system is initially prepared in the fully-entangled GHZ state $|\Psi_{in}\rangle = (|g,g,\ldots,g\rangle + |e,e,\ldots,e\rangle)/\sqrt{2}$. The unitary rotation operator $U = \prod_{i=1}^{N_e}\otimes\exp[(i\varphi/2)\sigma_z^{(i)}]$ is applied on $|\Psi_{in}\rangle$, resulting in $|\Psi_{out}\rangle = U|\Psi_{in}\rangle = (e^{-iN_e\varphi/2}|g,g,\ldots,g\rangle + e^{iN_e\varphi/2}|e,e,\ldots,e\rangle)/\sqrt{2}$. The elements of a positive operator valued measure (POVM) [44] are chosen as $E_+ = |+\rangle\langle+|$ and $E_- = |-\rangle\langle-|$ with $|+\rangle = (|g,g,\ldots,g\rangle + |e,e,\ldots,e\rangle)/\sqrt{2}$ and $|-\rangle = (|g,g,\ldots,g\rangle - |e,e,\ldots,e\rangle)/\sqrt{2}$, satisfying the realtion $E_+ + E_- = 1$. The probability distribution is caculated to be $p(+|\varphi) = \langle E_+\rangle = \cos^2(N_e\varphi/2)$ and $p(-|\varphi) = \langle E_-\rangle = \sin^2(N_e\varphi/2)\neq$. The so-called quantum Fisher information $F(\varphi)$ [45] is then derived as $F(\varphi) = p^{-1}(+|\varphi)[\partial p(+|\varphi)/\partial\varphi]^2 + p^{-1}(-|\varphi)[\partial p(-|\varphi)/\partial\varphi]^2 = N_e^2$. The minimal standard deviation of the phase meassurement is given by the quantum Cramér-Rao bound [37] $\delta\varphi = 1/\sqrt{\nu F(\varphi)}$, where ν denotes the measurement times. Setting = 1 , i.e. the single-shot measurement, leads to the Heisenberg limit on measurement precision. Such a fundametal limit is also valid for the optical Mach-Zehnder interferometry, where the N00N state [46] $|\Psi\rangle = (|N_p,0\rangle + e^{iN_p\varphi}|0,N_p\rangle)/\sqrt{2}$ is usually employed. The state $|N_{p1},N_{p2}\rangle$ denotes the photon numbers in two arms are N_{p1} and N_{p2}, respectively.

Heisenberg limit, $\Delta\phi_L = 1/N_p$, imposed by the Heisenberg uncertainty principle (see Box 2).

Measuring the photon number N_p: Devices which are capable of precisely counting the number of photons at the single-quantum level are of particular importance to QIP. In particular, for applications in linear optics quantum computation [48, 49], the roles of single photonic qubits encompass information storage, communication and computation. They are also essential in quantum-sensing schemes in which the readout stage requires the detection

of small numbers of photons with high time resolution. Several factors are generally used to assess a photodetector: (i) Quantum efficiency (QE), i.e. the ratio of the number of photoelectrons collected by the detector to the number of incident photons; (ii) Dead time (recovery time), i.e. the time interval during which the detector is unable to absorb a second photon after the previous photon-detection event; (iii) Dark count rate, associated with the false detection events caused by the dark current in the detector; (iv) Timing jitter, i.e. the deviation of the time interval between the photon absorption and the electrical-pulse generation of the detector; and (v) Photon number resolution, i.e. the capability of distinguishing the photon number [50].

There are a large number of single photon detection technologies available, but perhaps the most conventional are photomultiplier tubes (PMTs) and single photon avalanche diodes (SPADs or APDs). In a PMT, a photon incident on the photocathode scatters a single electron and this electron is effectively multiplied at the successive dynode stages, giving rise to a macroscopic current in the external circuit. Despite comparatively low detection efficiencies (10–40% typical in the visible region [51]), the timing jitter can be extremely low, e.g. <10 ps in the study by Bortfeldt et al. [52], and PMTs are still widely used in a range of applications [53, 54]. SPADs are based on semiconductor pn junctions reverse biased above the breakdown voltage. Absorption of a photon creating an electron–hole pair leads to an avalanche current which is read out as a digital pulse [55]. Particular advantages include detection in the infra-red region using materials such as InGaAs/InP [56], low timing jitter (30 ps demonstrated in the study by Sanzaro et al. [57]), and room temperature operation [55]. Another semiconductor detector technology is the visible-light photon counter (VLPC), which unlike typical SPADs is capable of resolving the number of detected photons [58]. Choosing between different detector technologies inevitably involves trade-offs between the parameters described above, this is illustrated by the comparison of detector technologies available in 2011 given in the study by Eisaman et al. [51]. Superconducting nanowires (SNs) are a competitive alternative to avalanche diode detectors and offer superior detection efficiency and low dark count rate by comparison [59–61]. SNs are usually arranged in parallel, with each nanowire connected in series to a resistor. Each branch acts as a superconducting single photon detector [62]. When the nanowire is biased close to its critical current, the absorption of a photon triggers a second-order phase transition to a non-superconducting state, and the bias current is pushed to the external circuit. Divochy et al. demonstrate that in a parallel configuration, the resulting output voltage pulse is proportional to the number of photons [63]. In another experiment, Zen et al. used superconducting magnesium diboride strips to detect 20 keV biomolecular ions at a base temperature of 13 K [64]. SNs require temperatures on the order of a few kelvin to preserve the superconducting state and this makes it challenging to incorporate with other components for lab-on-chip-style biosensing schemes.

2.3 Cavity QED

One of the most fundamental scenarios in quantum optics is the so-called cavity quantum electrodynamics (cavity QED), which studies the properties of quantum emitters interacting with light confined in a high-Q cavity. Inevitable decay sources, spontaneous emission of emitter γ and cavity loss κ, interrupt the coherent emitter-photon interaction, erasing the quantum properties of the system after $t > \min(\gamma^{-1}, \kappa^{-1})$. The size of the quantum system, which is measured by the numbers of emitters and photons joining the interface, must be large enough that the system can exhibit/maintain quantum behaviour before the decay sources take effect [65, 66]. In practice, a quantum emitter in its excited $|e\rangle$ state may return back to the ground $|g\rangle$ state via spontaneously emitting a photon with a wave vector $\mathbf{k}$ and polarization μ. Indeed, this spontaneous emission is caused by the perturbation from the zero-point energy of the electromagnetic field $\mathbf{E}_{sp}^{(-)} = \sum_{\mathbf{k},\mu} \mathbf{e}^{*}_{\mathbf{k},\mu} \sqrt{\hbar\omega_k/2\epsilon_0 V_{eff}}\, a^{\dagger}_{\mathbf{k},\mu} e^{-i\mathbf{k}\cdot\mathbf{r}_0}$ with the emitter's location $\mathbf{r}_0$ and the frequency $\omega_k = c|\mathbf{k}|$. According to the Fermi's golden rule, the relevant transition rate is given by

$$\gamma = \frac{2\pi}{\hbar^2} \sum_{\mathbf{k},\mu} \frac{\hbar\omega_k}{2\epsilon_0 V_{\text{eff}}} \left| \langle g, 1_{\mathbf{k},\mu} | \left(\mathbf{d}\cdot\mathbf{e}_{\mathbf{k},\mu} \right)^{*} a^{\dagger}_{\mathbf{k},\mu} e^{-i\mathbf{k}\cdot\mathbf{r}_0} | e, 0\rangle \right|^2 \times \delta\left(ck - \omega_{eg} \right),$$

in the electric dipole approximation. In free space, the above equation is further rewritten as

$$\gamma = \frac{2\pi}{\hbar^2} \langle \mathbf{d}\cdot\mathbf{E}_{sp}^{(-)} \rangle^2 \rho_{vac}\left(\omega_{eg}\right),$$

by replacing the summation $\sum_{\mathbf{k}}(\cdot)$ with an integral $\frac{V_{\text{eff}}}{(2\pi)^3} \int_0^{\infty} k^2 dk \int_0^{\pi} \sin\theta\, d\theta \int_0^{2\pi} d\varphi$. Here, $\langle \mathbf{d}\cdot\mathbf{E}_{sp}^{(-)} \rangle^2 = \frac{\hbar\omega_{eg}}{6\epsilon_0 V_{\text{eff}}} |\mathbf{d}_{ge}|^2$ denotes the emitter-vacuum-field coupling intensity. The parameter $\rho_{\text{vac}}(\omega_{eg})$ with $\rho_{\text{vac}}(\omega) = \frac{\omega^2 V_{\text{eff}}}{\pi^2 c^3}$ is the density of electromagnetic modes per unit frequency around the transition frequency ω_{eg} of emitter within the quantization volume V_{eff}. The spontaneous emission rate of the emitter in free space finally reads as

$$\gamma = \frac{\omega_{eg}^3}{3\epsilon_0 \pi \hbar c^3} |\mathbf{d}_{ge}|^2,$$

which actually corresponds to the Einstein's A coefficient.

The spontaneous emission of an emitter depends strongly on the environment it resides in. The environment may be tailored by using a high-Q cavity. The resulting density of electromagnetic modes is in Lorentzian shape, $\rho_{\text{cav}}(\omega) = \frac{2}{\pi\kappa} \frac{\kappa^2/4}{(\omega-\omega_L)^2+\kappa^2/4}$ with the cavity loss rate κ and quality factor $Q = \omega_L/\kappa$. Thus, the spontaneous emission rate of an emitter located inside a cavity is expressed as $\gamma_{\text{cav}} = \gamma F_P \frac{\kappa^2/4}{(\omega_{eg}-\omega_L)^2+\kappa^2/4}$, where the so-called Purcell factor [67] is defined as

$$F_P = \frac{3Q}{4\pi^2} \left(\frac{V}{\lambda_{eg}^3} \right)^{-1}.$$

The factor 3 is originated from the fact that the dipole moment $\mathbf{d}$ is randomly oriented with respect to the laboratory frame. The combined emitter-cavity system can be parameterized by the emitter-photon coupling strength g (see Box 3), the saturation photon number $N_p^s = \gamma^2/(2g)^2$, and the critical excited emitter population $N_e^c = \kappa\gamma/(2g)^2$. The concepts of N_p^s and N_e^c may be understood from lasing dynamics [69], a process amplifying the coherent photons and maintaining the system's coherence.

In the weak-coupling regime, $g \ll \kappa, \gamma$, exploring the quantum properties of the emitter-cavity interaction requires a large system size because $N_p^s \gg 1$ and $N_e^c \gg 1$. In comparison, for $N_p^s \ll 1$ and $N_e^c \ll 1$, the required system size is significantly reduced down to a scale of one emitter and one photon, reaching the strong-coupling regime with $g \gg \kappa, \gamma$. The single emitter may repeatedly absorb and emit a single photon before the photon irreversibly escapes into the environment. This continuous exchange of excitation between emitters and cavity, known as Rabi oscillation, is imposed on the photons bouncing back and forth between cavity mirrors, resulting in a mode splitting in the spectrum (see Box 3). Thus, the vacuum Rabi splitting can be utilized as a diagnosis tool for the strongly coupled emitter-cavity system. A weak probe beam travels through the cavity with one emitter placed inside. The transmission spectrum of the probe beam exhibits two peaks due to the emitter-cavity interface and each peak is broadened with a spectral width $\sim\kappa, \gamma$. The inter-peak separation is determined by the resonant Rabi strength $2g$. Observing the splitting requires g exceeding both κ and γ. Enhancing the emitter-photon coupling strength g may be executed by two approaches (see Box 3): one is to choose a large transition dipole moment $|\mathbf{d}_{ge}|$ of the emitter, and the other is to suppress the cavity-mode volume V_{eff} while still maintaining a high quality factor $Q = \omega_L/\kappa$. Unfortunately, the former method is usually infeasible because the spontaneous emission rate γ is proportional to $|\mathbf{d}_{ge}|^2$ too, i.e. a larger $|\mathbf{d}_{ge}|$ leads to a larger γ. In contrast, the latter approach can be achieved through exquisite design of the fundamental properties of the cavity. We focus on the critical number of emitters N_e^c. Using the original expressions of γ and g (see Box 3), one finds that N_e^c is virtually equal to the reciprocal of the Purcell factor, which was originally introduced as an enhancement factor of the spontaneous emission of a dipole moment placed inside a resonator. Thus, it is natural to employ F_P to measure the emitter-photon coupling. Figure 3 summarizes the F_P factors of different emitter-cavity structures realized in recent experiments. The strong coupling between a single emitter and one photon leads to a value of F_P much greater than unity.

The Q factor for different types of cavities varies greatly, strongly dependent on their geometric structures and mechanisms of light confinement. The Q factor for microtoroid and microsphere cavities can be as high as 10^9 while that for plasmonic cavities is around 10 because of the huge ohmic loss of collective oscillations of surface electrons (Figure 3). Commonly, suppressing the volume V_{eff} is a general manner to enhance the emitter-cavity interaction.

When the size of emitter is much smaller than the cube of the photon wavelength λ_L^3 (more precisely V_{eff}), the emitter may be viewed as a point-like dipole located at $\mathbf{r}_o$, which couples to the local electric field of a cavity mode $\mathbf{E}(\mathbf{r}_o)$. The effective mode volume V_{eff} may be computed by averaging the whole energy of the cavity mode based on this local value, $V_{\text{eff}} = \int |\mathbf{E}(\mathbf{r})|^2 d\mathbf{r} / |\mathbf{E}(\mathbf{r}_o)|^2$. Since the cavity-mode energy is fixed (i.e. the energy of one photon $\hbar\omega_L$), placing the emitter at the maximum of $|\mathbf{E}(\mathbf{r})|$, $|\mathbf{E}(\mathbf{r}_o)| = \max(|\mathbf{E}(\mathbf{r})|)$ leads to the minimal volume and the maximal emitter-cavity coupling strength. In addition, designing the cavity structure to extremely enhance $|\mathbf{E}(\mathbf{r}_o)|$ makes the single-photon energy $\hbar\omega_L$ primarily focused on a small region around $\mathbf{r}_o$, strongly suppressing V_{eff}.

Plasmonic nanocavities are the most attractive candidate for achieving an extremely large g [74]. The features of surface plasmon resonance enable the electric field to be strongly confined above the surface with a depth much shorter than λ_L, resulting in a huge enhancement of local field. The effective cavity-mode volume may be smaller than $\lambda_L^3 \approx \lambda_{eg}^3$ [75–77]. This well exceeds other types of cavities since diffraction limits the confinement of light to smaller than λ_L^3. Nevertheless, reducing V_{eff} (enhancing g) is only a part of the story. The Q-factor of plasmonic cavities

Box 3

Quantum mechanical theory of the emitter-light interaction

The simplest physical system in quantum optics consists of a two-level (ground $|g\rangle$ and excited $|e\rangle$ states) emitter near-resonantly interacting with a single-mode quantized light field. The emitter-light interface is governed by the Jaynes-Cummings (JC) Hamiltonian in the rotating wave approximation (RWA) [68] $H/\hbar = \omega_L a^\dagger a + \frac{\omega_{eg}}{2}\sigma_z + g(\sigma_-^\dagger a + a^\dagger \sigma_-)$, where ω_{eg} is the emitter's transition frequency, ω_L is the light's frequency, $a^\dagger$ and a are the photon creation and annihilation operators with the bosonic commutators $[a, a^\dagger] = 1$ and $[a^\dagger, a^\dagger] = [a, a] = 0$, $\sigma_- = |g\rangle\langle e|$ and $\sigma_-^\dagger$ are the lowering and raising operators of the quantum emitter. The parameter $g = |d_{ge}|\sqrt{\omega_L/2\hbar\epsilon_0 V_{\text{eff}}}$ measures the emitter-photon coupling strength. Here, d_{ge} is the emitter's transition (from $|e\rangle$ to $|g\rangle$) dipole moment and V_{eff} represents the effective quantization volume of the light field.

The Hilbert space is spanned by the product-state basis $\{|u, n_p\rangle; u = e, g; n_p \in Z\}$. The Fock state $|n_p\rangle$ denotes that the number of photons within V_{eff} is n_p. The zero-photon state $|n_p = 0\rangle$ is referred to as the vacuum state. The photon operators a and $a^\dagger$ acting on the Fock states gives $a|n_p\rangle = \sqrt{n_p}|n_p - 1\rangle$ and $a^\dagger|n_p\rangle = \sqrt{n_p + 1}|n_p + 1\rangle$. The interaction term $\sigma_-^\dagger a$ ($a^\dagger\sigma_-$) in the Hamiltonian H describes the process that the emitter transits from $|g\rangle$ ($|e\rangle$) to $|e\rangle$ ($|g\rangle$) by absorbing (emitting) one photon. Under the basis $|u, n_p\rangle$, H may be expressed in a matrix form that is divided into a set of 2×2 block submatrices. Each sub-block is spanned by $|e, n_p\rangle$ and $|g, n_p + 1\rangle$, except for the ground $|g, 0\rangle$ state. Diagonalizing the sub-blocks leads to the eigenvalues $\omega_{n_p,\pm} = \omega_L(n_p + 1/2) \pm \Omega_{n_p}/2$, and the so-called dressed states, $\Psi_{n_p,+} = \cos\theta_{n_p} e, |n_p\rangle + \sin\theta_{n_p} g, |n_p + 1\rangle$ and $\Psi_{n_p,-} = \sin\theta_{n_p}|e, n_p\rangle - \cos\theta_{n_p}|g, n_p + 1\rangle$ with $\sin\theta_{n_p} = 2g\sqrt{n_p + 1}/\sqrt{2\Omega_{n_p}(\Omega_{n_p} - \Delta)}$ and $\cos\theta_{n_p} = (\Omega_{n_p} - \Delta)/\sqrt{2\Omega_{n_p}(\Omega_{n_p} - \Delta)}$. The generalized Rabi frequency Ω_{n_p} and detuning Δ are defined as $\Omega_{n_p} = \sqrt{\Delta^2 + 4g^2(n_p + 1)}$ and $\Delta = \omega_L - \omega_{eg}$. The energy spacing $\Delta\omega_{n_p} = \omega_{n_p,+} - \omega_{n_p,-}$ between two dressed states is minimized at $\Delta = 0$ with $\Delta\omega_{n_p} = 2g\sqrt{n_p + 1}$, corresponding to the avoided level crossing. In particular, the vacuum field resonantly coupling to the emitter gives the vacuum Rabi splitting $\Delta\omega_0 = 2g$, which is solely determined by the emitter-photon coupling strength g, and two lowest dressed states $|+\rangle = \Psi_{0,+} = (|e, 0\rangle + |g, 1\rangle)/\sqrt{2}$ and $|-\rangle = \Psi_{0,-} = (|e, 0\rangle - |g, 1\rangle)/\sqrt{2}$ (see Figure B2a).

The JC model can be also generalized to the quantum system of multiple emitters interacting with photons. For a quantum system consisting of n_e emitters and one photon, the emitter-photon coupling strength is derived as $2g\sqrt{n_e}$ (see Figure B2b). Thus, increasing the emitter number may enhance the vacuum Rabi splitting $\Delta\omega_0$ too.

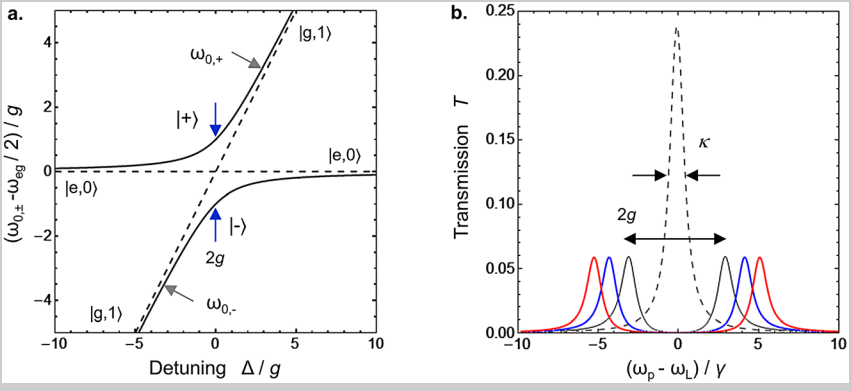

Figure B2: Cavity QED spectrum.
(a) Energy spectrum $\omega_{0,\pm}$ of the quantum system composed of one emitter and one photon as a function of the detuning $\Delta = \omega_L - \omega_{eg}$ between cavity ω_L and emitter-transition ω_{eg} frequencies. The presence of anti-crossing between two energy-level branches at $\Delta = 0$ proves the formation of polaritons, $|+\rangle = (|e, 0\rangle + |g, 1\rangle)/\sqrt{2}$ and $|-\rangle = (|e, 0\rangle - |g, 1\rangle)/\sqrt{2}$. The eigenstates at selected locations have been marked. (b) Transmission spectrum vs. the probe-beam frequency ω_p, corresponding to the atom-FP-cavity platform shown in (a). Adapted from [29].

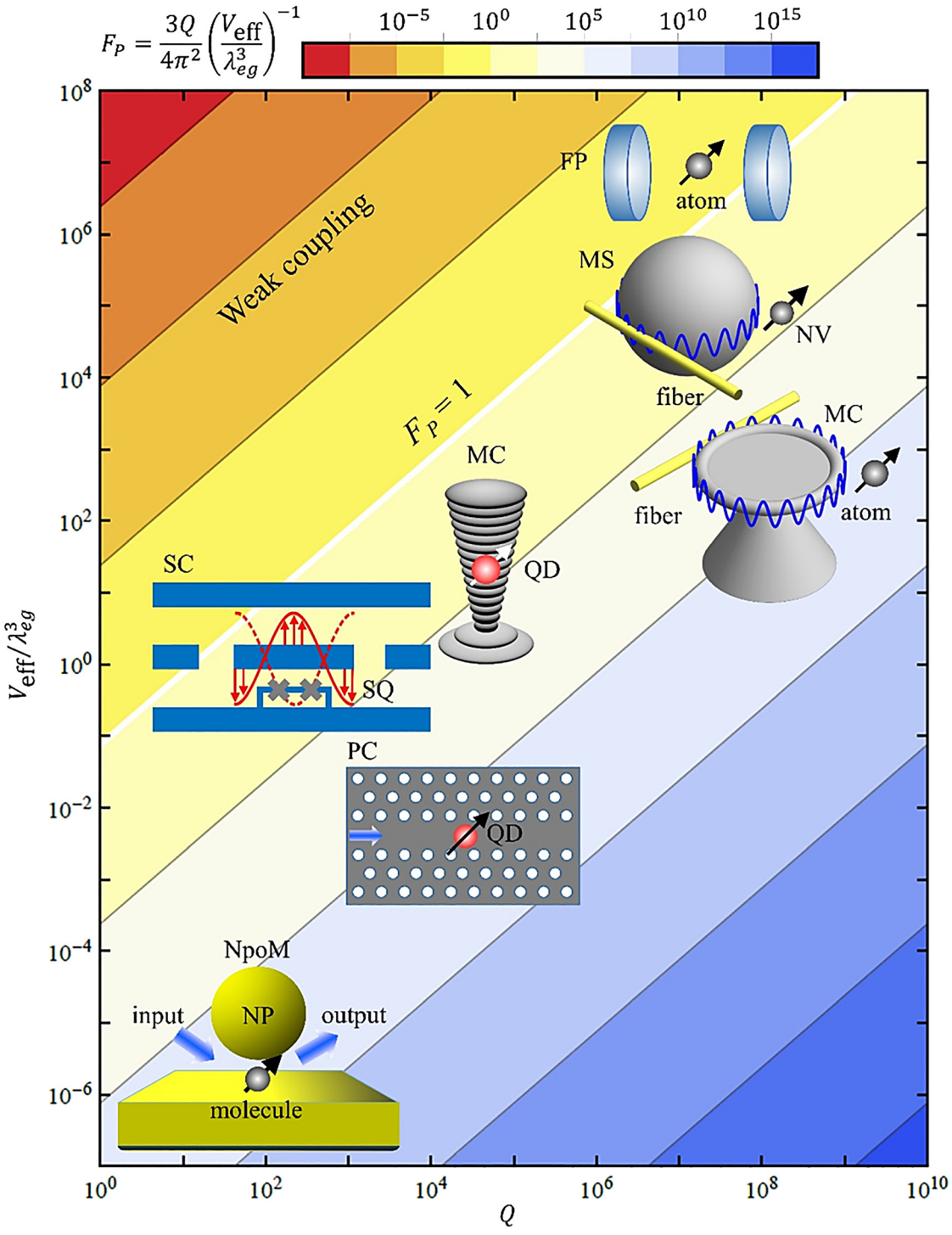

Figure 3: Purcell factors F_P for different QED structures.
The quantum emitters may be atoms, molecules, QD (quantum dot), NV (nitrogen-vacancy) centre and SQ (superconducting qubit). The resonators include FP (Fabry-Pérot), MT (microtoroid), MS (microsphere), MP (micropillar), PC (photonic crystal), NpoM (nanoparticle-on-mirror) and SC (superconducting) cavities. The arrow crossing sphere represents the transition dipole moment of the quantum emitter. All these QED systems achieved in experiment are in the strong-coupling regime $F_P > 1$.

is only about 10, much lower than other cavity structures. The Purcell factor F_P achieved in recent experiments based on the nanoparticle-on-mirror-plasmonic-cavity structure reaches over 10^3 [77–81]. The enhanced single-photon Rabi frequency g (10^{13}~10^{14} s^{-1}) and spontaneous emission rate of emitters prohibits the direct measurement of Rabi flopping due to the limited instrumental response. The vacuum Rabi splitting was first measured in an atom-FP-cavity structure [82], with a ^{133}Cs atomic beam flying through a high-Q optical Fabry-Pérot interferometer.

So far, such a vacuum Rabi splitting has also been performed principally in other diverse emitter-cavity systems, including single atoms interacting with microtoroid cavities [83], the interface between nitrogen-vacancy centres and whispering-gallery waves of a microsphere [84], quantum dots fabricated in a micropillar [85] and photonic crystal cavities [86], superconducting qubits coupled with superconducting resonators, and hybridization of molecules in microcavities [87–89]. Besides exploiting the fundamental properties of light–matter interface, the strong emitter-cavity coupling is of particular importance to QIP [90–92] because the relevant quantum operations, e.g. reading, transferring, writing and storing the information between quantum memory (long-lived emitters) and flying qubits (photons), can be accomplished with a high fidelity. It also possesses the potential of wide application in quantum sensing, such as detecting the weak electric/magnetic fields [93, 94] and exploring gravity [95]. Moreover, the recent implementation of the strong interaction between molecules and plasmonic nanoresonators [80, 96] may pave the avenue towards exploring new types of quantum chemistry and molecular reaction [74, 97].

3 Quantum non-classical photon probes: entangled photons and squeezed states

Quantum photonic science and technology is envisaged to bring about unprecedented ultra-sensitive detection schemes to overcome the standard quantum limit (SQL) by means of quantum correlated light sources and metrology. The SQL quantifies the best precision achievable in a measurement without the use of quantum correlations of photon flux, in particular for optical phase measurements where it corresponds to shot noise (see Box 2). In the meantime, there are also scientific and technological challenges to overcome for non-classical states of light to be compatible with the present day integrated nanophotonic/nanoplasmonic sensing platforms. In 1981, Caves proposed quantum noise reduction highlighting its importance in optical interferometry [98]. In the recent past, non-classical sources are getting more attention as promising sources for quantum noise reduction. Two of the very important quantum states of non-classical light that are highly preferred in quantum photon sensing are "squeezed states" and "entangled states".

Perhaps the most well-known example of using non-classical light to enhance the sensitivity of a measurement is the use of squeezed light in gravitational wave interferometry, for example at LIGO [22]. Squeezed light is a broad category of non-classical light states for which fluctuations in the field quadratures are supressed below the fluctuations in the unmodified vacuum state. These states are typically generated using non-linear light–matter interactions; the first demonstrations used four-wave mixing [99, 100] and parametric down conversion [101]. Squeezing can now exceed a 10 dB reduction in field quadrature fluctuations [102–105], reaching as much as 15 dB [106], and compact, ultra-low pumping power squeezed light sources have also been developed, e.g. the study by Otterpohl et al. [107]. Here, a brief overview of the theoretical description of squeezed states is given, for a thorough review see Loudon and Knight [108].

For a single electromagnetic mode described by a quantum harmonic oscillator in the photon number state representation, the creation and annihilation operators are $\hat{a}^\dagger$ and $\hat{a}$, respectively. The field quadrature operators are then defined as:

$$\hat{X}_1 = (\hat{a}^\dagger + \hat{a})/2\,; \quad \hat{X}_2 = i(\hat{a}^\dagger - \hat{a})/2.$$

Note that some texts use the notation $\hat{X}, \hat{Y}$ instead of $\hat{X}_1, \hat{X}_2$ [109].

Making an analogy with a one-dimensional quantum harmonic oscillator particle with mass m and angular frequency ω, the field quadratures can be related to the displacement and momentum operators [109]:

$$\hat{x} = (\hbar/2m\omega)^{1/2}(\hat{a}^\dagger + \hat{a}) = (2\hbar/m\omega)^{1/2}\hat{X}_1;$$
$$\hat{p}_x = i(m\hbar\omega/2)^{1/2}(\hat{a}^\dagger - \hat{a}) = (2m\hbar\omega)^{1/2}\hat{X}_2.$$

This is why the dimensionless field quadrature operators can be referred to as the "position" and "momentum" quadratures. In the number representation, a state of light may be represented by a phasor in quadrature operator space, with length $|\alpha|$ corresponding to the square root of the average photon number and the argument ϕ corresponding to photon phase (Figure 4).

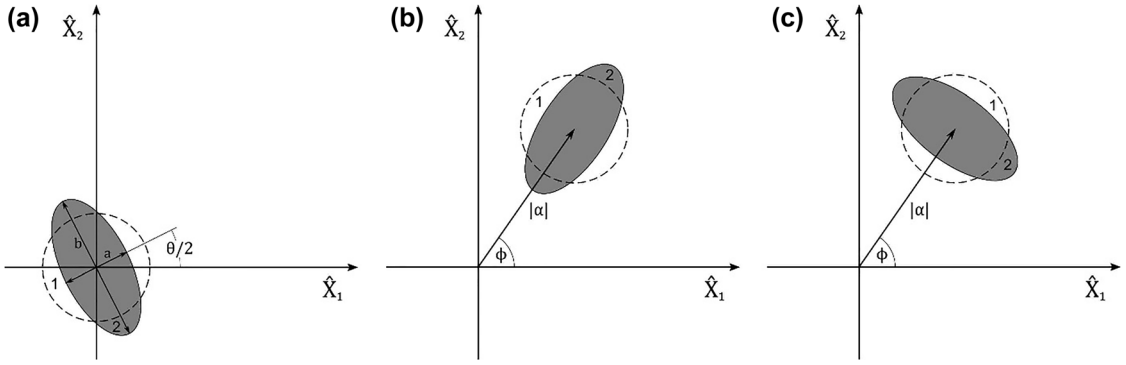

Figure 4: Quadrature-space representation of squeezed states.
The quadrature circles and ellipses indicate the uncertainties in the field quadratures ΔX_1, ΔX_2. Vacuum and coherent states (1) have equal quadrature uncertainties. When these states are transformed to squeezed states the area of the uncertainty ellipse (2) is conserved [108]. (a) Vacuum state (1) and squeezed vacuum state (2). (b) Bright phase-squeezed state (2) generated from a coherent state (1) with amplitude $|\alpha|$ and phase ϕ. (c). Bright amplitude-squeezed state.

The position and momentum operator uncertainties obey the Heisenberg Uncertainty Principle: $\Delta x\, \Delta p_x \geq \hbar/2$. Via the relations above for $\hat{x}, \hat{p}_x$, it follows that the quadrature operator uncertainties must obey the inequality [109]:

$$\Delta X_1\, \Delta X_2 \geq 1/4.$$

The equality in this relation is realized for minimum uncertainty states, in which case $\Delta X_1 = \Delta X_2 = 1/2$. Examples of these are coherent and vacuum states, and the minimum quadrature uncertainties can be understood to originate from vacuum fluctuations in a given mode of the electromagnetic field.

Quadrature-squeezed states have $\Delta X_1 \neq \Delta X_2$, so that the uncertainty in one quadrature may be decreased below the vacuum fluctuation level at the expense of the other quadrature, while still satisfying the uncertainty relation. Figure 4 illustrates several examples of squeezed states, represented by uncertainty ellipses in quadrature space. Squeezed vacuum states are centred on the origin since $|\alpha| = \sqrt{\bar{n}} = 0$ and bright squeezed states have $|\alpha| > 0$. Special cases of the bright squeezed states are amplitude-squeezed and phase-squeezed states, although arbitrary orientations of the squeezed uncertainty ellipse are possible [109]. Squeezed states are typically characterized by interference with a local oscillator field in a homodyne detection scheme [108].

Modern sources of squeezed light typically use optical parametric oscillators or amplifiers (OPOs and OPAs); by placing the non-linear medium in an optical cavity the strength of the non-linear interaction is enhanced and the spectral properties of the generated squeezed state can be tuned. These OPO/A cavities can take the form of external Fabry–Pérot or ring cavities, or fully monolithic or semi-monolithic designs using reflective coatings applied directly to the non-linear crystal end surfaces [110–112]. Depending on the input modes to the cavity, two broad classes of squeezed states are generated: squeezed vacuum and bright squeezed states, these are illustrated in Figure 4. In an OPO the only input is the pump field, the input to the squeezed mode is a vacuum state and hence a squeezed vacuum mode is generated. If a coherent input seed field is introduced in an OPA, the squeeze operator is acting on a coherent state and a bright squeezed mode is generated [113]. The phase difference between the pump and seed input fields determines the argument of the complex squeeze parameter θ and the angle in quadrature space along which the output state will be squeezed.

As well as squeezed light, photon correlations and entangled states are widely used as optical probes in quantum metrology. Entangled states are many-body states which cannot be described by a single separable (product) state $|\Psi_N\rangle$:

$$|\Psi_N\rangle = |\psi_1\rangle|\psi_2\rangle \ldots |\psi_N\rangle.$$

In the case of photons, entanglement may be produced in the momentum, energy and polarization degrees of freedom [114]. Two-photon states constructed with correlations in all these degrees of freedom are referred to as hyper-entangled [115]. A common entangled state discussed for quantum metrology is the N00N state [116], constructed by entangling N photon states in the two optical paths A, B, often in a Mach–Zenhder interferometer:

$$|\Psi_{\mathrm{N00N}}\rangle = \left(|N\rangle_A\, |0\rangle_B + |0\rangle_A |N\rangle_B \right) \Big/ \sqrt{2}.$$

This state is useful in quantum sensing schemes since it maximizes the photon number uncertainty in each

interferometer path for a given number of input photons. For phase measurements using interferometry, this minimizes the phase uncertainty due to the photon number-phase uncertainty relation [1]. Entangled photon pairs are often referred to as EPR states, after the states discussed by Einstein, Podolsky and Rosen when considering the nature of locality in quantum mechanics [117]. These states are commonly produced by spontaneous parametric down conversion (SPDC) in non-linear optical media [118]. In quantum metrology and also quantum communications entangled photon pairs are of particular interest for generating heralded single photons [119]. Pairs of photons are separated in a given degree of freedom (e.g. separated into orthogonal momenta or polarizations); detecting one of each pair then "heralds" the arrival of the other, allowing post-selection of single photon detections.

4 Quantum optical measurement schemes

Sensing experiments exploiting quantum optics generally concern counting single photon detections and measuring correlations between detections on different optical paths. Here, we summarize a few basic measurements which form the building blocks of many quantum optical metrology experiments.

The Hanbury Brown and Twiss (HBT) experiment is used extensively in experimental quantum optics to measure the second-order (intensity) correlation function, $g^{(2)}(\tau)$, of an optical beam [120]. For a beam split into two modes (1,2), the $g^{(2)}(\tau)$ function is defined [109]:

$$g^{(2)}(\tau) = \frac{\langle n_1(t+\tau)n_2(t)\rangle}{\langle n_1(t+\tau)\rangle\,\langle n_2(t)\rangle} = \frac{\langle \hat{a}_1^\dagger(t+\tau)\hat{a}_2^\dagger(t)\hat{a}_2(t)\hat{a}_1(t+\tau)\rangle}{\langle \hat{a}_1^\dagger(t+\tau)\hat{a}_1(t+\tau)\rangle\,\langle \hat{a}_2^\dagger(t)\hat{a}_2(t)\rangle}$$

where $n_{1,2}$ are the photon numbers detected in each mode, $\hat{a}_{1,2}^\dagger(\hat{a}_{1,2})$ are the creation (annihilation) operators, and $\langle \dots \rangle$ denotes averaging over many measurements (or over time t).

In practice, the beam is passed through a beamsplitter to single photon detectors at each of the output ports and detections are recorded using a time-to-digital converter. A normalized histogram of the time delay τ between detections at the two detectors corresponds to the $g^{(2)}(\tau)$ function. The value of this function at zero time delay is an important parameter when characterizing a quantum optical light source, for example light generated from quantum emitters or a non-linear optical medium. A value $g^{(2)}(0) < 1$ indicates a non-classical anti-bunched state, while $g^{(2)}(0) < 0.5$ is generally accepted as an indication of a single photon state [124]. An ideal one photon Fock state would have $g^{(2)}(0) = 0$. HBT can be performed either on a continuous wave (CW) or pulsed beam, resulting in different forms for the $g^{(2)}(\tau)$ function, each is illustrated in Figure 5b and c. CW anti-bunched light produces an anti-bunching dip at $\tau = 0$ with a width proportional to the photon coherence time, while pulsed anti-bunched light will produce peaks at multiples of the pulse repetition period, with the peak at $\tau = 0$ being suppressed.

Hong-Ou-Mandel (HOM) interference is a phenomenon observed when a pair of indistinguishable photons arrives at the two input ports of a beamsplitter [125]. For truly indistinguishable photons arriving simultaneously, the only possible output states are both photons leaving through the same output port; no coincidences between detections at the outputs will be observed. Therefore, a histogram of coincidences as a function of delay time between detections at the outputs will fall to zero at zero time delay for the interference of indistinguishable photons: a "HOM dip" as shown in Figure 5e. The HOM signal depends on the relative phase, frequency detuning and polarization of the incident photons [126, 127], as well as the time and frequency jitter in the system generating the photons [128]. For pairs of photons slightly detuned in frequency, it is possible to observe oscillations in this HOM signal, referred to as "quantum beating" [129, 130].

The visibility of HOM interference can be defined as $V_{\mathrm{HOM}} = 1 - (\int C_{\parallel}(\tau)d\tau / \int C_{\perp}(\tau)d\tau)$, where $C_{\parallel,\perp}(\tau)$ is the coincidence detection rate for parallel (interfering) and perpendicular (non-interfering) polarized photons arriving at the beamsplitter with a time delay τ [131]. The visibility parameter acts as a measure of indistinguishability between two beams. The indistinguishability of successive single photon pulses can also be measured by separating every other pulse with an electro-optic switch into a delay line, then interfering pairs of pulses on a beamsplitter. Measurement of the HOM visibility has been proposed as a quantum sensing method, which has been predicted to show high sensitivity in measuring refractive index changes [132].

The detection rate of coincidences between more than two detectors may also be used. For entangled pairs of photons between two optical paths, detecting a photon in one path indicates the arrival of its pair in the other path. This is the principle behind heralded detection of single photons, but may also be applied in more complex

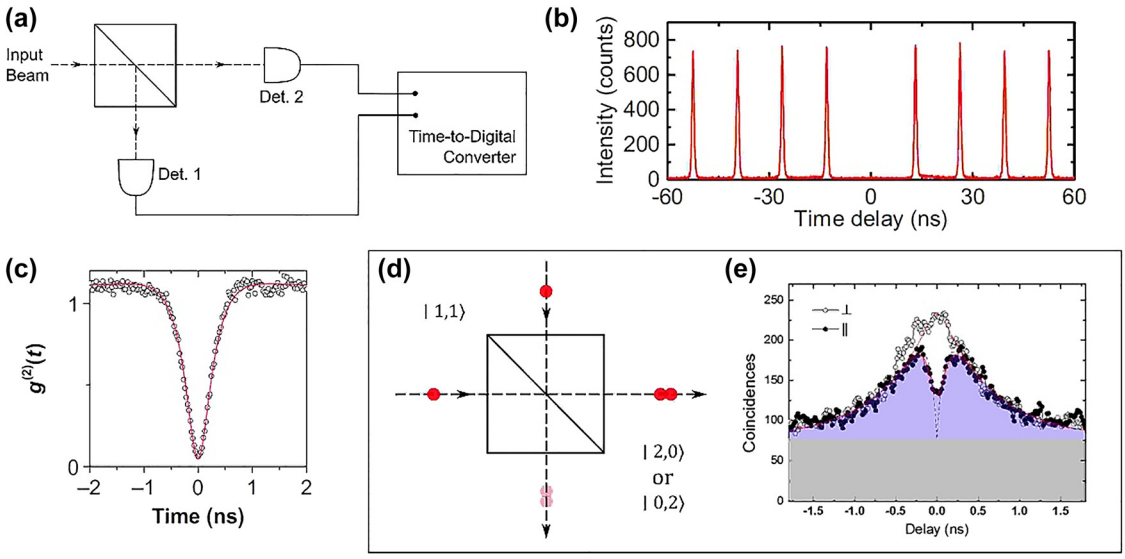

Figure 5: Hanbury Brown and Twiss (HBT) measurement of the second-order correlation function and Hong-Ou-Mandel (HOM) interference. (a) Schematic of a basic HBT setup. The time-to-digital converter records photon detection times and the normalized histogram of time differences t between detectors 1 and 2 is the $g^{(2)}(t)$ function for the input beam. (b) $g^{(2)}(t)$ function (unnormalized) for emission from quantum dots pumped by a pulsed laser, rather than showing an anti-bunching dip, the peak at $t = 0$ is missing. Adapted from the study by Bennett et al. [121] under Creative Commons Attribution 4.0 International License. (c) Normalized $g^{(2)}(t)$ function for anti-bunched emission from a quantum dot pumped by a continuous wave laser. Adapted from the study by Hanschke et al. [122] under Creative Commons Attribution 4.0 International License. (d) Schematic of the HOM effect: a pair of indistinguishable photons arriving simultaneously at a beamsplitter can only produce photon pairs at the outputs. Therefore, no coincidences would be measured by detectors at each of the output ports for completely indistinguishable input photons. (e) HOM interference dip. Coincidence detections when pairs of single photon pulses from a photonic crystal quantum dot are interfered on a beamsplitter, with parallel ∥ or perpendicular ⊥ polarizations. Parallel-polarized photons are indistinguishable and so coincidences at zero time delay are suppressed by the HOM effect. Adapted from the study by Kim et al. [123].

schemes involving one detector heralding photon arrivals at several other detectors. For example, the experiment shown in the study by Crespi et al. [133] uses four detectors (A–D) to detect different output states: coincidences at A, C and B, D count states $|2, 0\rangle$, $|0, 2\rangle$ while coincidences between A and B count the state $|1, 1\rangle$.

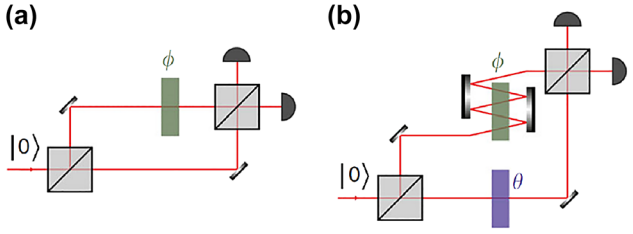

Figure 6: Mach-Zehnder interferometer (MZI).
(a) Conventional MZI setup with input state $|0\rangle$ and phase difference ϕ between the two arms. The intensity at each detector oscillates as a function of ϕ allowing the phase to be measured. (b) An adaptive interferometer is implemented by adding a variable phase element θ which is controlled to operate the interferometer at the maximum sensitivity. Adapted from the study by Daryanoosh et al. [134] under Creative Commons Attribution 4.0 International License.

A common measurement scheme in quantum optical metrology is the Mach-Zehnder interferometer (MZI), consisting of two beamsplitters in succession (Figure 6). A phase difference between the two optical paths modulates the count rates at the output detectors, allowing a phase change to be transduced into an intensity change. In a biosensing application, the phase change might be introduced by a change in refractive index of the sensor environment due to the concentration of a biomolecule of interest, for example. MZIs with entangled input states have allowed optical phase measurements at a precision beating the standard quantum limit (SQL) [34, 135]. In particular, N00N states increase the frequency of intensity oscillations with changing phase difference by a factor of N [136]. Adaptive interferometry applies an additional variable phase difference between the optical paths in order to make measurements at points in the intensity oscillations with maximum slope, and hence maximum sensitivity [137].

5 Quantum detection limits in biosensing and metrology

Owing to its short wavelength and high coherence, the light wave has been widely applied in precision measurement and sensing. One of the typical optical sensors is the Michelson-Morley interferometer (MMI), which makes use of multiple-beam interference to detect the tiny displacement (a few wavelengths) of an object. Here two inter coherent light beams travel along different arms and then are forced to interfere with each other. Any disturbance in either optical path can be distinctly reflected in the interference pattern that records the accumulated inter-optical-path phase difference. Perhaps its most well-known finding is the direct observation of cosmic gravitational waves. As predicted by Einstein's general relativity theory, the gravitational waves can cause space to stretch and compress in two orthogonal directions. The Laser Interferometer Gravitational-Wave Observatory (LIGO), a gigantic MMI, was built for detecting such a space distortion. Each arm of LIGO is 4-km long and this length is further extended up to 1600 km by applying a Fabry–Pérot resonator in each arm. In 2015, LIGO firstly recorded a transient GW signal with a peak GW strain of one part in 10^{21} [138].

One obtains the MZI (Figure 6) by introducing a second beam splitter into MMI. This extra beam splitter actually acts as a beam combiner, and no beams are redirected into the light source, avoiding disturbance. In comparison to MMI, MZI is commonly applied as a transducer for biosensing, where one arm works as a *reference* while the other is the *sensing* area. A small change of the refractive index caused by, e.g. the binding reaction of biomolecules and the variation in biomass or number of biomolecules, in the sensing arm is converted into a resonant wavelength shift [139]. Such a detection is highly sensitive, fast and reproducible. Different optical techniques, such as phase modulation [140] and multimode propagation [141] may be performed on MZI so as to improve the detection. MZI-based biosensors can be constructed using nano-optical waveguides [142], making use of the evanescent field detection principle, and are able to be integrated with a microfluidic polymer network to form a cost-effective lab-on-a-chip platform [143]. Such a miniaturized device offers real-time label-free detection [144]. In addition, replacing the light waves with surface plasmon waves propagating on the top and bottom surfaces of a metal film, i.e. a plasmonic MZI, further enhances the refractive index sensitivity [145].

The heart of various optical biosensors is the high-coherence light source (i.e. laser), which is generally locked to an optical resonator. Sensing applications require that the laser possess a stable central frequency, enabling a long-term detection without calibrating. In addition, the sensor's sensitivity, usually represented by the frequency shift or the spectral broadening [146], is mainly limited by the laser linewidth. Reaching the ultimate single molecule detection sensitivity relies on an ultranarrow linewidth. Currently, one of the most sensitive single-molecule interferometry techniques with optical resonators employs commercially available narrow linewidth external cavity lasers as the wavelength-tuneable laser sources combined with high Q glass microsphere (whispering-gallery mode) resonators [147].

In established areas of precision measurements such as in optical physics, state-of-the-art laser systems for sensing with ultra-stable frequency and ultra-narrow linewidth have been obtained based on the techniques developed in optical clocks. A typical clock configuration is composed of a local oscillator (i.e. laser source) with its frequency being interrogated and locked to a high-Q frequency reference (i.e. atomic/ion transition) via a servo loop. To date, the best record of the laser linewidth has reached the sub-10 mHz level, corresponding to a phase coherence up to 55 s [39]. The best accuracy of optical clocks has been achieved to be 9.4×10^{-19} [43]. That is, the clock will not gain or lose a second in 33 billion years, longer than the age of the universe (13.8 billion years). In addition, the record for the best stability held by optical clocks is $\sigma_y(\tau) = 4.8 \times 10^{-17}/\sqrt{\tau}$ with the measurement time τ of each tick [148]. Recently, the size of optical clocks has been shrunk significantly, achieving on-chip timekeepers [149, 150]. Using the advances made for optical clocks and their precision light sources has prospects in advancing the ultimate detection limits for single-molecule detection on microfluidic laboratories on chip.

For example, precision optical measurements in quantum metrology are now capable of approaching the Heisenberg limit (see also Box 2); the ultimate limit to phase uncertainty for a given optical power. In biosensing, there is also much interest in beating the standard quantum limit to achieve quantum-enhanced optical measurements, particularly due to the constraints on optical power placed by the photo-damage threshold of a biological sample. In the following we outline some biosensing experiments which have used quantum optical probes such as entangled photon pairs, heralded single photons and squeezed light to surpass classical detection limits.

Crespi et al. measured protein concentrations in an interferometer using entangled photon $N = 2$ N00N states as probes [133]. A blood protein was introduced to one interferometer arm via integrated microfluidics, providing

a phase shift dependent on the refractive index and hence the concentration, in a Mach-Zehnder Interferometer setup. Accounting only for post-selected photons, the uncertainties in these measurements were below the quantum noise limit.

Squeezed light experiments have since pushed biosensing precision limits further. Particle tracking experiments using a squeezed local oscillator field allowed Taylor et al. to track nanoparticles and lipid granules at resolutions up to 42% below the quantum noise limit, within living yeast cells [151, 152]. Although the sensitivity achieved here is possible using a purely classical probe, using squeezed light allowed low light intensities to be used, hence reducing the risk of photodamage in biological samples. In particular, this could allow the observation of dynamics in biological systems over longer time periods than previously possible.

An alternative approach to measure concentrations by refractive index sensing is the use of plasmonic sensors based on metal films. Pooser et al. illuminated a plasmonic sensor with squeezed light produced by four-wave mixing and observed a 4.6 dB reduction in the noise floor power below the shot-noise limit [154]. They estimate a 50% improvement in the smallest resolvable refractive index shift over an equivalent measurement using classical illumination. More recently, the sensitivity of this setup was improved by nearly five orders of magnitude, this time using a plasmonic film with an array of triangular nanoholes to detect ultrasound-induced refractive index changes in air [156]. Plasmonic sensing has also been performed using heralded single photons to provide a sensitivity enhancement over a comparable coherent probe state [162]. In this experiment, a bovine serum albumin (BSA) sample concentration was measured using the transmitted heralded single photon count rate. First the transmission spectrum was measured as a function of angle of incidence at different concentrations, then changes in the transmission with changing concentration; both methods demonstrated an advantage in sensitivity over the sensitivity possible using classical measurements at the same light intensity.

Moving from biosensing experiments to general quantum metrology, the most precise optical phase measurements made to date have achieved Heisenberg scaling phase uncertainty and some have approached the absolute Heisenberg limit. Daryanoosh et al. reported a phase measurement with precision within 4% of the absolute Heisenberg limit using an entangled probe state which passes the phase element three times per measurement shot [134]. Multipass interferometry combined with adaptive measurement algorithms—in which a control phase is updated between measurements as more information on the unknown phase is obtained—allow Heisenberg scaling even without an entangled probe state [137].

It is important to be clear about the intensity passing through a sample which is taken into account when claiming sub-shot noise or Heisenberg scaling uncertainties. The previous two experiments required post-selection of photons in order to achieve Heisenberg scaling uncertainties. When taking all optical power into account however, the shot-noise limit can still be surpassed; Slussarenko et al. have made “unconditional” sub-shot-noise

Table 1: Comparison of quantum-enhanced sensing experiments with potential applications in biosensing.

Year	Ref.	Description	Optical probe	QNL beaten?	Biosensing?
2012	[133]	Protein concentration measurement using microfluidic-integrated interferometer	Entangled $N = 2$ N00N states	✓	✓
2013	[151]	Particle tracking in living cells	Squeezed local oscillator	✓	✓
2014	[152]	Particle tracking with sub-diffraction limit spatial resolution	Squeezed local oscillator	✓	✓
2015	[153]	Microcantilever displacement measurement	Squeezed light	✓	✗
2016	[154]	Plasmonic refractive index sensing	Twin beam squeezed light	✓	✗
2017	[155]	Single molecule detection at the quantum noise limit	Coherent	✗	✓
2018	[156]	Plasmonic refractive index sensing	Twin beam squeezed light	✓	✗
2018	[157]	Optomechanical magnetometer	Squeezed light	✓	✗
2018	[158]	Plasmonic refractive index sensing	Heralded single photons	✓	✓
2020	[159]	Stimulated Raman spectroscopy	Bright squeezed light	✓	✗
2020	[160]	Stimulated emission microscopy	Intensity squeezed light	✓	✗
2020	[161]	Coherent Raman microscopy	Bright squeezed light	✓	✓

Experiments in which the measurement precision exceeded the quantum noise limit (QNL) are indicated; those which explicitly make measurements on biological samples are indicated in the biosensing column. The state-of-the-art in single molecule detection is quantum noise limited (i.e. at the QNL), and is shown for comparison.

limit phase measurements using $N = 2$ N00N states in an interferometer [34]. In order to achieve this, very high optical efficiency was required; the power transmission in each interferometer path was ~0.8, including all loss channels and the detection efficiencies of the superconducting nanowire detectors.

Table 1 collects some quantum enhanced sensing experiments which relate closely to biosensing, i.e. magnetometry, particle tracking and refractive index sensing. Some of these techniques explicitly make measurements on biological systems, such as protein molecules and even living cells. Although biosensing experiments are as yet far from reaching Heisenberg scaling uncertainties and exploiting the full potential of quantum-enhanced measurements, techniques from state-of-the-art quantum metrology experiments will direct future developments in biosensors. The practical considerations and potential barriers to applying quantum metrology methods to biosensing and imaging are discussed further in the study by Taylor and Bowen [1].

6 Quantum optical measurement building blocks: materials, devices and integrated technologies

Integrated quantum sensing devices—quantum sensors on-chip—are promising for producing robust devices; mitigating the effects of optical losses and the need for delicate alignment. Future sensors exploiting quantum optics will require on-chip sources of non-classical photon states. Operation at room temperature is also important in an integrated device incorporating a biological sample: since the sample is necessarily close to the chip cryogenic conditions cannot be used for a truly integrated device. Promising candidates for single quantum emitters include NV centres, defects in hexagonal boron nitride (hBN) and quantum dots. Non-linear interactions in waveguides and micro-resonators are also discussed as bulk sources of single photons, entangled pairs and squeezed light.

6.1 Nitrogen vacancy centres as quantum emitters

As well as in spin-based sensing, nitrogen vacancy (NV) centres also have applications as single photon emitters [163]. NV centres feature a fluorescence peak around 437 nm; the Hamiltonian for the triplet ground and excited states of NV^- share the following form [164]:

$$\frac{\widehat{H}_{\mathrm{NV}}}{h} = (D + d_{\parallel}E_{\parallel})\widehat{S}_z^2 + \gamma_{\mathrm{B}}\boldsymbol{B}\cdot g\cdot\widehat{\boldsymbol{S}} + \widehat{\boldsymbol{S}}\cdot A\cdot\widehat{\boldsymbol{I}}$$

where D is the crystal-field splitting (Hz), γ_{B} is the gyromagnetic ratio (Hz/G), $d_{\parallel}$ is the axial electric-field dipole moment [Hz/(V/cm)], $E_{\parallel}$ is the axial electric field (V/cm), $\boldsymbol{B}$ is the magnetic-field vector, g is the g factor tensor, $\widehat{\boldsymbol{S}}$ is the vector of electronic spin-1 Pauli operators, A is the hyperfine tensor and $\widehat{\boldsymbol{I}}$ is the vector of nuclear spin-1 Pauli operators. Emission from an individual NV defect has been shown to produce anti-bunched photon states [165–167]. The purity of single photon emission in these first demonstrations was high, with second-order correlation functions of $g^{(2)}(0) = 0.26$ in bulk diamond [166] and $g^{(2)}(0) = 0.17$ in diamond nanocrystals [167]. These nanocrystals have been shown to be biocompatible and have potential sensing and imaging applications within living cells [168]; exploiting both their potential for magnetometry (see also Section 7.1) and sub-diffraction imaging (see also Section 7.5). NV centres have also been proposed as sources of entangled photons [169, 170]. A potential issue with single photon emission from NV centres is a low photon collection efficiency due to the lack of directional emission. Novel fabrication techniques may provide a solution; highly directional single photon emission was achieved by top-down fabrication of diamond nanowires containing individual NV centres [171]. The brush-like array of nanowires also show an order of magnitude greater single photon flux than an ultrapure bulk diamond sample, and at an order of magnitude lower pumping intensity. An alternative approach to directional emission could be to embed emitters in a dielectric antenna structure, as proposed in the study by Lee et al. [172].

NV centres are compatible with integrated photonic circuits; the study by Faraon et al. [173] demonstrates coupling of NV centre fluorescence to diamond-on-silicon waveguides and grating couplers, and the study by Gould et al. [174] shows coupling to waveguides via GaP microdisks. Further to this, the GaP system has been modified to allow the single photon emission frequency to be tuned by an applied bias voltage (Figure 7) [175]. This could compensate for the natural variation in emission frequencies from different NV centres. Femtosecond laser fabrication methods can produce photonic and microfluidic circuits in diamond [163, 176]. Importantly, these reports demonstrate the creation of NV centres on-demand using femtosecond laser pulses. Lenzini et al. give an overall review of progress in diamond integrated circuits for quantum photonics [177]. Together, these fabrication techniques show clear potential for diamond-based

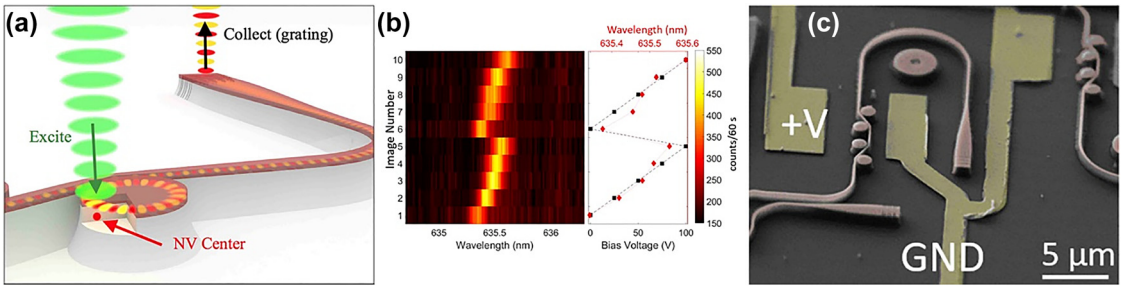

Figure 7: NV centre single photon emission coupled to GaP microdisks, with tuneable emission wavelength.
(a) Schematic of NV centre coupled to waveguide via a GaP microdisk. (b) Wavelength shift in single photons coupled into GaP microdisks from NV centres, in response to changing bias voltage Reprinted with permission from the study by Gould et al. [174]. Copyright (2016) by the American Physical Society. (c) SEM image of circuit. Pink: GaP microdisks and waveguides; Yellow: Ti/Au electrodes for applying bias voltage; Grey: diamond substrate. Reprinted with permission from the study by Schmidgall et al. [175]. Copyright (2018) American Chemical Society.

systems integrating single photon emitters and microfluidics in on-chip sensors; a potential platform for integrated quantum biosensors.

6.2 Quantum dots

Quantum dots (QDs) are semiconductors on the scale of a few nm in all three dimensions which have quantized electronic energy levels. QDs based on CdSe, CdTe and CdS are in widespread use as fluorescent markers in bio-assays and imaging [178], however these applications do not exploit the photon statistics of single photon emission from individual quantum dots. Therefore, we focus here on semiconductor QDs which would be suitable as sources of single photons in integrated biosensing devices.

Semiconductor-based single photon sources consisting of QDs in optical cavities have been studied extensively. These systems are typically based on GaAs and InGaAs semiconductor layers grown by molecular beam epitaxy (MBE), producing sources with second-order correlation functions as low as $g^{(2)}(0) = 10^{-4}$ [121, 122, 179]. QDs can also be integrated into photonic circuits based on silicon waveguides and fabricated using standard CMOS processes by a transfer printing method [180]. Quantum dots in photonic crystal cavities have demonstrated high-purity single photon emission [181, 182]; this work has even led to a commercially available on-chip single photon source using waveguides and grating couplers to extract photons [183].

Organic single photon emitters can be integrated with photonic circuits too; a single dibenzoterrylene fluorophore has been coupled to a silicon nitride waveguide, resulting in anti-bunched emission with $g^{(2)}(0) = 0.01$ [184]. In the same way as for diamond-based integrated devices, these techniques could provide a silicon-based platform for integrated quantum optical sensing devices exploiting emission from QDs or organic fluorophores. Opto-plasmonic enhancements might also be combined with QD systems, as shown by the demonstration of strong coupling of individual QDs with a plasmonic silver bowtie cavity [185]. Although photon correlation measurements on these systems have not yet been carried out, there is the interesting possibility of exploiting both single photon emission and sub-wavelength field localization in a quantum opto-plasmonic system.

6.3 Hexagonal boron nitride defects

Single photon emitters in 2D materials are attractive for achieving more efficient extraction of single photons as compared with emitters embedded in bulk materials. Candidates include defects in semiconducting transition metal dichalcogenides (TMDs) (for example WSe_2) and hexagonal boron nitride (hBN) single crystals [186]. While TMDs require low temperatures for efficient single photon emission, hBN defect centres have been shown to be chemically and thermally stable sources of bright single photon emission, at room temperature [187–189].

hBN single crystals are a 2D semiconducting material with a large band gap; almost 6 eV [188]. The large band gap is attributed to relatively easy formation of sub-band gap energy defects and highly suppressed non-radiative recombination, which contribute to the capability for room temperature single photon emission [186]. Defects responsible for single photon emission have been proposed to be nitrogen vacancies and anti-site nitrogen vacancies, in which one boron atom adjacent to the vacancy is substituted for nitrogen [188]. The photophysics of the defects is typically modelled using three- or four-level systems, which achieve good fits to experimental second-

order correlation functions [188, 191]. These defects can be generated with a high degree of control using oxygen plasma etching and thermal annealing. Wet chemistry techniques for transferring single crystals to substrates have also been developed [192].

Although the zero phonon lines of different emitters may range over 570–800 nm [187, 193], single photon emission from hBN defects can be spectrally tuned using strain [194–196], photodoping in ionic liquid devices [197] and temperature tuning methods [193]. Localization of emitters and some control over their polarization has been achieved using defects formed at wrinkles in hBN layers [198]. In order to exploit hBN centres in integrated devices, efficient extraction of single photons is required. Two works have shown coupling of hBN emission to optical fibres. One used a tapered fibre to couple single photon emission from hBN flakes with an efficiency of 10% [199]. The second-order correlation function at the output of the fibre was measured to be $g^{(2)}(0) = 0.15$. The other study used hBN flakes applied directly to the end of an optical fibre, resulting in an output correlation function of $g^{(2)}(0) = 0.18$ and an estimated coupling efficiency also around 10% [200]. It is also possible to fabricate on-chip photonic components directly out of hBN, for example photonic crystal cavities recently produced using reactive ion etching (RIE) and electron beam induced etching (EBIE) fabrication techniques [190] (Figure 8). In Figure 9, we give one of the scanned intensity maps as well as the second-order correlation measurement of a hBN sample. Unlike in diamond NV centres in which spins are currently exploited for magnetic field measurements, the spin properties of hBN defects are not yet well understood. This is partially due to the wide variety of defect types produced in typical hBN fabrication processes. However, magneto-optical effects using hBN defects have been theoretically predicted [201]. Magnetic field-dependent photoluminescence [202] and optical manipulation of defect spins [203] have now been observed in hBN, raising the possibility of 2D material-based magnetometers in the future.

6.4 Non-linear optical quantum sources and resonators

Non-linear optical processes provide a means of generating non-classical states of light and are in widespread use as sources in quantum sensing schemes. The polarization response of an optical medium can be expanded in powers of the incident light field:

$$P_i = \epsilon_0 \chi^{(1)} E_i + \epsilon_0 \chi^{(2)}_{ijk} E_j E_k + \epsilon_0 \chi^{(3)}_{ilmn} E_l E_m E_n + \cdots,$$

where $\chi^{(n)}$ is the nth-order susceptibility of the medium and summation over the indices j, k, l, m, n is implied.

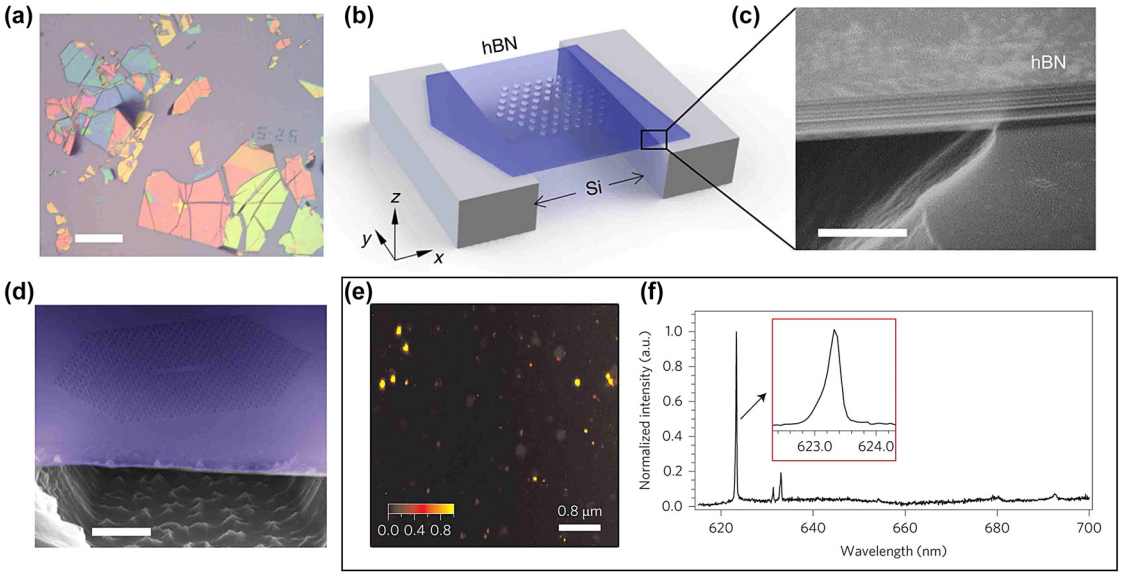

Figure 8: Quantum emitters in hexagonal boron nitride (hBN) and on-chip fabrication using hBN.
(a) Optical image of hBN flakes, scale bar 50 µm. (b–d) Schematic and SEM images of a photonic crystal cavity fabricated in a suspended multilayer hBN flake, scale bars: 500 nm in (c), 2 µm in (d). Adapted from the study by Kim et al. [190], available under Creative Commons Licence. (e and f) Photoluminescence map of quantum emitters in hBN and photoluminescence spectrum of a single emitter taken at 77 K. Reprinted by permission from Springer Nature: Nature Nanotechnology [188], copyright (2016).

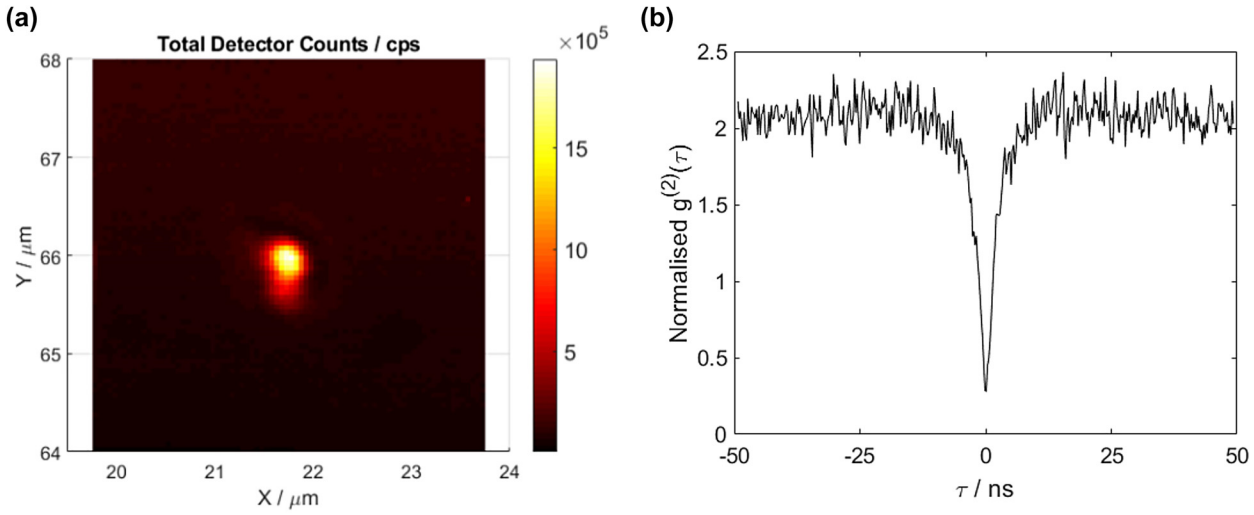

Figure 9: Photon characterization of quantum emission from hexagonal boron nitride (hBN).
(a) Scanned intensity map of emission from hBN sample at around 570 nm, excited at 532 nm. (b) The second-order correlation $g^{(2)}(\tau)$ function, the $g^{(2)}(0)<0.5$ indicates single photon emission.

Therefore, media with non-zero susceptibilities at second order and higher can support interactions between optical fields at different frequencies. Most common are second- and third-order non-linear interactions, or three- and four-wave mixing, respectively. Only non-centrosymmetric crystals have a non-zero $\chi^{(2)}$ and can support three-wave mixing, also known as spontaneous parametric down-conversion (SPDC) when a single pump frequency is split into two lower frequencies [204]. Centrosymmetric crystals and amorphous media can have non-zero $\chi^{(3)}$ but a high susceptibility coefficient is desirable otherwise high pump power is needed for efficient non-linear processes to take place. From a quantum optics perspective, the SPDC non-linear process represents a pump photon being annihilated and a pair of photons created. Non-linear processes are of interest in quantum optics because of the quantum correlations between these paired output photons.

Monolithic non-linear crystals can be integrated in on-chip devices as waveguides, or non-linear cavities can be used, often ring resonators supporting whispering gallery modes (WGM). Whispering gallery mode resonators (WGMRs) have high Q-factors which enhance the efficiency of non-linear conversion processes in WGMRs fabricated from non-linear optical media [205]. Integrating sources of non-classical photon states with other components in photonic circuits is currently of great interest, and the role of non-linear media in this area is covered in the review by Caspani et al. [119]. Waveguides and resonators fabricated from second-order ($\chi^{(2)}$) non-linear materials can produce photon pairs via spontaneous parametric down conversion (SPDC).

Periodically poled lithium niobate ($LiNbO_3$) waveguides have been developed as photon pair sources [206] and as sources of polarization-entangled photon pairs by Type-II SPDC [207, 208]. The computational results of

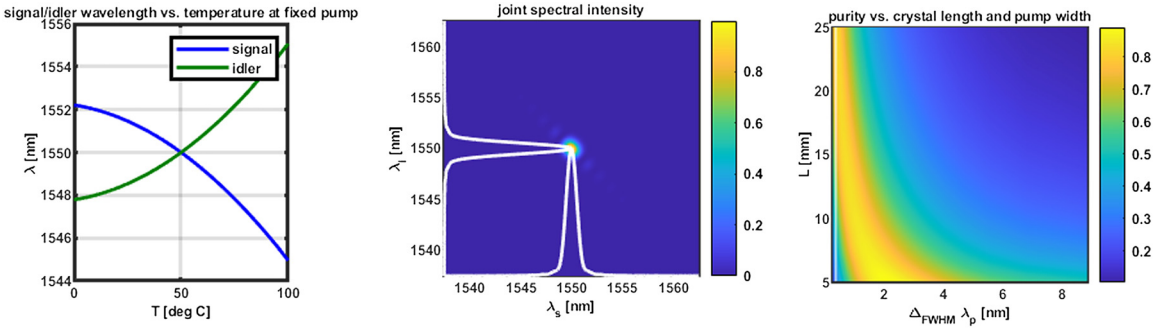

Figure 10: Computational analysis of joint spectral intensity and quantum purity of spontaneously parametric down converted photon pairs. A Type-II SPDC in PPKTP crystal is used as the source for the generation of polarization quantum entangled photon pairs. The pump photon wavelength used here is 775 nm, which gives rise to degenerate signal and idler photons at the communication wavelength of 1550 nm.

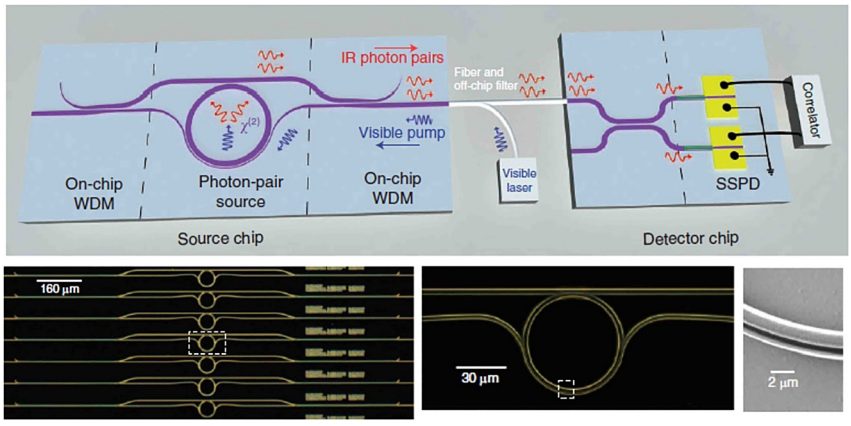

Figure 11: Aluminium nitride micro-ring parametric-down conversion source of correlated photon pairs.
An on-chip source of correlated photon pairs made from an aluminium nitride waveguide on a silicon substrate was coupled to superconducting nanowire single photon detectors (SNSPDs) on a separate chip. High purity heralded single photons were measured using this on-chip setup, showing $g^{(2)}(0) = 0.088 \pm 0.004$. Adapted from the study by Guo et al. [214].

the joint spectral intensity as well as the quantum purity estimation of SPDC photon pairs from a 25 mm long periodically poled KTP crystal at a temperature of 50 °C in Type-II phase matching condition is shown in Figure 10. Lithium niobate microdisks have been used to generate entangled pairs which are also shown to be individually quadrature squeezed [107, 209]. Periodically poled lithium niobate microdisk resonators are capable of ultra-bright photon pair generation; a pair generation rate of 36.3 MHz was achieved using only 13.4 μW pump power in the study by Ma et al. [210]. The wavelength of emitted photon pairs can be tuned, for example using thermal and electro-optic tuning. The tuning of photon pair wavelengths to alkali atom hyperfine transitions is demonstrated in the study by Schunk et al. [211]. Alternative $\chi^{(2)}$ materials include GaAs [212] and AlGaAs [213], both of which have been used to implement waveguide sources of polarization-entangled and counter-propagating photon pairs, respectively. Further to this, an aluminium nitride micro-ring integrated with superconducting single photon detectors via waveguides was demonstrated (Figure 11) in the study by Guo et al. [214]. This demonstrates the potential for quantum optical devices to be completely integrated with both sources and sensors on a chip, although the detectors in this case are mounted on a separate chip in a cryostat.

Examples of quadrature-squeezed light generation in integrated photonic devices are included in the studies by Vaidya et al. and Zhao et al. [215, 216], both of which use four-wave mixing processes in silicon nitride micro-resonators. Squeezed light generation in a room temperature optomechanical cavity was also achieved recently. Rather than using a non-linear optical medium, this system uses effective non-linearity due to the optomechanical interaction to achieve squeezing and has the potential to be miniaturized [217].

Non-linear effects can also be achieved in centrosymmetric materials, using $\chi^{(3)}$ processes such as four-wave mixing. An AlGaAs waveguide photon pair source is one example [218]. Silicon-based waveguide sources have also been developed [219], including sources of polarization entangled pairs [220]. More complex quantum optical states have recently been produced on-chip, such as four-photon states [221] and on-chip sampling of states with up to eight photons [222]. Due to their potential application to quantum communications, photon pair sources based on silicon micro-ring and micro-disk resonators have been extensively studied [223–231]. Further to this, silicon micro-ring sources have been developed with higher degrees of photon entanglement including time-energy entanglement [232–234] and hyper-entanglement (polarization and time-energy) [235]. Simultaneous generation of photon pairs in two communications frequency bands (1310 and 1550 nm) was demonstrated in [236]. Other materials that have been investigated as $\chi^{(3)}$ WGMR photon pair sources include silicon nitride [237], and recently, indium phosphide membrane micro-rings [238]. A further step towards fully integrated devices is the demonstration that the pump laser could also be placed on a chip. In a work by Wang et al. [239], an electrically injected wafer scale hybrid silicon laser was shown to have comparable performance to a stand-alone laser when pumping a silicon micro-ring photon pair source. Therefore, integrated photonic devices with pump lasers, photon pair sources and single photon detectors all on-chip now appear feasible. The material systems presented here provide sources of non-classical light states: single photons, entangled photon pairs and squeezed light, all with the potential for integration on-chip. Room temperature operation, which is required for integrated sensors in close proximity with biological samples, is offered by all these systems.

6.5 Quantum optical frequency combs

Quantum optical frequency combs (QOFC) combine the advantages of a light source with a large number of phase

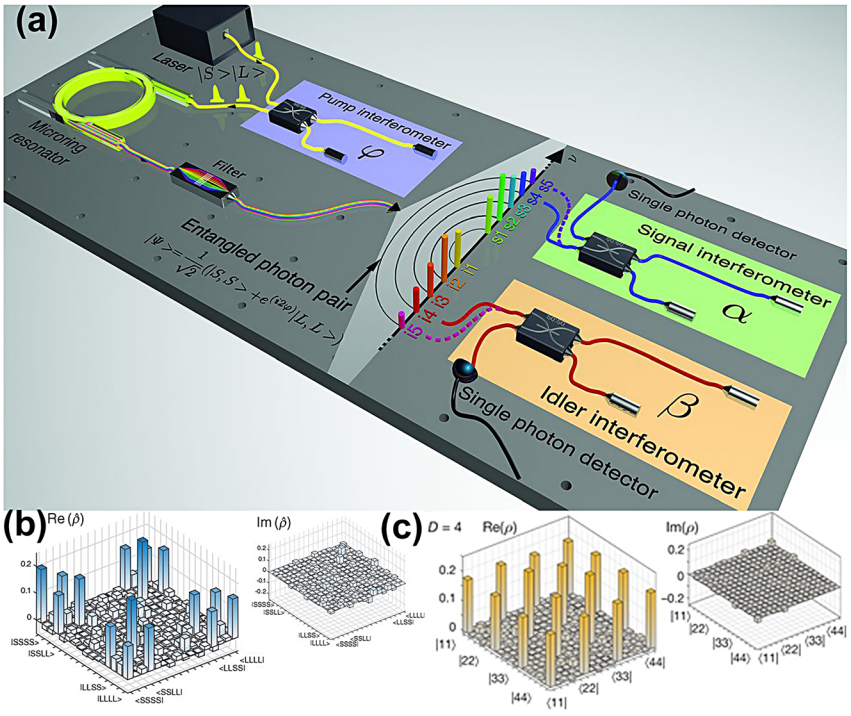

Figure 12: Integrated generation of time bin multi-photon entangled state in quantum frequency comb through spontaneous four wave mixing (SFWM) [240, 249, 250]. (a) Experimental scheme for generating time-bin–entangled photon pairs on a frequency comb through SFWM based on a micro-ring resonator. Adapted from the study by Reimer et al. [249]. Reprinted with permission from AAAS. (b) Measured density matrix of 4-photon qubit state where achieved fidelity was 64%. Adapted from the study by Reimer et al. [249]. Reprinted with permission from AAAS. (c) Higher-dimensional entangled state generation showing the measured density matrix with quidits, $D = 4$ where achieved fidelity was 76.6%. Reprinted by permission from Springer Nature: Nature [250], copyright (2017).

stable frequency modes of an optical frequency comb (OFC) as well as the photon output embedded with the non-classical quantum property of time-energy entanglement. Because of this peculiar property QOFCs have attracted great interest for on-chip applications such as molecular spectroscopic finger printing as well as to store and process large amounts of quantum information in frequency and time correlations in addition to joint spectral amplitude and phase [240–243]. OFCs were basically originated as mode locked lasers with optical pulses generated by coherent addition even up to millions of resonant longitudinal optical cavity modes resulting in output optical modes which are harmonically related and phase coherent [244–246]. OFCs have evolved further with wide band width with the advent of non-linear optical fibers (erbium- and thulium-doped fibers)-based super continuum sources [245]. For the on-chip integration of OFCs with very broad spectra, either supercontinuum generation in optical waveguides or Kerr-comb generation in microresonators are widely used [247].

By means of spontaneous four wave mixing (SFWM) Reimer et al. demonstrated a CMOS compatible micro-ring resonator-based integrated frequency comb source of heralded photon pairs with 200 GHz channel separation and 110 MHz line width [248]. Subsequently, multi-photon entangled quantum states by means of in a QOFC in four-port micro-ring resonators were realized demonstrating how Kerr frequency combs can be well suited to generate several bi- and multi-photon entangled qubits [249] (Figure 12a and b). The micro-ring resonator of this QOFC was pumped with a passive mode-locked fiber laser with a repetition rate of 16.8 MHz and a pulse width of 570 ps. A stabilized unbalanced fiber interferometer with an 11.4 ns delay was used to generate time-bin–entangled qubits where double pulses of equal power were produced with a defined relative phase difference [249]. Further, on chip generation of the higher-dimensional entangled states is also being realized where the photons were created in a coherent superposition of multiple high-purity frequency modes (Figure 12c) [240, 243, 250].

7 Quantum photonic/plasmonic sensing and imaging

7.1 Solid-state spin-based quantum sensing

Quantum sensors based on solid-state spins have demonstrated single molecule resolution [251] and quantum coherence over a large range of temperatures [252], which makes them favourable for applications in the life sciences. High spin-state colour centres arise because of point defects in the bulk structure of wide band gap semiconductors. An important example is the negatively charged nitrogen-vacancy (NV) centre in diamond which consists of a substitutional nitrogen impurity adjacent to a missing carbon atom. NV centres have been integrated into

many sensing devices and provide the fundamental mechanism for quantum-based magnetometry [93, 253, 254], thermometry [255, 256] and quantum-enhanced biosensing [257, 258] applications. Petrini et al. discuss the theory of quantum sensing with NV centres in more detail [259], whereas this section provides a summary of the main aims and challenges for solid-state spin-based quantum biosensing.

The electronic structure of group IV defects affects the performance of the sensor. The NV centre is a favourable choice because it features a spin-split ground state accessible by microwave fields, long electron spin coherence times over a large range of temperatures and an internal dynamic that allows for spin initialization and read-out using off-resonant lasers. The performance of the sensor can be further improved in combination with advanced techniques to optimize the spin dephasing time, the readout fidelity and fabrication processes of the NV-based sensor. The optimization techniques for NV diamond magnetometry are reviewed extensively by Barry et al. [260]. Other group IV defects in diamond have also been explored for quantum sensing and are reviewed by Bradac et al. [261]. A promising candidate is the silicon vacancy in diamond, which shows superior spectral properties compared to the NV centre, but an inherently shorter electron spin coherence time [262].

The sensitivity of an NV quantum sensor depends on the location of the NV defect in the lattice. NV centres are most sensitive at or near the surface of the lattice, where it is closest to the sensing target, but quantum coherence is preserved over longer time scales in the lattice bulk. The compromise is between the sensitivity and quantum coherence of the sensor. The direct coupling of an NV centre to nearby spin magnetic dipoles scales as r^{-3}, where r is the distance [263] and for scanning magnetometry applications, r also directly sets the spatial resolution [28]. The resolution can be improved without changing the depth of the NV centre in the lattice by coupling the NV centre to electronic spin-½ qubits on the surface of a high-purity diamond crystal. With proper quantum control, surface electron spins can be coherently manipulated and measured to detect individual proton spins with angstrom resolution [264]. More recently, NV-based sensors have been designed to provide vectorized resolution, for sensing applications in more than one dimension [265].

The fabrication technique also plays an important role in producing stable, high-quality NV centres near the diamond surface. Recently, a new fabrication method has been tested, using plasma immersion ion implantation (PIII) to produce high-quality shallow layers of NV-centres [266]. In conventional NV-centre implantation, accelerated ions penetrate the diamond lattice, causing damage to the shallow layers, which prevents the NV centres from forming. The PIII technique utilizes simultaneous implantation and etching resulting in a shallow good quality implantation layer. Using this fabrication method, most NV centres are within 3.6 nm from the diamond surface and the estimated magnetic sensitivity is around $2.29\,\mu\mathrm{T}/\sqrt{\mathrm{Hz}\cdot\mu\mathrm{m}^{-2}}$. The creation efficiency of NV ensembles can be further improved by high temperature annealing in vacuum [267] and the stability of the NV charge state can be fine-tuned using different temperatures during the nano-diamond growth period for tailored applications [268].

Improving the performance of solid-state spin-based quantum sensors relies on optimizing the quantum state initialization and readout techniques and finding efficient polarization transfer techniques from electron to nuclear spin. The nuclear hyperpolarization of molecules near or at the surface of a quantum sensor is the basis for nanoscale nuclear magnetic resonance spectroscopy. NV centres in diamond are favourable over other types of quantum defects because the electron spin can be optically initialized almost perfectly even at room temperature. However, it remains a challenge to maximize the dynamic nuclear polarization for the quantum manipulation and detection of small nuclear spins. Some of the most recent approaches to dynamic nuclear polarization include a new PulsePol technique [269] and magic-angle spinning with arbitrary wave-form pulse shaping [270]. Lei et al. also developed a new set of steering pulse sequences for manipulating the quantum coherence times of NV centres [271].

The readout fidelity of a solid-state spin-based quantum sensor can be enhanced by repeating readouts, as described in the quantum sensing protocol. However, the number of repeated readouts is limited by measurement backaction, which changes the quantum state that is measured. Coupling the NV centre electronic spin to its associated ^{15}N nuclear spin minimizes the measurement backaction effect and results in up to a 13-fold enhancement of the readout fidelity over conventional readout methods [272]. In the case where continuous microwave pulses are used for nuclear magnetic resonance spectroscopy, the readout fidelity can further be improved with quantum logic [273]. Data science deconvolution techniques have also been used to sharpen the readout signal. Aharon et al. demonstrate a deep learning discrimination scheme that outperforms Bayesian methods when verified on noisy nuclear magnetic resonance spectroscopy data [274].

For practical applications, it is important that the sensing technology can be integrated into ultra-compact and scalable platforms. Kim et al. demonstrate a chip-scale

quantum sensor, which combines NV-based quantum sensing with complementary metal-oxide-semiconductor technology [275]. All the components required for NV-based magnetometry are stacked into a compact 200 × 200 μm footprint. The sensor measures external magnetic fields with a sensitivity of 32.1 $\mu T/\sqrt{Hz}$, with the potential to be improved even further. Another exciting design for NV-based magnetometry is the distributed quantum fibre magnetometer, which allows for distributed magnetic sensing capabilities over extended lengths with a sensitivity of 63 ± 5 $nT/\sqrt{Hz}$ per site [276].

7.2 From surface plasmons to quantum plasmonic sensing

Plasmon-based sensors are important in biology because they can monitor real-time molecular binding events [277]. Plasmonic sensors typically fall into two main categories; those that are based on propagating surface plasmons and those that are based on localized surface plasmons as shown in Box 4. More recently, with the motivation to reach unprecedented sensitivities, the blueprints for plasmonic-based sensors have become more diverse. Some notable examples are discussed in this section and include hybrid plasmonic-photonic structures and plasmonic structures irradiated with quantum sources of light.

Surface plasmons cannot be directly excited by photons due to the large wavenumber mismatch. Instead, light must be coupled to surface plasmons through a dielectric medium with a high dielectric constant to increase the momentum of the incident light. Traditionally, this is achieved using the Kretschmann-Raether (K-R) configuration [278], whereby the incident light is coupled to a metal film through a glass prism or substrate. Figure 13a and b show adaptations to the traditional K-R configuration that improve the performance of the sensor. Figure 13a shows an example of a sensing device with a wide tunability due to the strong dispersion of hybrid lattice plasmon modes [279], which are a result of patterning the surface with an array of cylinders. Figure 13b shows an example of a sensor that uses optical fibres instead of a prism to couple light to surface plasmons and has the advantage of a more compact configuration for in situ analysis [280]. A comprehensive review of fibre-optic sensors based on the surface plasmon resonance can be found here [284].

The distinctive optical properties of propagating and localized surface plasmons are even more prominent when combined with other optically resonant processes [285], such as Raman spectroscopy [286] or photonic microcavities [146]. In Raman spectroscopy, the near-field signal can be enhanced by introducing plasmonic nanoparticles into the experimental set up, either through core–shell nanoparticles and coated nanostructures [287]; tip-enhanced Raman spectroscopy (TERS) [288] or shell-isolated nanoparticle-enhanced Raman spectroscopy (SHINERS) [289, 290]. Of these, SHINERS has very wide applicability as it can be used for surfaces with any composition and morphology, whereas this is a limitation with the other surface-enhanced Raman spectroscopy techniques [291].

Plasmonic nanostructures combined with optical microcavities or photonic structures also demonstrate extraordinary sensing capabilities. An extensive review of the diverse range of plasmonic-photonic architectures is discussed by Xavier et al. [146]. Some notable examples include WGM resonators coupled to plasmonic nanoparticles, as shown in Figure 13c [281], whereby single molecules in the near field of the resonator can be detected through a resonant frequency shift of the modes [292]. This type of sensor has been used to study single molecules [147, 293] and the conformational dynamics of single proteins, such as DNA polymerase [294]. Another type of plasmonic-photonic nanosensor is shown in Figure 13d and is based on a dielectric photonic microstructure acting as an antenna, which efficiently funnels light towards a plasmonic transducer to enhance the detection sensitivity [282]. This sensor achieves single molecule sensitivity down to 4 zg, which allows this sensor to be used as an optical molecular weighing scale.

Recently, there has also been an interest in hot electron plasmonics for sensing applications [295]. Plasmon decay generates hot electrons, which can be used as a sensing signal if the rate of hot electron generation and collection is faster than the rate of energy dissipation by electron-phonon scattering [296]. Wang et al. propose a sensing device based on the signal from hot electrons, rather than traditional optical measurement, to simplify the conventional sensing configuration [283]. The schematic is shown in Figure 13e and consists of a planar Au-TiO_2-Ti microcomb structure with 64 Schottky diodes connected in parallel on one 10 mm chip. The sensitivity of the device and the limit of detection are estimated to be 1.87×10^{-4} RIU/nA and 4.13×10^{-3} RIU, respectively. Although these values are not at the known fundamental limits of detection, they are feasible for chemical and biosensing applications, whilst using a very simple lab-on-chip setup.

Since the realization that propagating and localized surface plasmons can transduce squeezed states of light [297, 298], the field of quantum plasmonic sensing has been rapidly expanding. Squeezed states of light suppress the statistical noise in either the amplitude or phase of an

Box 4

Propagating and localized surface plasmons

A plasmon is the quasiparticle associated with plasma oscillations and can be excited by an electromagnetic field incident on a material with free charges, such as the valence electrons in a metal. Surface Plasmons Polaritons (SPPs) are light-coupled plasmon excitations that are confined at the boundary between two materials, typically a metal-dielectric interface as shown in Figure B4a, and their propagation is described by slow electromagnetic eigenwaves [70]. SPPs exhibit strong energy confinement at the interface, which makes them very sensitive to the surface condition. When an SPP is confined to a particle with dimensions comparable to the wavelength of light, the plasmon oscillates locally around the nanoparticle, as shown in Figure B4b, and the maximum near-field enhancement occurs at the localized surface plasmon resonance. The frequency of the resonance is highly sensitive to perturbations in the local refractive index of the surrounding medium. The high sensitivity of propagating and localised surface plasmons to changes in the near-field makes them ideal for sensing applications [71].

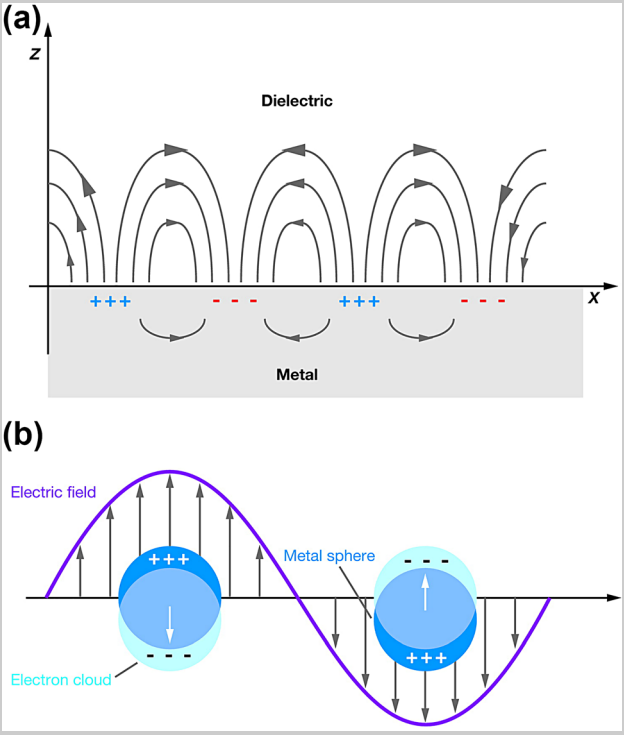

Figure B4: Schematic diagrams illustrating (a) a surface plasmon polariton (or propagating plasmon) and (b) a localised surface plasmon. Adapted from the study by Willets and Van Duyne [72].

The quantum mechanical description of surface plasmons can be obtained through the quantization of their respective electromagnetic fields. The basic approach is summarised in the paper by Tame et al. [73] and is broken down into three main steps: (i) classical mode description, (ii) discretization of classical modes and (iii) quantization via the correspondence principle.

optical field at the expense of increased noise in the respective conjugate variable. For plasmonic sensing applications, this quantum property of the optical field can be exploited to detect refractive index changes that would have otherwise been lost in the classically optimized system [156]. A comparison of different specialized quantum states, namely the two-mode squeezed displaced state; the two-mode squeezed vacuum state and the twin Fock state, reveals that all of them can provide a quantum advantage to some extent depending on the parameter regime [299]. Another advantage of quantum plasmonic sensors, specifically for applications in the biosciences, is that they can achieve the same sensitivity as their classical counterparts, but with less optical power, which reduces the chances of damaging the biological specimen under investigation [300].

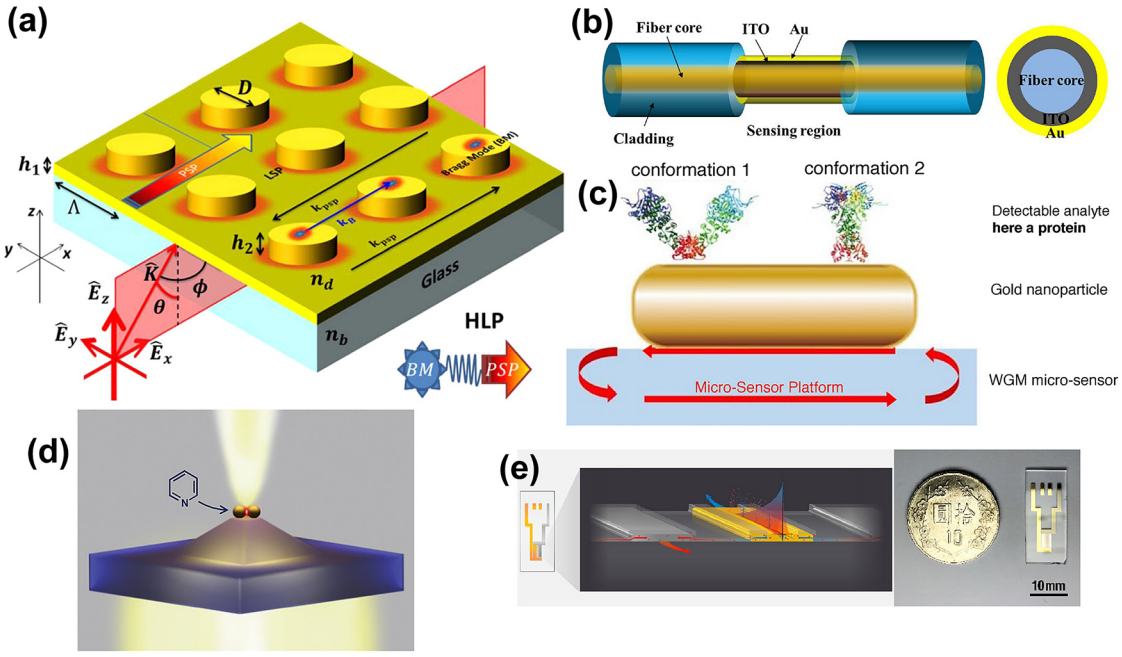

Figure 13: The diverse blueprints for plasmon-based sensing.
(a) Sensing device with a wide tunability due to the strong dispersion of hybrid lattice plasmon modes. Adapted from the study by Sarkar et al. [279]. Copyright © 2015, American Chemical Society. (b) A compact plasmonic sensor for in situ analysis based on photon-plasmon coupling with fibre-optics. Adapted from the study by Li et al. [280]. © The Optical Society. (c) Plasmonic nanoparticle coupled to whispering gallery mode (WGM) for single molecule detection. Adapted from the study by Frustaci and Vollmer [281] under Creative Commons Attribution 4.0 International License. (d) Molecular weighing scale with single molecule sensitivity down to 4 zg. Adapted from the study by Proust et al. [282]. Copyright © 2019, American Chemical Society. (e) Convenient lab-on-chip design for a plasmonic sensor based on hot electrons. Adapted with permission from the study by Wang et al. [283].

The quantum nature of plasmons has been observed through numerous experiments, which have been reviewed by Tame et al. [73]. The quantum properties of plasmons include the survival of entanglement; quantum decoherence and loss; wave-particle duality; the quantum size effect and quantum tunnelling. The quantum description of propagating or localized surface plasmons comes from the quantization of the classical modes for the system and can include the effects of loss with either the microscopic Hopfield [301] or macroscopic Green's function formalism [302]. Including the effects of loss is important for understanding the mechanism for hot carrier generation, which, for biosensing applications, can influence the behaviour of molecules adsorbed to the surface of a quantum plasmonic sensor [295].

Plasmons can also be modelled computationally with varying levels of approximations, depending on the scale of the plasmonic system and geometry considered. For plasmonic nano-gap structures, Zhu et al. assess the appropriate level of theory, based on the size of the nanogap [303]. Fully quantum calculations using time-dependent density functional theory are computationally intensive and are reserved for plasmonic structures with a size $\lesssim$10 nm. In another computational study, the plasmonic properties of a 55-atom silver nanoparticle are simulated using real-time time-dependent density functional theory [304] and the dominant channels for hot-carrier generation are identified, providing a greater insight into plasmon decay mechanisms in quantum plasmonics.

Having given a brief introduction to the field of quantum plasmonics, this section continues with specific examples of quantum plasmonic metrology in the biosciences. Zhou et al. highlight that the field of quantum plasmonics is now moving from fundamental science towards technological applications [290]. Examples of quantum plasmonic devices with potential biosensing applications are summarized in Figure 14. The blueprints for quantum plasmonic sensors are diverse, but some common themes include using quantum states of light with classical detectors, integrating coherent photon-plasmon conversion processes and/or using the quantum tunnelling property of plasmonic nanogap structures. Plasmon rulers exploit the quantum tunnelling property of coupled

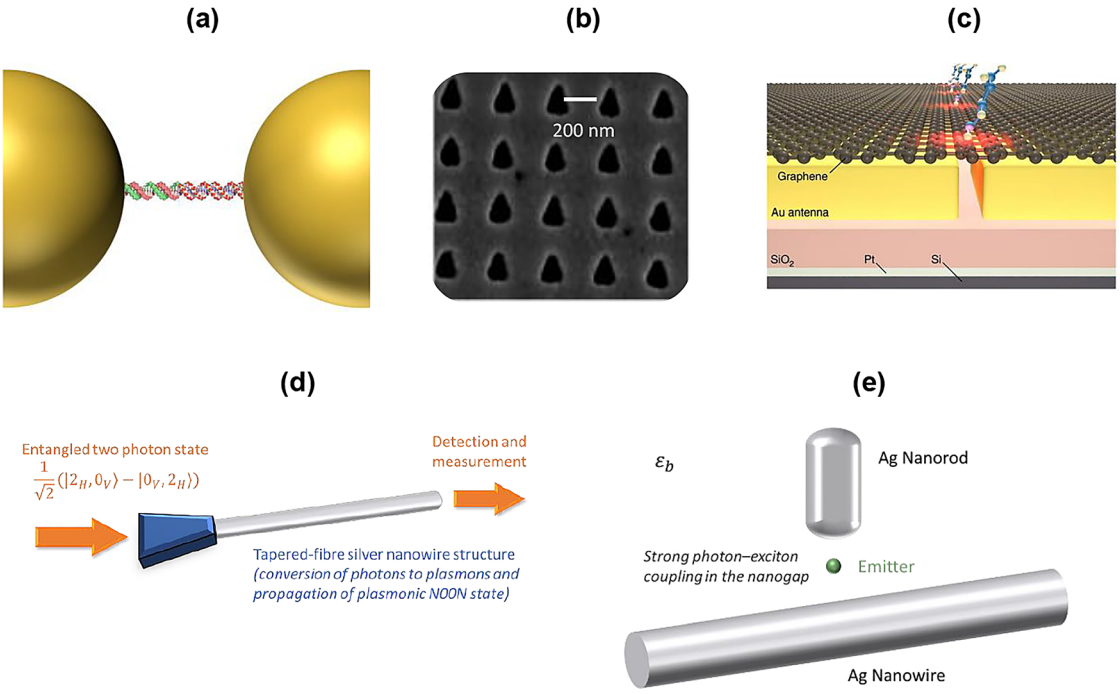

Figure 14: (a) DNA linker in a plasmonic nanoparticle dimer increases the range of coherent charge transfer. Adapted from the study by Lerch and Reinhard [305] with DNA linker illustration by David S. Goodsell and the RCSB PDB under CC-BY-4.0 license. (b) Plasmonic metasurface increases the conversion efficiency between photons and plasmons for quantum plasmonic detection schemes. Adapted with permission from the study by Dowran et al. [156] © The Optical Society. (c) Hybrid quantum-limited sensor that takes advantage of multiple features from plasmonic, electronic and spectroscopic approaches to maximize sensing capabilities. Adapted from the study by Zhu et al. [306] under Creative Commons Attribution 4.0 International License. (d) Using quantum states of light in plasmonic sensing schemes; plasmonic N00N state in a silver nanowire. Based on the study by Chen et al. [300]. (e) Theoretical proposal for strong coupling between a silver nanowire and silver nanorod across a plasmonic nanogap. Based on the study by Qian et al. [307].

plasmonic dimers, which consist of two metal nanoparticles separated by a nanoscale gap. The quantum tunnelling regime occurs at dimer separations, S, below which the tunnelling-induced conductance becomes large enough to allow a significant fraction of the plasmon-induced surface charges to tunnel across the gap in half an optical cycle ($S \lesssim 1$ nm) [303]. The concept behind the plasmon ruler is to increase the quantum tunnelling range by connecting the nanoparticle dimer with a DNA linker. This introduces bond tunnelling, which promotes direct charge exchange between the nanoparticle dimer. Lerch and Reinhard [305] demonstrate that by tethering the nanoparticle dimer with a DNA linker, as shown in Figure 14a, the range of coherent charge transfer can be extended to dimer separations of $S \approx 2.8$ nm. The plasmon ruler is highly sensitive to changes in the tunnelling current due to ion or protein binding to DNA, which provides a new concept for quantum plasmonic biosensing.

Quantum-enhanced plasmonic sensors can also be realized by using quantum states of light. Dowran et al. use a two-mode squeezed displaced state of light (bright entangled twin beams) to demonstrate a quantum-enhanced surface plasmon resonance sensor [156]. A four-wave mixing process is used to generate a probe beam and a conjugate beam. The conjugate beam is sent to a photodetector for a reference intensity measurement, whilst the probe beam passes through the plasmonic sensor for the sample measurement, before arriving at the second photodetector. The plasmonic sensor is patterned by an array of triangular nano-holes, as shown in Figure 14b, and is designed to provide coherent conversion between photons and plasmons, whilst preserving the quantum properties of light. The intensity difference between the measurement and reference beams is subtracted, before passing to a spectrum analyser to demodulate and measure the refractive index shift from the plasmonic sensor. Using this method, it is possible to achieve sensitivities on the order of 10^{-10} RIU/$\sqrt{\text{Hz}}$.

Another example of a plasmonic sensor that utilizes quantum states of light is presented by Chen et al. [300]. The experimental setup is similar to Dowran et al. [156], but the plasmonic nanohole array is replaced by the tapered-fibre

silver nanowire structure shown in Figure 14d. The structure can efficiently convert between photons and plasmons [308]. Chen et al. experimentally verify that polarization entangled photon pairs can excite a plasmonic N00N state in the silver nanowire and propagate over a distance of 5 μm before reconverting back into photons, whilst preserving high-quality entanglement throughout. They also assess the potential for the device to be used for super-resolution and super-sensitivity measurements and find that after quantifying the losses in the experimental setup, the sensor does not quite meet the criteria for these measurements. Chen et al. suggest that with a twofold coincidence measurement for the two-photon state input and a few improvements to the experimental setup, it would not be impossible to achieve super-sensitivity in the future.

Hybrid sensors take advantage of multiple features from plasmonic, electronic and spectroscopic approaches to maximize sensing capabilities. Zhu et al. demonstrate a hybrid meta-surface sensor with quantum-limited measurement for monolayers of sub-nanometer-sized particles and affinity binding-based quantitative detection of glucose down to 200 pM [306]. They further demonstrate enhanced fingerprinting of minute quantities of glucose and polymer molecules. The metasurface architecture is shown in Figure 14c and shows a monolayer of graphene suspended above a gold nanorod antenna array. The nanoantenna array sits above a platinum mirror, separated by a quartz spacer layer. The sensor operates in air, but there are challenges to integrate the sensor with microfluidic channels due to the stability of monolayer nanomaterials.

Qian et al. propose a sensor based on the strong photon-exciton coupling in a plasmonic nanogap between a silver nanowire and silver nanorod [307]. The proposed setup is shown in Figure 14e. They choose to define the sensitivity of the strongly coupled photon-exciton system according to the Rabi splitting of energy, rather than by the plasmon resonance shift, as it can be directly linked to the dipole moment of the emitter and the electric field corresponding to a single excitation of the silver nanorod. By optimising these parameters for the system, they show that the sensitivity of the quantum plasmon sensing system can exceed that of the traditional plasmon sensing system, which in principle only depends on the resonance spectral shift. Their scheme is yet to be experimentally realized.

Recently, there has been a growing interest in plasmonic strong coupling [309], including sensors based on the strong coupling between plasmonic modes and the optical modes of single emitters [310]. This type of sensor confines light to micro-to pico-sized cavities or gaps, whereby the walls of the cavity are surfaces that support localized or propagating surface plasmon modes. The emitter is positioned inside the cavity or in between the two walls of the nano-gap, such that the optical modes of the emitter can interact with the plasmonic modes of the cavity. The strong coupling regime occurs when the plasmonic and emitting system have overlapping resonant eigenmodes and the strong coupling leads to new hybrid eigenmodes that are distinct from either the individual emitter or plasmonic modes. Plasmonic biosensors based on strong coupling have the potential to achieve superior sensitivity with lower optical power in comparison to the weak coupling case, due to the extreme confinement and amplification of light within the cavity or nano-gap structure.

Several experiments have shown strong coupling in systems that combine plasmonics with photon emitters [80, 311] or quantum dots. Leng et al. assess the properties of a plasmon-emitter system, consisting of a single colloidal quantum dot in the gap between a gold nanoparticle and a silver film [312]. Their results suggest that, in practice, the strong coupling regime is difficult to achieve for this system, since strong coupling is measured for less than 1% of the samples. In a different study, Santhosh et al. investigate strong coupling in plasmonic bowtie-quantum dot systems [185]. Their results show that they were close to achieving strong coupling in the case of a plasmonic bowtie with a single quantum dot. These examples demonstrate the importance of having a consistent definition for strong and weak coupling to compare different experimental results. Pelton et al. propose a uniform method for evaluating and quantifying strong coupling from the scattering spectra, which they derive from strong plasmon-exciton coupling theory [310]. Their analytical expressions can be used to reliably distinguish between Rabi splitting and exciton-induced transparency.

Computational methods are very useful for studying strong coupling in plasmon-emitter systems and can be used to accelerate research in this field. Classical electromagnetism simulations, using finite-difference time-domain methods or finite element methods, have been used to predict and optimize plasmonic-emitter configurations that would lead to strong coupling before doing experiments [313–315]. The strong coupling regime has also been explored with ab initio computational methods, which model the many-electron interactions of the system. Rossi et al. predict strong coupling between a 201-atom aluminium nanocluster and the molecular resonance of benzene [316]. Ab initio methods can capture the relevant interactions at the quantum level of theory and the relevant electronic transitions can be visualized with additional tools, which provide a greater insight into strong coupling mechanisms.

The strong coupling regime by plasmonics opens new prospects for single molecule detection and quantum optical biosensing. Ojambati et al. [96] recently showed that, with a few additional experimental considerations, it is possible to achieve strong coupling for a molecule-plasmonic system, which is considerably more challenging than for quantum dots due to the Stokes-shifted emission process and the range of vibrational modes. Their results show wavelength-dependent photon statistics in molecular systems, arising from a combination of biexciton excitation, photon-induced tunnelling and multiple excitations of the emitter. These results already show promise for future quantum biosensing applications.

7.3 Quantum-limited single molecule sensors

Tapered optical fibres, or nanofibers, are produced by pulling a single mode optical fibre with heating to reach diameters of hundreds of nm. They have previously been used to achieve nanoparticle trapping [317] (providing higher trapping forces than conventional optical tweezers) and single nanoparticle detection [318]. Mauranyapin et al. have extended the capabilities of fibre sensors to detecting nanoparticles and single biomolecules with quantum-limited precision, by using a heterodyne sensing technique [155]. Silica nanospheres down to 5 nm radius and single BSA (bovine serum albumin) molecules with 3.5 nm Stokes radius were detected in this setup. Dark-field illumination from a probe beam perpendicular to the fibre sensor is scattered by nanoparticles in the fibre's evanescent field and modulated by a local oscillator propagating in the fibre (Figure 15). The high sensitivity detection was achieved by a heterodyne measurement, balanced at the detector by the pure local oscillator. This measurement scheme was recently developed to use an exposed core fibre sensor [319]. These sensors are more robust (around 120 µm diameter; compared with 500 nm tapered fibres) and can be produced with much longer sensing regions than the <1 mm provided by the previous setup. Detection of silica nanospheres down to 25 nm radius was demonstrated, but using an order of magnitude lower light intensity than the previous technique. The low light intensity used in these experiments is an important feature; since it is up to two orders of magnitude lower than quoted photodamage thresholds these schemes are promising for the observation of biological systems over long timescales.

Crucially, both experiments [155, 319] demonstrate that noise in the system follows a linear scaling with local oscillator power, consistent with quantum-limited noise (Figure 15c). Therefore, these sensors operate at the fundamental limit for a coherent light probe, i.e. are shot-noise-limited. Although sensitivity may be improved by using higher light intensities, this scaling will remain a limit for the technique. Exceeding this performance, as stated in Ref. [155], would require the use of quantum correlated photons.

7.4 Prospects of ultra-sensitive detection with optoplasmonic sensor

State of the art optical label-free micro- and nanosensors are developed to enable the detection of biomolecules at the level of single molecules [293]. Plasmonic nanoparticles and nanostructures are particularly well suited to develop these nanosensors. Their ultra-small modal detection volumes translate into very high detection sensitivities. In 2012, single protein molecule detection in aqueous solution was demonstrated with plasmonic nanorods as small as approximately 37 × 9 nm in the studies by Ament et al. and Zijlstra et al. [320, 321]. In both demonstrations, individual protein binding events were

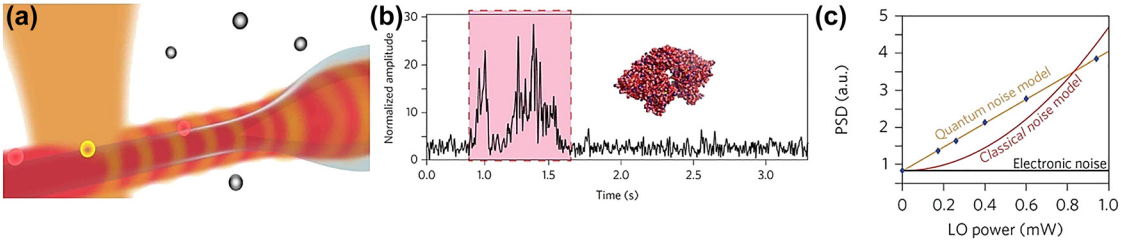

Figure 15: Tapered fibre single molecule detection platform.
(a) Sensor geometry; dark-field pump beam (orange) is scattered by nanoparticles into the tapered fibre. Local oscillator (red) propagating in the fibre modulates the scattered signal and is measured by a balanced detector. (b) Detection signal for a single BSA (bovine serum albumin) molecule. (c) Power spectral density of system noise is shown to scale linearly with local oscillator power, consistent with quantum-limited noise. Reprinted by permission from Springer Nature: Nature Photonics [155], copyright (2017).

recorded from the shifts of the plasmon resonance spectra. In the most sensitive demonstration that was aided by a photothermal effect [321], the best sensitivity at the shot noise limit was estimated at ~53 kDa, approximately the molecular weight of streptavidin protein. Many important protein markers for disease have a molecular weight larger than 50 kDa, examples for this are antibodies. With arrays of plasmonic gold nanorods having already demonstrated clinically relevant bulk detection tasks [322], the emerging localized surface plasmon resonance (LSPR) single-molecule sensors are poised to play a very important role in future healthcare applications. Moving beyond the current ~53 kDa detection limit of LSPR sensors, however, requires new approaches to advance on the uphill road of improving the single-molecule detection of plasmonic nanosensors. One of the very promising and very recent approaches in this regard is based on the use of optical microcavities to read out the response of plasmonic nanosensors, a class of hybrid photonic-plasmonic sensors called optoplasmonic sensors [146].

In order to understand the exceptionally high single-molecule sensitivity of optoplasmonic sensors, it is instructive to first review the sensing mechanisms that have been established for optical microcavities based on WGMs [29, 323]. The electric-field operator of a quantized WGM at frequency ω_L takes the general form,

$$\mathbf{E}(\mathbf{r},t) = \mathbf{u}(\mathbf{r})ae^{-i\omega_L t} + \mathbf{u}^*(\mathbf{r})a^\dagger e^{i\omega_L t}$$

with the normalized mode vector $\mathbf{u}(\mathbf{r})$ and the annihilation a and creation $a^\dagger$ operators of intracavity photons. When a tiny particle (e.g. metal nanoparticle and molecules) is located in the vicinity of the microcavity, the evanescent light of a WGM perturbs the distribution of electrons in the particle, which in turn affects the spectral profile of the WGM. Two counter-propagating WGMs (clockwise: cw and counter-clockwise: ccw) are degenerate, i.e. corresponding to the same mode frequency ω_L. The particle interacts with cw and ccw WGMs simultaneously. In general, the particle may be modelled by a two-state (upper $|e\rangle$ and lower $|g\rangle$) system with a transition frequency ω_A. The coupling strength between the light-induced dipole moment $\mathbf{d}$ of particle and the cw (ccw) WGM is $g_{cw} = -\mathbf{d}\cdot\mathbf{u}_{cw}(\mathbf{r}_0)/\hbar$ ($g_{ccw} = -\mathbf{d}\cdot\mathbf{u}_{ccw}(\mathbf{r}_0)/\hbar$) with the particle's location $\mathbf{r}_0$. Besides the particle-WGM coupling, the particle also interacts with the (vacuum) bosonic reservoir, which accounts for the backscattering and Rayleigh scattering of WGM photons. The jth boson mode is characterized by the annihilation b_j and creation $b_j^\dagger$ operators with the corresponding frequency ω_j. The coupling strength between the particle and the jth boson mode is $g_j = \sqrt{\frac{\omega_j}{2\hbar\epsilon_0 V_{\rm vac}}}|\mathbf{d}|$ with the quantization volume $V_{\rm vac}$. As a result, the Hamiltonian for some such interacting system is written as

$$H/\hbar = \omega_L a_{ccw}^\dagger a_{ccw} + \omega_L a_{cw}^\dagger a_{cw} + \frac{\omega_A}{2}\sigma_z + \sum_j \omega_j b_j^\dagger b_j - \left(g_{ccw}\,\sigma_{eg}a_{ccw} + g_{cw}\sigma_{eg}a_{cw} + \sigma_{eg}\sum_j g_j b_j + h.c. \right),$$

with the particle's operators $\sigma_{eg} = |e\rangle\langle g|$, $\sigma_{ge} = \sigma_{eg}^\dagger = |g\rangle\langle e|$ and $\sigma_z = |e\rangle\langle e| - |g\rangle\langle g|$. According to the Heisenberg equation of motion for an operator, $dO/dt = i[H/\hbar, O]$, one obtains the following equations

$$da_{cw}/dt = (-\kappa/2 - i\omega_L)a_{cw} + ig_{cw}^*\sigma_{ge},$$

$$da_{ccw}/dt = (-\kappa/2 - i\omega_L)a_{ccw} + ig_{ccw}^*\sigma_{ge},$$

$$d\sigma_{ge}/dt = (-\gamma/2 - i\omega_A)\sigma_{ge} - ig_{ccw}a_{ccw}\sigma_z - ig_{cw}a_{cw}\sigma_z - i\sigma_z\sum_j g_j b_j,$$

$$db_j/dt = -i\omega_j b_j + i\sigma_{ge}g_j^*,$$

where we have artificially inserted the dissipative terms associated with the cavity losses (rate κ) and the decay of particle's polarization (rate γ). In the weak-coupling limit, the particle stays mainly in the lower state $|g\rangle$, thereby $\sigma_z \sim -1$. Following the Weisskopf-Wigner approach, the equations of motion for the cavity operators can be approximately derived as

$$da_{cw}/dt = (-\kappa/2 - \Gamma_R/2 + i\Delta)a_{cw} + (-\Gamma_R/2 + i\Delta)e^{i\varphi}a_{ccw},$$

$$da_{ccw}/dt = (-\kappa/2 - \Gamma_R/2 + i\Delta)a_{ccw} + (-\Gamma_R/2 + i\Delta)e^{-i\varphi}a_{cw}.$$

Here we have defined the particle's polarizability $\alpha = \frac{|\mathbf{d}|^2}{\hbar(\omega_A - \omega_L - i\gamma/2)}$, the Rayleigh scattering rate $\Gamma_R = \left(\frac{\alpha}{\epsilon_0}\right)^2 \frac{\omega_L^4}{6\pi(c/n)^3 V_{\rm cav}}$, and the mode frequency shift $\Delta = \left(\frac{\alpha}{\epsilon_0}\right)\frac{\omega_L}{2V_{\rm cav}}$. The WGM volume $V_{\rm cav}$ is defined based on the light intensity at the location $\mathbf{r}_0$ of particle and φ denotes the phase difference between cw and ccw waves at $\mathbf{r}_0$. The above coupled equations may be extended to a system with multiple particles,

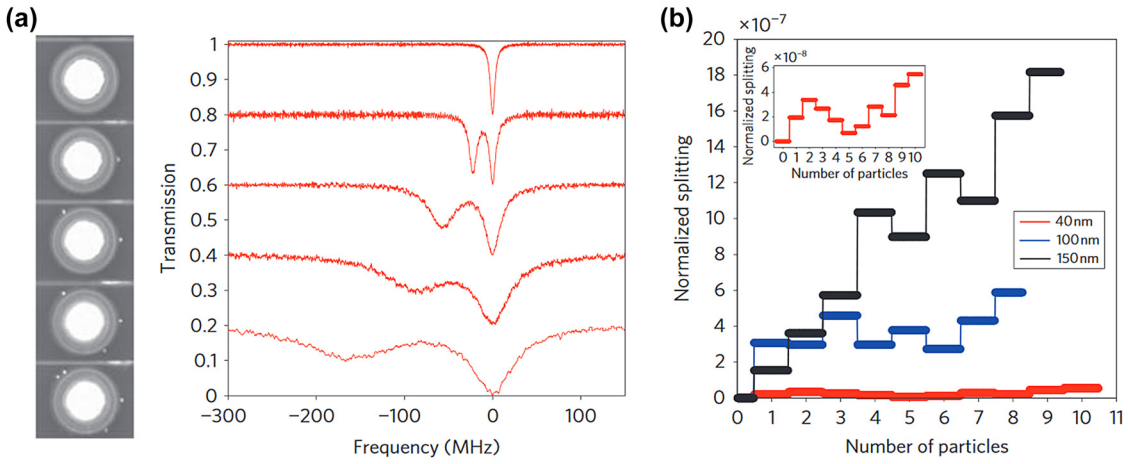

Figure 16: (a) Series of transmission spectra recorded with successive depositions of nanoparticles. (b) Splitting distance versus the number of nanoparticles bound to the microcavity's surface. Reprinted by permission from Springer Nature: Nature Photonics [323], copyright (2009).

$$\frac{d}{dt}\begin{pmatrix} a_{cw} \\ a_{ccw} \end{pmatrix} = \left[-\frac{\kappa + \kappa_{in}}{2} + i(\omega - \omega_L) + \sum_k \left(-\frac{1}{2}\Gamma_{R,k} + i\Delta_k \right) \times \begin{pmatrix} 1 & e^{i\varphi_k} \\ e^{-i\varphi_k} & 1 \end{pmatrix} \right] \begin{pmatrix} a_{cw} \\ a_{ccw} \end{pmatrix} - \sqrt{\kappa_{in}} \begin{pmatrix} a_{cw}^{in} \\ a_{ccw}^{in} \end{pmatrix},$$

with the fibre taper-cavity coupling strength κ_{in} and the amplitudes a_{cw}^{in} and a_{ccw}^{in} of the input cw and ccw fields, respectively.

As one can see, the cw and ccw WGMs are coupled with each other through the backscattering and Rayleigh scattering. This, as a result, gives rise to the spectral splitting and broadening in the passive measurement of transmission spectra, as shown in Figure 16. It is worth noting that the splitting distance between two spectral peaks may either increase or decrease as a new particle is bound to the microcavity's surface because of the phase differences φ_k (Figure 16b).

Optical dielectric microcavities such as tiny ~100 um glass microspheres confine light for an extended time period by the near-total internal reflection of light. The resulting WGM optical resonances exhibit very narrow linewidths and high quality factors up to 10^9 in air [324]. The dielectric WGM sensors are immersed in liquid sample solution to detect protein molecules as they bind to the surface of the glass microsphere [325, 326]. For example, the binding of BSA protein to the WGM sensor shifts the frequency (wavelength) of the WGM [326] continuously as a protein layer is formed. The WGM frequency shifts are caused by the energy required to polarize the nanosized protein molecules in the layer, with the evanescent field of the WGM. By first-order perturbation, the molecules need only to be characterized by their polarizability α_{ex} in excess of that of the surrounding medium, which in biosensing is water:

$$\frac{\Delta\omega}{\omega} \cong \frac{-(\alpha_{ex}/\epsilon_0)|\mathbf{E}_0(\mathbf{r}_p)|^2}{2\int \epsilon_r(\mathbf{r})|\mathbf{E}_0(\mathbf{r})|^2 dV},$$

where $\Delta\omega$ is the WGM frequency shift, ω is the unperturbed WGM resonance frequency before the protein is adsorbed, α_{ex} is the excess polarizability of the protein molecule with respect to the solvent, ε_r denotes the refractive index distribution, $\mathbf{E}_0(\boldsymbol{r})$ is the electric field of the WGM, and $\boldsymbol{r}_p$ is the molecule's position. The above equation is often referred to as the reactive sensing principle (RSP). It allows us to estimate the frequency shifts induced by a variety of biomolecules in different biosensing applications of dielectric WGM sensors [327]. A careful analysis of the WGM detection limits [328] reveals that one has to maximize a figure of merit that is proportional to Q/V in order to achieve a high nanoparticle per-molecule detection sensitivity, where V is the mode volume of the probing WGM.

The equation shown above can be applied to the optoplasmonic sensor, a WGM-plasmonic nanoparticle system, under the assumption that the plasmonic nanoparticle only act to locally enhance the electric field interacting with the molecules. With this in mind one rewrites this RSP equation as

$$\frac{\Delta\omega}{\omega} \cong \frac{-\alpha_{ex} f^2(\boldsymbol{r}_p)}{2V_m},$$

where $f^2(\boldsymbol{r}_p) = |\mathbf{E}_0(\boldsymbol{r}_p)|^2/\max[\varepsilon(\mathbf{r})|\mathbf{E}_0(\mathbf{r})|^2]$ is the normalised mode distribution and $V_m = \int_V \varepsilon(\mathbf{r})|\mathbf{E}_0(\mathbf{r})|^2 d\mathbf{r}/\max[\varepsilon(\mathbf{r})|\mathbf{E}_0(\mathbf{r})|^2]$ is the mode volume [329]. The enhancement factor $f^2{}_{\text{enh}}(\boldsymbol{r}_p) = f^2(\boldsymbol{r}_p)_{\text{WGM optoplasmonic}}/f^2(\boldsymbol{r}_p)_{\text{WGM dielectric}}$ signifies the boost of the single-molecule detection signal that is

obtained on the hybrid optoplasmonic WGM sensor as compared to the dielectric WGM counterpart without plasmonic nanoparticle, if the Q factor and V_m do not significantly change when forming the WGM-plasmonic nanoparticle system which is most often the case in biosensing [329].

Optoplasmonic WGM sensors can be most easily realized by attaching one or more plasmonic nanoparticles to a WGM glass microsphere cavity [330–332]. For the optoplasmonic sensing of single DNA molecules, a gold nanoparticle of ~20–100 nm in size is attached to ~80 μm diameter WGM microsphere [332]. The self-assembled optoplasmonic sensors enable the detection of single DNA oligomers (11-mers) and intercalating dye molecules <1 kDa in molecular weight [332], demonstrating an optoplasmonic sensor sensitivity that is much improved over the ~53 kDa detection limit reported for the LSPR nanosenors [321]. On ultra-sensitive optoplasmonic WGM sensors, single-molecules are detected from the shifts of the resonance frequencies of hybrid photonic-plasmonic WGMs. The shifts appear when molecules bind to the metal nanoparticle, where they perturb the sensor system. In the most sensitive single-molecule sensing demonstrations [147, 333], the WGM remains weakly coupled [334, 335] to the plasmon resonance of the attached plasmonic nanoparticle, a gold nanorod. In these demonstrations, the plasmonic nanoparticle, the gold nanorod, provides a dramatic near field enhancement at the single-molecule detection site. The gold nanorods employed in these demonstrations are excited near plasmon resonance with WGM and provide high near field enhancements due to their rod-shaped nanostructures and their high aspect ratio. Experimentally, it was found that single molecules such as BSA (~66.5 kDa) shift the hybrid-photonic plasmonic WGM by several tens of MHz when the protein molecules bind to the most sensitive detection sites encountered most likely at the tips of the nanorod. The enhancement of the detection signal there is on the order of $f^2_{\mathrm{enh}} \sim 10^{3-4}$. For the dielectric WGM microcavity counterpart, the RSP predicts only ~ kHz of WGM frequency shifts [325]. Given the small single-molecule polarizabilities of proteins such as BSA (~66.5 kDa) [336] and even much smaller polarizabilities of aminoacids as such as cysteine (~121 Da) and small molecules such as cysteamine (~77 Da), all of which have been detected on optoplasmonic WGM sensors [29], the detection signal on the dielectric WGM sensor would be well below the noise floor.

One can conceptually explain the enhancement factor of 10^3–10^4 improvement of optoplasmonic WGM detection limits over those of dielectric WGM microsphere sensors with the plasmonic near-field enhancements provided by the plasmonic nanostructures which are nanorods in all of the highly sensitive demonstrations well below the ~53 kDa LSPR detection limit. The nanorod-based plasmonic near-field enhancements benefit from the surface roughness of gold nanorods [332] and may result in the factor 10^{3-4} of optoplasmonic single-molecule sensitivity enhancements that have been observed. The relative improvements in the sensitivity of optoplasmonic sensors may be approximated by a figure of merit that is proportional to $Q/V \times E^2/E_0^2$. The term E^2/E_0^2 denotes the maximum near field enhancement that single molecules can explore within a detection site at or near the surface of a plasmonic nanostructure coupled to the WGM microcavity. Note that the Q factor and the mode volume after attaching gold nanorods to the WGM resonator do not change significantly in actual biosensing experiments in water. Dielectric WGM sensors immersed in water for biosensing applications start out with a Q factor on the order of 1×10^7. Their polar mode numbers l [337] are typically in the range of l = 300 to l = 1000 for the WGMs excited in glass microsphere as small as 80 ům and at visible to near infrared wavelengths 640 –780 nm. The Q factor drops to approximately 2–3×10^6 after the cavity is modified with one or a few gold nanorods [147, 292, 332, 333].

The plasmonic near field of optoplasmonic sensors defines a detection length scale which can be on the order of the diameter of a protein such as BSA with a diameter of about ~3–4 nm. Any changes in the chemical structure or physical shape (conformation) of a protein such as an enzyme that remains immobilized within the nanometer-scale plasmonic sensing hotspot can be observed in real-time [281, 294]. Optoplasmonic sensors are thus sensitive to structural changes in protein because the detection signal, the resonance frequency or wavelength shift, changes as the overlap of the protein with the highly localized near field changes. Likewise, any chemical changes in the composition of the immobilized protein or the binding of a substrate to an enzyme or a ligand to a receptor would all contribute to the shifts. The variations of the wavelength shift signal $\Delta\lambda$ caused by e.g. conformational (shape) changes of a protein can be estimated from:

$$\Delta\lambda \propto \alpha_{ex}\left(\int\limits_{v_m(t_2)} |E(r)|^2 dV - \int\limits_{v_m(t_1)} |E(r)|^2 dV \right).$$

The magnitude and sign of these $\Delta\lambda$ wavelength shifts are proportional to the changes in the electric field intensity integrated over the volume occupied by the molecule $v_m(t)$ at the times t_1 and t_2, where α_{ex} is the excess polarizability

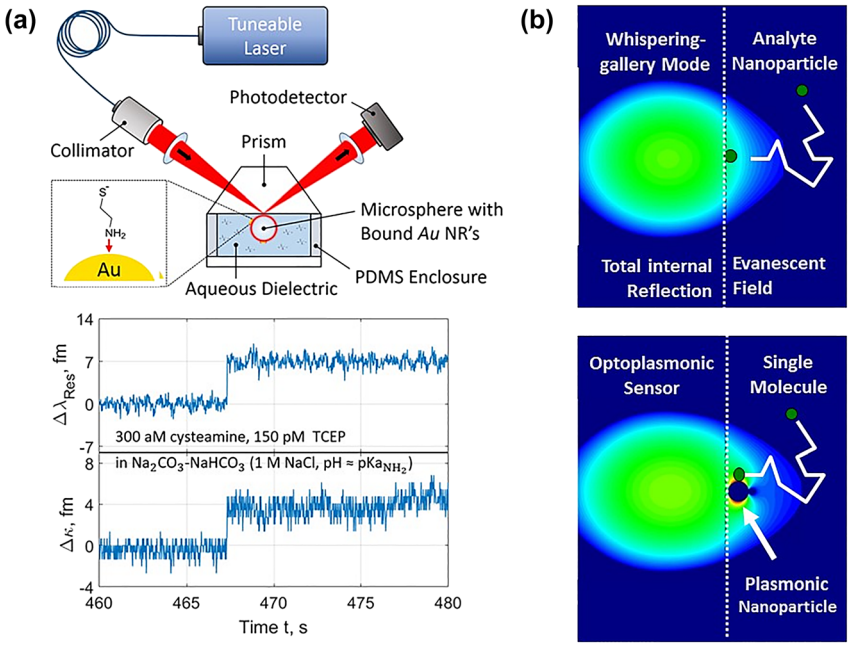

Figure 17: (a) TOP: An optoplasmonic sensor combines the light recirculation in a high Q (Q~10^{6-7}) whispering-gallery mode (WGM) microsphere cavity with the plasmonic near field enhancements of gold (Au) nanorods (NRs) that are attached to the microcavity. BOTTOM: Optoplasmonic sensor signals that were recorded for individual cysteamine (~77 Da) molecules binding to the Au NRs. Binding events are detected from femto-meter step-changes in the resonance wavelength or linewidth traces. The detection sensitivity of 300 aM cysteamine required specific buffer conditions, adapted from [147]. (b) TOP: Dielectric WGM cavity sensing mechanism. The WGM resonance changes as single (analyte) nanoparticles diffuse and bind to the dielectric WGM sensor within its evanescent field where the WGM interacts with the nanoparticle, adapted from [330]. BOTTOM: Optoplasmonic WGM sensing mechanism. A plasmonic nanoparticle attached to the WGM sensor and excited by the WGM near the plasmon resonances frequency enhances the intensity of the probing light field at the surface of the nanoparticle. Single molecules are detected with much higher sensitivities if they bind within the region of plasmonic near-field enhancements where, depending on the plasmonic nanoparticle or system, the wavelength shift can be greatly enhanced by a factor of 10^3–10^4 over the shift expected for an all-dielectric microsphere sensor, adapted from [330].

of the protein, and v_m (t) is the volume taken up by the protein which depends on the conformation (shape) of the protein adopted at time points t_1 and t_2.

Several demonstrations for the optoplasmonic sensing beyond the ~53 kDa LSPR detection limit have been reported for optoplasmonic WGM sensors. These demonstrations including the detection of 11-mer oligonucleotides and the small, intercalating <1 kDa dye molecules [332], as well as the sensing of single atomic ions such as Zn^{2+} and Hg^{2+} ions in aqueous solution [333]; and most recently the monitoring of intricate chemical reactions such as the disuflide exchange reaction [147] and the detection of small dithiobis(C2-NTA, ~772 Da) molecules from effective WGM linewidth shifts [329].

Single cysteamine molecules have been detected at attomolar concentration levels as the ~77 Da molecules bind to the gold nanorods of a WGM optoplasmonic sensor (Figure 17). The cysteamine molecules link to gold nanorod via their amine group, at the specific buffer conditions used for their immobilization. Once bound, the thiol group of the cysteamine molecule provides a single thiol site for the reversible binding of, i.e. D- and L-cysteine aminoacids. In this way, it becomes possible to find experimental conditions that allow for the repeated probing of a thiolated molecule species such as D- or L-cysteine as these molecules repeatedly bind and unbind at a single thiol sensing site. In this way, the heterogeneity of sensing sites on the optoplasmonic WGM nanosensors can be greatly reduced or removed. This results in signal levels in the single molecule traces [147], which marks an important milestone for demonstrating the laboratories on chip that can potentially identify molecular species. It is a milestone for demonstrating the quantitative analysis of the sensing signals and thereby achieving advanced single-molecule sensing capabilities such as chiral discrimination i.e. of the D and L aminoacids.

With further technical improvements, it is expected that the optoplasmonic sensors will be able to demonstrate

single-molecule sensing capabilities by operating with single photons and at the detection limit set by the quantum noise. The development of the faint-light metrology for single-molecule WGM biosensors operating at the quantum limits will help us implement the most noninvasive optical single-molecule probing techniques. Once single molecules can be probed with single photons it is envisaged that the single photons can be analysed for additional phase or polarization information. The analysis of single photons that have interacted with single molecules may provide us with the possibility for measuring the properties of the molecules that could not have been measured with classical techniques. For example, it is envisaged to realize time averaged single photon-single protein short time scale interactions which could be further improved with ultrafast pulses and they can probe the quantum properties outlined in the first section of this review.

Advancing the sensing capabilities of optical micro and nanosensors even further, beyond the classical limits of detection and beyond the photon shot noise, will require entirely new approaches. Quantum metrology applied to optoplasmonic sensors provides a new avenue to take for advancing single molecule detection capabilities and improving the sensitivity. Moving beyond the classical detection limits, will require the application of quantum-correlated non-classical light sources and quantum measurement schemes described in Sections 4 and 5. Bowen et al. have already demonstrated detection of approx. 50 kDa bovine serum albumin proteins with evanescent optical fibre sensors operating at the photon shot noise (quantum noise) limit [155]. It is envisaged that the optoplasmonic WGM sensors can operate beyond the standard quantum limit (SQL) with the applications of N00N states and squeezed light states. Moving existing biosensing techniques to the quantum-enhanced regime comes with a considerable increase in complexity; for example the need for single photon detectors, single photon timing and counting modules, stringent limits on optical losses, and quantum optical light sources such as non-linear crystal setups. However, the complexity could be significantly reduced with the integration of components on-chip. As demonstrated in Section 6, quantum optical light sources and even entire sensors have the potential to be integrated on-chip, and could therefore become more accessible through collaborations with experts in integrated quantum information technologies and fabrication. Quantum optical laboratories on a chip will enable us to use quantum biosensors such as optoplasmonic WGM sensors to explore Nature's smallest entities such as single molecules, single photons, pico-Newton forces, molecular chirality, and their interesting physics and applications at unprecedented quantum levels of detection whilst not interfering with the biomolecular activity.

7.5 Quantum optical imaging

Before we close our discussion on the prospects and progress of new generation sensors with unprecedented detection limits driven by quantum phenomena, it will be worthwhile to give a short glimpse of the advances in quantum optical imaging. Ghost imaging was the first experimentally demonstrated imaging technique exploiting quantum correlations between photons [338]. This technique uses entangled photon pairs from a spontaneous parametric down-conversion (SPDC) source. One of each photon pair passes through the object to a bucket detector and the other passes directly to a spatially-resolving detector. Momentum correlations between paired photons allow an image to be formed from coincident signals at the two detectors. Ghost imaging has since been shown to be possible using intensity correlations in purely classical coherent [339]—and even thermal [340, 341]—light sources. Despite this, quantum correlations offer improvements in resolution over classical schemes and the possibility of sub-shot noise sensitivity [342]; see Meda et al. for a review of this area [343].

Imaging schemes relying on quantum correlations include quantum illumination [345–347], sub-shot noise imaging [19, 20], interaction-free imaging [348] and quantum correlated plenoptic imaging [349, 350]. Rather than working to improve resolution, these techniques typically aim to increase imaging *sensitivity*, achieving greater image contrast against background thermal noise than is possible using classical imaging. Improved sensitivity allows the imaging of weakly absorbing objects at low light intensities; a regime ideally suited to biological samples prone to photo-damage. As a demonstration of this, Morris et al. [344] reported imaging a wasp wing in a heralded single photon imaging experiment with an average of only 0.45 photons per pixel (Figure 18).

A recent development in quantum illumination was the first full-field imaging setup. This achieved up to a factor of 5.5 improvement in image contrast over a setup using illumination with classical light in the presence of thermal background noise [351]. Wide-field microscopy has also been demonstrated with sub-shot noise sensitivity; 80% of the shot-noise level per pixel [20]. By applying median filtering, noise could be reduced further to <30% of the shot-noise level. Imaging can even be performed by measuring photons which have not interacted with the object directly, by using

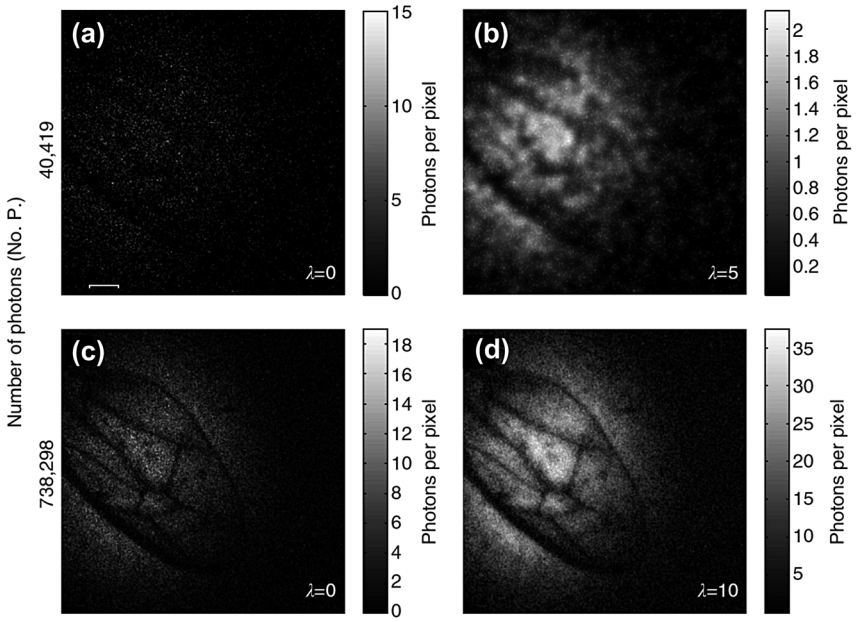

Figure 18: Heralded single-photon imaging of a wasp wing.
a and c direct imaging b and d reconstructed image using correlations in photon pair detection. Scale bar in a measures 400 µm. Adapted from the study by Morris et al. [344], available under creative commons license 4.0.

two photon pair sources and detecting photons entangled with those passing through the sample [348]. This could allow detectors to operate in a different frequency band to that incident on the sample, working in a band where the available detector efficiency is higher for example.

Quantum-enhancements to image *resolution* have also been proposed, for example using entangled two-photon fluorescence microscopy [352]. Typically, high light intensities are required to efficiently detect non-linear fluorescence processes, but by instead exploiting correlations between entangled photon pairs, much lower light intensities could be used. Two-photon fluorescence has been demonstrated using entangled photons illuminating organic fluorophores, including porphyrin dendrimers [162] and annulene systems [353]. A two-photon microscope using entangled photons has also been produced which achieved a signal-to-noise ratio 1.35 times greater than possible at the shot-noise limit [354]. An experiment combining these to produce an entangled two-photon *fluorescence* microscope could not be found.

Sub-diffraction imaging can also be achieved using the single photon properties of fluorescence from individual NV centres [356, 357] and CdSe/CdS/ZnS colloidal quantum dots [358]. In these reports, nearby single photon emitters are resolved below the diffraction limit by measuring higher-order intensity correlations in the light emitted by fluorescence. Rather than illuminating a sample with entangled photons, this approach performs imaging by measuring the photon statistics of light emitted from the sample itself. The most advanced imaging experiment

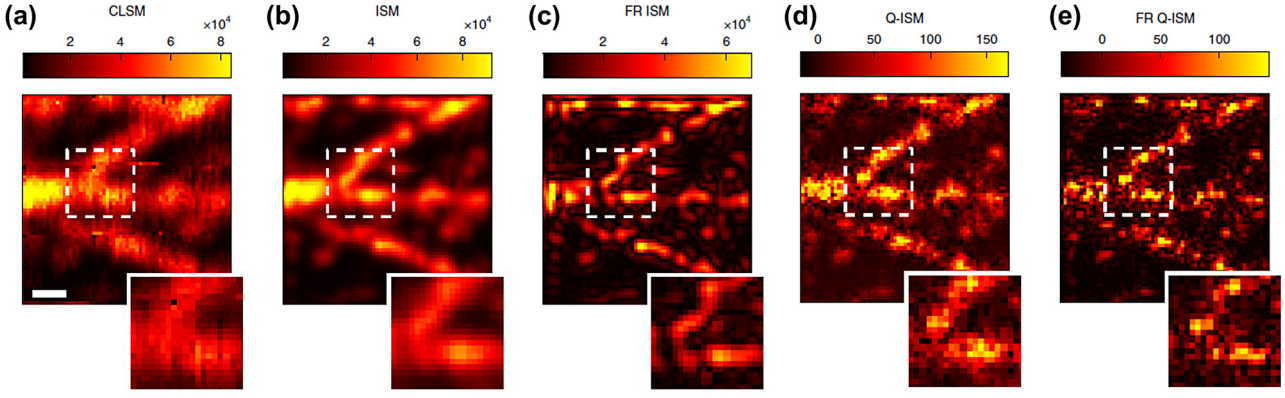

Figure 19: Microtubule imaging using quantum ISM.
Image scanning microscopy (ISM) images of a microtubule sample labelled with fluorescent quantum dots. Different imaging techniques using the same experimental setup are compared, from classical scanning microscopy (CLSM, a) to Fourier reweighted quantum image scanning microscopy (FR Q-ISM, d). Scale bar: 0.5 µm. Reprinted by permission from Springer Nature: Nature Photonics [355], copyright (2018).

working on this principle was recently reported by Tenne, Rossman, Rephael et al. [355]. This experiment combined the classical image scanning microscopy (ISM) method with correlation measurements between high time resolution single photon detectors, to image single photon fluorescence emission from CdSe/CdS/ZnS quantum dots. Features in microtubule cell samples containing these nanoparticles were imaged with a resolution four times the diffraction limit, as shown in Figure 19.

8 Outlook and future directions

Impressive progress has been made so far in the area of quantum-enhanced biosensing. A broad range of measurements have been made using quantum optical probe states, from concentration measurements [133] to particle tracking [151], and many of these experiments have achieved higher sensitivities than would be possible with a classical probe. Similar quantum optical enhancements have yet to be demonstrated in the field of label-free single-molecule biosensing, although the development of quantum noise limited nanofiber sensors [155] sets a challenge for the next generation of single molecule experiments to beat this limit. By maximising the sensitivity at a given optical power, we can develop non-invasive biosensors that operate below photodamage thresholds [359–361] or the excitation thresholds of interesting biological molecules such as photoreceptors. This could allow optical sensors to probe biological systems non-invasively and over longer timescales than otherwise possible. Squeezed light in particular offers greater flexibility over the optical power available compared to typical entangled photon sources [362], allowing quantum-enhanced biosensing experiments to compete with the sensitivity of corresponding classical experiments. This has made possible quantum-enhanced plasmonic sensing of refractive index changes at state-of-the-art sensitivity $10^{-10}\mathrm{RIU}/\sqrt{\mathrm{Hz}}$ [156]. More efficient generation and detection efficiency of squeezed states can improve sensitivities even further. Using the full potential of current 10–15 dB squeezing capabilities is predicted to be able to improve the sensitivity of optomechanical magnetometers by a factor of 5.6 [157], and the resolution of photonic force microscopy by an order of magnitude [152].

In the future, integrated biosensors could mitigate some of the practical challenges that face the incorporation of quantum optical probes into sensors for biological systems. Optical losses between the photon source and detector could be reduced by integrating as many components as possible on-chip, with efficient waveguide couplers between them, and grating couplers to interface with external components. Experiments in quantum metrology have shown that high optical efficiency is key to achieving truly sub-shot noise measurement schemes [34]. On-chip quantum optical components, from entangled photon pair and single photon sources to single photon detectors, have already been developed, primarily for quantum information applications. These components could also be used to implement quantum metrology schemes in on-chip quantum optical biosensors. Microfluidic systems would be well suited to delivering biological samples to an on-chip quantum optical biosensor, and they have already been applied in quantum-enhanced biosensing [133]. Particularly promising in this context is the integration of sources of photon quantum states based on non-linear optics with electronic on-chip complementary metal oxide semiconductor (CMOS) technology, to controllably provide photons on demand for the biological quantum-measurements [119]. The integration of CMOS compatible heralded photon sources and quantum optical frequency combs with single-molecule biosensors opens up fundamentally new opportunities for faint-light metrology and real time tracking of single biomolecular interactions and dynamics [240, 363]. Another goal to aim for will be the integration of super resolution imaging microscopy [355] together with quantum-enhanced plasmonic and optoplasmonic sensors for faint-light metrology [146]. Placing these various technologies on chip can promote their wide spread use in applications that analyse biomatter with quantum-optical measurement techniques whilst validating measurements with single-molecule microscopy techniques [364].

An exciting prospect for integrating solid state spin-based quantum sensing on optical biosensor chips is the possibility to control individual nuclei with electric fields as opposed to magnetic fields. Electric fields are more easily confined and screened at the nanoscale than magnetic fields, which allows them to target individual nuclear spins. Using highly localized fields reduces the spin-noise due to excited neighbouring nuclei and improves the signal-to-noise ratio in the readout. In experiments, quantum control using localized electric fields was realized for the first time with a single 123Sb (spin-7/2) nucleus and provides the foundations for applications in nuclear electric resonance spectroscopy [365]. The detection of single nuclear spins can have wide ranging applications in structural analysis ranging from life sciences to materials research [366, 367].

Quantum optical bioscience (QOB) laboratories on chip may also address one of the challenging and

fascinating questions, namely what role do quantum effects play in human cognition, a highly debated field of research with diverse and contrary opinions. Is our brain a quantum brain? Are quantum effects measurable in the brain, are they essential for thought, memory and intelligence? Has Nature exploited quantum-biological effects for the evolution of the human mind? Neuroscientists have thus far studied the brain without looking for quantum effects and have not been able to explain the human mind. The study of biophotons in the brain could now be extended into the quantum-realm [368, 369]. QOB laboratories may aid the investigation of quantum effects in the brain, with the study of biological neuroscience in animal model systems of reduced complexity and size thereby facilitating the quantum-optical analysis by on-chip integration. A possible quantum nature of cells and organs in the model organism could be probed with classical and quantum states of light applied directly to its photosensitive constituents while simultaneously (fluorescence) imaging a physiological response.

QOB is one of the emerging fields in optics and photonics to study molecules and biological matter. An innovative approach to detect and measure a single molecule could use WGM microcavities, to develop unique probing methods to study a molecule at nanometer scale, and to apply these precision measurement techniques to study biomolecules and bioemitters, and enhance the sensor by using highly sensitive optical interferometer and quantum measurement techniques to overcome noise limits. The enhanced sensors could enable a magnificent way to analyse photons emitted from a single molecule in real time at nanoscale realizing the possibility of *nanoprobing*. One could take advantage of the cavity Purcell factor with a suitable fluorescent probe and establish a new technique to study molecules as they respond to a change such as ligand binding. Combined with the single photon correlation analysis, the nanoprobing on the optoplasmonic WGM sensor platform could become a new tool to study protein folding, conformation changes, chemical reactions and chirality. Once we gain a better understanding of quantum effects in nature, will it be possible to harness these effects in devices? Can we create new quantum technologies inspired by nature? Already, genetically engineered green fluorescent proteins (GFPs) have been used to produce quantum-entangled photons [370]. In the near future, will we use *in vitro* evolution experiments to evolve such biological systems with desired quantum effects? Biologically inspired quantum technologies may well outperform classical devices designed for the same purpose. Quantum thermodynamics already points the way towards engineering better nanoscale heat engines [371]. Indeed, if evolution has been making use of quantum effects then we should be able to uncover more biological quantum systems. There may be a wealth of yet to be discovered quantum processes in nature in addition to the ones reviewed here, namely magneto-perception, olfaction, photosynthesis and enzymatic activity. Nature itself may well offer inspiration for exciting new approaches to build quantum networks and quantum sensors with the help of molecules.

QOB laboratories on chip will play a major role in uncovering all of these new quantum processes in Nature that were difficult to study with traditional biophysical and quantum optical measurement techniques. Single photons can probe single molecules on very short timescales where they may reveal quantum properties discussed in chapter one of this review. The challenges are set, now we will need to develop the methods that are capable of the quantum state characterisation of biophotons emitted by biomatter; and we need to develop the methods capable of the quantum state characterisation of photons that have interacted with single-molecules.

Author contributions: All the authors have accepted responsibility for the entire content of this submitted manuscript and approved submission.
Research funding: This research was funded by (i) EPSRC – EP/T002875/1 Molecular Mechanics of Enzymes, (ii) EP/R031428/1—An Optical Single Molecule Scanner of Protein Motion and the Royal Society—Wolfson Research Merit Award.
Conflict of interest statement: The authors declare no conflicts of interest regarding this article.

References

[1] M. A. Taylor and W. P. Bowen, "Quantum metrology and its application in biology," *Phys. Rep.*, vol. 615, pp. 1–59, 2016.
[2] N. Lambert, Y.-N. Chen, Y.-C. Cheng, C.-M. Li, G.-Y. Chen, and F. Nori, "Quantum biology," *Nat. Phys.*, vol. 9, pp. 10–18, 2012.
[3] G. R. Fleming, G. D. Scholes, and Y.-C. Cheng, "Quantum effects in biology," *Proc. Chem.*, vol. 3, pp. 38–57, 2011.
[4] J. Cai, "Quantum biology: explore quantum dynamics in biological systems," *Sci. China Inf. Sci.*, vol. 59, 2016, https://doi.org/10.1007/s11432-016-5592-y.
[5] J. C. Brookes, "Quantum effects in biology: golden rule in enzymes, olfaction, photosynthesis and magnetodetection," *Proc. Math. Phys. Eng. Sci.*, vol. 473, p. 20160822, 2017.
[6] R. Penrose and R. Landauer, "The emperor's new mind: concerning computers, minds, and the laws of physics," *Phys. Today*, vol. 43, pp. 73–75, 1990.
[7] J. Reingruber, D. Holcman, and G. L. Fain, "How rods respond to single photons: key adaptations of a G-protein cascade that

enable vision at the physical limit of perception," *Bioessays*, vol. 37, pp. 1243–1252, 2015.
[8] A. Marais, B. Adams, A. K. Ringsmuth, et al., "The future of quantum biology," *J. R. Soc. Interface*, vol. 15, 2018, https://doi.org/10.1098/rsif.2018.0640.
[9] K. M. Doll, B. R. Bender, and R. G. Finke, "The first experimental test of the hypothesis that enzymes have evolved to enhance hydrogen tunneling," *J. Am. Chem. Soc.*, vol. 125, pp. 10877–10884, 2003.
[10] C. Offord, "Quantum biology may help solve some of life's greatest mysteries," *The Scientist*, 2019. Available at: https://www.the-scientist.com/features/quantum-biology-may-help-solve-some-of-lifes-greatest-mysteries-65873.
[11] T. Ritz, P. Thalau, J. B. Phillips, R. Wiltschko, and W. Wiltschko, "Resonance effects indicate a radical-pair mechanism for avian magnetic compass," *Nature*, vol. 429, pp. 177–180, 2004.
[12] A. Pinzon-Rodriguez, S. Bensch, and R. Muheim, "Expression patterns of cryptochrome genes in avian retina suggest involvement of Cry4 in light-dependent magnetoreception," *J. R. Soc. Interface*, vol. 15, 2018, https://doi.org/10.1098/rsif.2018.0058.
[13] E. M. Gauger, E. Rieper, J. J. Morton, S. C. Benjamin, and V. Vedral, "Sustained quantum coherence and entanglement in the avian compass," *Phys. Rev. Lett.*, vol. 106, p. 040503, 2011.
[14] J. Cai, G. G. Guerreschi, and H. J. Briegel, "Quantum control and entanglement in a chemical compass," *Phys. Rev. Lett.*, vol. 104, p. 220502, 2010.
[15] G. S. Engel, T. R. Calhoun, E. L. Read, et al., "Evidence for wavelike energy transfer through quantum coherence in photosynthetic systems," *Nature*, vol. 446, pp. 782–786, 2007.
[16] G. Panitchayangkoon, D. Hayes, K. A. Fransted, et al., "Long-lived quantum coherence in photosynthetic complexes at physiological temperature," *Proc. Natl. Acad. Sci. U. S. A.*, vol. 107, pp. 12766–12770, 2010.
[17] S. Wills, *Quantum Effects in Biology*, Optics and Photonics News, 2019, p. 30. Available at: https://www.osa-opn.org/home/articles/volume_30/april_2019/features/quantum_effects_in_biology/.
[18] E. Schrödinger, *What is Life? the Physical Aspect of the Living Cell*, Cambridge, Cambridge University Press, 1944.
[19] G. Brida, M. Genovese, and I. Ruo Berchera, "Experimental realization of sub-shot-noise quantum imaging," *Nat. Photonics*, vol. 4, pp. 227–230, 2010.
[20] N. Samantaray, I. Ruo-Berchera, A. Meda, and M. Genovese, "Realization of the first sub-shot-noise wide field microscope," *Light Sci. Appl.*, vol. 6, p. e17005, 2017.
[21] J. Haas, M. Schwartz, U. Rengstl, M. Jetter, P. Michler, and B. Mizaikoff, "Chem/bio sensing with non-classical light and integrated photonics," *Analyst*, vol. 143, pp. 593–605, 2018.
[22] J. Aasi, J. Abadie, B. P. Abbott, et al., "Enhanced sensitivity of the LIGO gravitational wave detector by using squeezed states of light," *Nat. Photonics*, vol. 7, pp. 613–619, 2013.
[23] E. Oelker, L. Barsotti, S. Dwyer, D. Sigg, and N. Mavalvala, "Squeezed light for advanced gravitational wave detectors and beyond," *Opt. Express*, vol. 22, pp. 21106–21121, 2014.
[24] J. Wang, F. Sciarrino, A. Laing, and M. G. Thompson, "Integrated photonic quantum technologies," *Nat. Photonics*, vol. 14, pp. 273–284, 2019.
[25] A. Politi, M. J. Cryan, J. G. Rarity, S. Yu, and J. L. O'Brien, "Silica-on-silicon waveguide quantum circuits," *Science*, vol. 320, pp. 646–649, 2008.
[26] J. Wang, S. Paesani, Y. Ding, et al., "Multidimensional quantum entanglement with large-scale integrated optics," *Science*, vol. 360, pp. 285–291, 2018.
[27] D. Llewellyn, Y. Ding, I. I. Faruque, et al., "Chip-to-chip quantum teleportation and multi-photon entanglement in silicon," *Nat. Phys.*, vol. 16, pp. 148–153, 2019.
[28] C. L. Degen, F. Reinhard, and P. Cappellaro, "Quantum sensing," *Rev. Mod. Phys.*, vol. 89, 2017, https://doi.org/10.1103/revmodphys.89.035002.
[29] F. Vollmer and D. Yu, *Single-Molecule Sensing. Optical Whispering Gallery Modes for Biosensing*, Cham, Springer, 2020.
[30] H. P. Yuen and V. W. Chan, "Noise in homodyne and heterodyne detection," *Opt. Lett.*, vol. 8, pp. 177–179, 1983.
[31] G. Santarelli, P. Laurent, P. Lemonde, et al., "Quantum projection noise in an atomic fountain: A high stability cesium frequency standard," *Phys. Rev. Lett.*, vol. 82, pp. 4619–4622, 1999.
[32] P. Grangier, J. A. Levenson, and J.-P. Poizat, "Quantum non-demolition measurements in optics," *Nature*, vol. 396, pp. 537–542, 1998.
[33] S. F. Huelga, C. Macchiavello, T. Pellizzari, A. K. Ekert, M. B. Plenio, and J. I. Cirac, "Improvement of frequency standards with quantum entanglement," *Phys. Rev. Lett.*, vol. 79, pp. 3865–3868, 1997.
[34] S. Slussarenko, M. M. Weston, H. M. Chrzanowski, et al., "Unconditional violation of the shot-noise limit in photonic quantum metrology," *Nat. Photonics*, vol. 11, pp. 700–703, 2017.
[35] V. Giovannetti, S. Lloyd, and L. Maccone, "Quantum-enhanced measurements: beating the standard quantum limit," *Science*, vol. 306, pp. 1330–1336, 2004.
[36] J. J. Bollinger, W. M. Itano, D. J. Wineland, and D. J. Heinzen, "Optimal frequency measurements with maximally correlated states," *Phys. Rev. A*, vol. 54, pp. R4649–R4652, 1996.
[37] M. Zwierz, C. A. Perez-Delgado, and P. Kok, "General optimality of the Heisenberg limit for quantum metrology," *Phys. Rev. Lett.*, vol. 105, p. 180402, 2010.
[38] R. W. P. Drever, J. L. Hall, F. V. Kowalski, et al., "Laser phase and frequency stabilization using an optical resonator," *Appl. Phys. B*, vol. 31, pp. 97–105, 1983.
[39] D. G. Matei, T. Legero, S. Hafner, et al., "1.5 mum lasers with sub-10 mHz linewidth," *Phys. Rev. Lett.*, vol. 118, p. 263202, 2017.
[40] T. Kessler, C. Hagemann, C. Grebing, et al., "A sub-40-mHz-linewidth laser based on a silicon single-crystal optical cavity," *Nat. Photonics*, vol. 6, pp. 687–692, 2012.
[41] N. F. Ramsey, "A molecular beam resonance method with separated oscillating fields," *Phys. Rev.*, vol. 78, pp. 695–699, 1950.
[42] W. M. Itano, J. C. Bergquist, J. J. Bollinger, et al., "Quantum projection noise: population fluctuations in two-level systems," *Phys. Rev. A*, vol. 47, pp. 3554–3570, 1993.
[43] S. M. Brewer, J. S. Chen, A. M. Hankin, et al., "^{27}Al^{+} quantum-logic clock with a systematic uncertainty below 10^{-18}," *Phys. Rev. Lett.*, vol. 123, p. 033201, 2019.

[44] M. A. Nielsen and I. L. Chuang, *Quantum Computation and Quantum Information*, Cambridge, Cambridge University Press, 2000.
[45] S. L. Braunstein and C. M. Caves, "Statistical distance and the geometry of quantum states," *Phys. Rev. Lett.*, vol. 72, pp. 3439–3443, 1994.
[46] H. Lee, P. Kok, and J. P. Dowling, "A quantum Rosetta stone for interferometry," *J. Mod. Opt.*, vol. 49, pp. 2325–2338, 2002.
[47] O. Hosten, N. J. Engelsen, R. Krishnakumar, and M. A. Kasevich, "Measurement noise 100 times lower than the quantum-projection limit using entangled atoms," *Nature*, vol. 529, pp. 505–508, 2016.
[48] E. Knill, R. Laflamme, and G. J. Milburn, "A scheme for efficient quantum computation with linear optics," *Nature*, vol. 409, pp. 46–52, 2001.
[49] P. Kok, W. J. Munro, K. Nemoto, T. C. Ralph, J. P. Dowling, and G. J. Milburn, "Linear optical quantum computing with photonic qubits," *Rev. Mod. Phys.*, vol. 79, pp. 135–174, 2007.
[50] R. H. Hadfield, "Single-photon detectors for optical quantum information applications," *Nat. Photonics*, vol. 3, pp. 696–705, 2009.
[51] M. D. Eisaman, J. Fan, A. Migdall, and S. V. Polyakov, "Invited review article: single-photon sources and detectors," *Rev. Sci. Instrum.*, vol. 82, p. 071101, 2011.
[52] J. Bortfeldt, F. Brunbauer, C. David, et al., "Timing performance of a micro-channel-plate photomultiplier tube," *Nucl. Instrum. Methods Phys. Res. Sect. A Accel. Spectrom. Detect. Assoc. Equip.*, vol. 960, 2020.
[53] A. K. L. Dymoke-Bradshaw, J. D. Hares, J. Milnes, et al., "Development of an ultra-fast photomultiplier tube for gamma-ray Cherenkov detectors at the National Ignition Facility (PD-PMT)," *Rev. Sci. Instrum.*, vol. 89, p. 10I137, 2018.
[54] Q. Zheng, Y. Huang, D. Huang, et al., "An improved design of the readout base board of the photomultiplier tube for future PandaX dark matter experiments," *J. Instrum.*, vol. 15, pp. T12006–T12006, 2020.
[55] F. Ceccarelli, G. Acconcia, A. Gulinatti, M. Ghioni, I. Rech, and R. Osellame, "Recent Advances and Future Perspectives of Single-Photon Avalanche Diodes for Quantum Photonics Applications," *Advanced Quantum Technologies*, vol. 4, p. 2000102, 2020.
[56] C. Scarcella, G. Boso, A. Ruggeri, and A. Tosi, "InGaAs/InP single-photon detector gated at 1.3 GHz with 1.5% afterpulsing," *IEEE J. Sel. Top. Quant. Electron.*, vol. 21, pp. 17–22, 2015.
[57] M. Sanzaro, P. Gattari, F. Villa, A. Tosi, G. Croce, and F. Zappa, "Single-photon avalanche diodes in a 0.16 μm BCD technology with sharp timing response and red-enhanced sensitivity," *IEEE J. Sel. Top. Quant. Electron.*, vol. 24, pp. 1–9, 2018.
[58] E. Waks, K. Inoue, W. D. Oliver, E. Diamanti, and Y. Yamamoto, "High-efficiency photon-number detection for quantum information processing," *IEEE J. Sel. Top. Quant. Electron.*, vol. 9, pp. 1502–1511, 2003.
[59] L. You, "Superconducting nanowire single-photon detectors for quantum information," *Nanophotonics*, vol. 9, pp. 2673–2692, 2020.
[60] I. Esmaeil Zadeh, J. W. N. Los, R. B. M. Gourgues, et al., "Single-photon detectors combining high efficiency, high detection rates, and ultra-high timing resolution," *APL Photonics*, vol. 2, 2017, https://doi.org/10.1063/1.5000001.
[61] L. Schweickert, K. D. Jöns, K. D. Zeuner, et al., "On-demand generation of background-free single photons from a solid-state source," *Appl. Phys. Lett.*, vol. 112, 2018, https://doi.org/10.1063/1.5020038.
[62] G. N. Gol'tsman, O. Okunev, G. Chulkova, et al., "Picosecond superconducting single-photon optical detector," *Appl. Phys. Lett.*, vol. 79, pp. 705–707, 2001.
[63] A. Divochiy, F. Marsili, D. Bitauld, et al., "Superconducting nanowire photon-number-resolving detector at telecommunication wavelengths," *Nat. Photonics*, vol. 2, pp. 302–306, 2008.
[64] N. Zen, H. Shibata, Y. Mawatari, M. Koike, and M. Ohkubo, "Biomolecular ion detection using high-temperature superconducting MgB2 strips," *Appl. Phys. Lett.*, vol. 106, 2015, https://doi.org/10.1063/1.4913844.
[65] H. J. Kimble, "Strong interactions of single atoms and photons in cavity QED," *Phys. Scripta*, vol. T76, 1998, https://doi.org/10.1238/physica.topical.076a00127.
[66] J. McKeever, A. Boca, A. D. Boozer, J. R. Buck, and H. J. Kimble, "Experimental realization of a one-atom laser in the regime of strong coupling," *Nature*, vol. 425, pp. 268–271, 2003.
[67] E. M. Purcell, H. C. Torrey, and R. V. Pound, "Resonance absorption by nuclear magnetic moments in a solid," *Phys. Rev.*, vol. 69, pp. 37–38, 1946.
[68] E. T. Jaynes and F. W. Cummings, "Comparison of quantum and semiclassical radiation theories with application to the beam maser," *Proc. IEEE*, vol. 51, pp. 89–109, 1963.
[69] M. I. Kolobov, L. Davidovich, E. Giacobino, and C. Fabre, "Role of pumping statistics and dynamics of atomic polarization in quantum fluctuations of laser sources," *Phys. Rev. A*, vol. 47, pp. 1431–1446, 1993.
[70] Y. Akimov, M. E. Pam, and S. Sun, "Kretschmann-Raether configuration: revision of the theory of resonant interaction," *Phys. Rev. B*, vol. 96, 2017, https://doi.org/10.1103/physrevb.96.155433.
[71] K. M. Mayer and J. H. Hafner, "Localized surface plasmon resonance sensors," *Chem. Rev.*, vol. 111, pp. 3828–3857, 2011.
[72] K. A. Willets and R. P. Van Duyne, "Localized surface plasmon resonance spectroscopy and sensing," *Annu. Rev. Phys. Chem.*, vol. 58, pp. 267–297, 2007.
[73] M. S. Tame, K. R. McEnery, Ş. K. Özdemir, J. Lee, S. A. Maier, and M. S. Kim, "Quantum plasmonics," *Nat. Phys.*, vol. 9, pp. 329–340, 2013.
[74] J. Flick, M. Ruggenthaler, H. Appel, and A. Rubio, "Atoms and molecules in cavities, from weak to strong coupling in quantum-electrodynamics (QED) chemistry," *Proc. Natl. Acad. Sci. U. S. A.*, vol. 114, pp. 3026–3034, 2017.
[75] A. F. Koenderink, "On the use of Purcell factors for plasmon antennas," *Opt. Lett.*, vol. 35, pp. 4208–4210, 2010.
[76] F. Benz, C. Tserkezis, L. O. Herrmann, et al., "Nanooptics of molecular-shunted plasmonic nanojunctions," *Nano Lett.*, vol. 15, pp. 669–674, 2015.
[77] D. O. Sigle, L. Zhang, S. Ithurria, B. Dubertret, and J. J. Baumberg, "Ultrathin CdSe in plasmonic nanogaps for enhanced photocatalytic water splitting," *J. Phys. Chem. Lett.*, vol. 6, pp. 1099–1103, 2015.
[78] G. M. Akselrod, C. Argyropoulos, T. B. Hoang, et al., "Probing the mechanisms of large Purcell enhancement in plasmonic nanoantennas," *Nat. Photonics*, vol. 8, pp. 835–840, 2014.

[79] T. B. Hoang, G. M. Akselrod, and M. H. Mikkelsen, "Ultrafast room-temperature single photon emission from quantum dots coupled to plasmonic nanocavities," *Nano Lett.*, vol. 16, pp. 270–275, 2016.
[80] R. Chikkaraddy, B. de Nijs, F. Benz, et al., "Single-molecule strong coupling at room temperature in plasmonic nanocavities," *Nature*, vol. 535, pp. 127–130, 2016.
[81] R. Chikkaraddy, V. A. Turek, N. Kongsuwan, et al., "Mapping nanoscale hotspots with single-molecule emitters assembled into plasmonic nanocavities using DNA origami," *Nano Lett.*, vol. 18, pp. 405–411, 2018.
[82] R. J. Thompson, G. Rempe, and H. J. Kimble, "Observation of normal-mode splitting for an atom in an optical cavity," *Phys. Rev. Lett.*, vol. 68, pp. 1132–1135, 1992.
[83] T. Aoki, B. Dayan, E. Wilcut, et al., "Observation of strong coupling between one atom and a monolithic microresonator," *Nature*, vol. 443, pp. 671–674, 2006.
[84] Y. S. Park, A. K. Cook, and H. Wang, "Cavity QED with diamond nanocrystals and silica microspheres," *Nano Lett.*, vol. 6, pp. 2075–2079, 2006.
[85] C. Santori, M. Pelton, G. Solomon, Y. Dale, and Y. Yamamoto, "Triggered single photons from a quantum dot," *Phys. Rev. Lett.*, vol. 86, pp. 1502–1505, 2001.
[86] T. Yoshie, A. Scherer, J. Hendrickson, et al., "Vacuum Rabi splitting with a single quantum dot in a photonic crystal nanocavity," *Nature*, vol. 432, pp. 200–203, 2004.
[87] A. Shalabney, J. George, J. Hutchison, G. Pupillo, C. Genet, and T. W. Ebbesen, "Coherent coupling of molecular resonators with a microcavity mode," *Nat. Commun.*, vol. 6, p. 5981, 2015.
[88] M. Muallem, A. Palatnik, G. D. Nessim, and Y. R. Tischler, "Strong light-matter coupling and hybridization of molecular vibrations in a low-loss infrared microcavity," *J. Phys. Chem. Lett.*, vol. 7, pp. 2002–2008, 2016.
[89] K. Georgiou, P. Michetti, L. Gai, M. Cavazzini, Z. Shen, and D. G. Lidzey, "Control over energy transfer between fluorescent BODIPY dyes in a strongly coupled microcavity," *ACS Photonics*, vol. 5, pp. 258–266, 2017.
[90] T. G. Tiecke, J. D. Thompson, N. P. de Leon, L. R. Liu, V. Vuletic, and M. D. Lukin, "Nanophotonic quantum phase switch with a single atom," *Nature*, vol. 508, pp. 241–244, 2014.
[91] F. Flamini, N. Spagnolo, and F. Sciarrino, "Photonic quantum information processing: A review," *Rep. Prog. Phys.*, vol. 82, p. 016001, 2019.
[92] M. Saffman, T. G. Walker, and K. Mølmer, "Quantum information with Rydberg atoms," *Rev. Mod. Phys.*, vol. 82, pp. 2313–2363, 2010.
[93] J. R. Maze, P. L. Stanwix, J. S. Hodges, et al., "Nanoscale magnetic sensing with an individual electronic spin in diamond," *Nature*, vol. 455, pp. 644–647, 2008.
[94] F. Dolde, H. Fedder, M. W. Doherty, et al., "Electric-field sensing using single diamond spins," *Nat. Phys.*, vol. 7, pp. 459–463, 2011.
[95] J. B. Fixler, G. T. Foster, J. M. McGuirk, and M. A. Kasevich, "Atom interferometer measurement of the Newtonian constant of gravity," *Science*, vol. 315, pp. 74–77, 2007.
[96] O. S. Ojambati, R. Chikkaraddy, W. D. Deacon, et al., "Quantum electrodynamics at room temperature coupling a single vibrating molecule with a plasmonic nanocavity," *Nat. Commun.*, vol. 10, p. 1049, 2019.
[97] J. Galego, F. J. Garcia-Vidal, and J. Feist, "Cavity-induced modifications of molecular structure in the strong-coupling regime," *Phys. Rev. X*, vol. 5, 2015, https://doi.org/10.1103/physrevx.5.041022.
[98] C. M. Caves, "Quantum-mechanical noise in an interferometer," *Phys. Rev. D*, vol. 23, pp. 1693–1708, 1981.
[99] R. E. Slusher, L. W. Hollberg, B. Yurke, J. C. Mertz, and J. F. Valley, "Observation of squeezed states generated by four-wave mixing in an optical cavity," *Phys. Rev. Lett.*, vol. 55, pp. 2409–2412, 1985.
[100] R. M. Shelby, M. D. Levenson, S. H. Perlmutter, R. G. DeVoe, and D. F. Walls, "Broad-band parametric deamplification of quantum noise in an optical fiber," *Phys. Rev. Lett.*, vol. 57, pp. 691–694, 1986.
[101] L. A. Wu, H. J. Kimble, J. L. Hall, and H. Wu, "Generation of squeezed states by parametric down conversion," *Phys. Rev. Lett.*, vol. 57, pp. 2520–2523, 1986.
[102] M. Mehmet, S. Ast, T. Eberle, S. Steinlechner, H. Vahlbruch, and R. Schnabel, "Squeezed light at 1550 nm with a quantum noise reduction of 12.3 dB," *Opt. Express*, vol. 19, pp. 25763–25772, 2011.
[103] M. Mehmet and H. Vahlbruch, "High-efficiency squeezed light generation for gravitational wave detectors," *Classical Quant. Grav.*, vol. 36, 2019, https://doi.org/10.1088/1361-6382/aaf448.
[104] T. Eberle, S. Steinlechner, J. Bauchrowitz, et al., "Quantum enhancement of the zero-area Sagnac interferometer topology for gravitational wave detection," *Phys. Rev. Lett.*, vol. 104, p. 251102, 2010.
[105] M. S. Stefszky, C. M. Mow-Lowry, S. S. Y. Chua, et al., "Balanced homodyne detection of optical quantum states at audio-band frequencies and below," *Classical Quant. Grav.*, vol. 29, 2012, https://doi.org/10.1088/0264-9381/29/14/145015.
[106] H. Vahlbruch, M. Mehmet, K. Danzmann, and R. Schnabel, "Detection of 15 dB squeezed states of light and their application for the absolute calibration of photoelectric quantum efficiency," *Phys. Rev. Lett.*, vol. 117, p. 110801, 2016.
[107] A. Otterpohl, F. Sedlmeir, U. Vogl, et al., "Squeezed vacuum states from a whispering gallery mode resonator," *Optica*, vol. 6, 2019, https://doi.org/10.1364/optica.6.001375.
[108] R. Loudon and P. L. Knight, "Squeezed light," *J. Mod. Opt.*, vol. 34, pp. 709–759, 1987.
[109] M. Fox, *Quantum Optics: An Introduction*, New York, USA, Oxford University Press, 2006.
[110] X. Sun, Y. Wang, L. Tian, S. Shi, Y. Zheng, and K. Peng, "Dependence of the squeezing and anti-squeezing factors of bright squeezed light on the seed beam power and pump beam noise," *Opt. Lett.*, vol. 44, pp. 1789–1792, 2019.
[111] H. Yonezawa, K. Nagashima, and A. Furusawa, "Generation of squeezed light with a monolithic optical parametric oscillator: simultaneous achievement of phase matching and cavity resonance by temperature control," *Opt. Express*, vol. 18, pp. 20143–20150, 2010.
[112] Y. Zhang, H. Wang, X. Li, J. Jing, C. Xie, and K. Peng, "Experimental generation of bright two-mode quadrature squeezed light from a narrow-band nondegenerate optical parametric amplifier," *Phys. Rev. A*, vol. 62, 2000, https://doi.org/10.1103/physreva.62.023813.
[113] E. G. Lariontsev and I. I. Zolotoverkh, "Characteristics of bright-squeezed light produced in a below-threshold optical

parametric oscillator," *J. Opt. B Quant. Semiclassical Opt.*, vol. 4, pp. 15–19, 2002.
[114] J. T. Barreiro, N. K. Langford, N. A. Peters, and P. G. Kwiat, "Generation of hyperentangled photon pairs," *Phys. Rev. Lett.*, vol. 95, p. 260501, 2005.
[115] P. G. Kwiat, "Hyper-entangled states," *J. Mod. Opt.*, vol. 44, pp. 2173–2184, 1997.
[116] J. P. Dowling, "Quantum optical metrology – the lowdown on high-N00N states," *Contemp. Phys.*, vol. 49, pp. 125–143, 2008.
[117] A. Einstein, B. Podolsky, and N. Rosen, "Can quantum-mechanical description of physical reality Be considered complete?" *Phys. Rev.*, vol. 47, pp. 777–780, 1935.
[118] M. H. Rubin, D. N. Klyshko, Y. H. Shih, and A. V. Sergienko, "Theory of two-photon entanglement in type-II optical parametric down-conversion," *Phys. Rev. A*, vol. 50, pp. 5122–5133, 1994.
[119] L. Caspani, C. Xiong, B. J. Eggleton, et al., "Integrated sources of photon quantum states based on nonlinear optics," *Light Sci. Appl.*, vol. 6, p. e17100, 2017.
[120] R. H. Brown and R. Q. Twiss, "Correlation between photons in two coherent beams of light," *Nature*, vol. 177, pp. 27–29, 1956.
[121] A. J. Bennett, J. P. Lee, D. J. Ellis, et al., "Cavity-enhanced coherent light scattering from a quantum dot," *Sci. Adv.*, vol. 2, p. e1501256, 2016.
[122] L. Hanschke, K. A. Fischer, S. Appel, et al., "Quantum dot single-photon sources with ultra-low multi-photon probability," *Npj Quant. Inf.*, vol. 4, 2018, https://doi.org/10.1038/s41534-018-0092-0.
[123] J.-H. Kim, T. Cai, C. J. K. Richardson, R. P. Leavitt, and E. Waks, "Two-photon interference from a bright single-photon source at telecom wavelengths," *Optica*, vol. 3, 2016, https://doi.org/10.1364/optica.3.000577.
[124] P. Grunwald, "Effective second-order correlation function and single-photon detection," arXiv:1711.05897v3 [quant-ph], 2017.
[125] C. K. Hong, Z. Y. Ou, and L. Mandel, "Measurement of subpicosecond time intervals between two photons by interference," *Phys. Rev. Lett.*, vol. 59, pp. 2044–2046, 1987.
[126] P. B. R. Nisbet-Jones, J. Dilley, D. Ljunggren, and A. Kuhn, "Highly efficient source for indistinguishable single photons of controlled shape," *New J. Phys.*, vol. 13, 2011, https://doi.org/10.1088/1367-2630/13/10/103036.
[127] P. B. R. Nisbet-Jones, J. Dilley, A. Holleczek, O. Barter, and A. Kuhn, "Photonic qubits, qutrits and ququads accurately prepared and delivered on demand," *New J. Phys.*, vol. 15, 2013, https://doi.org/10.1088/1367-2630/15/5/053007.
[128] T. Walker, K. Miyanishi, R. Ikuta, et al., "Long-distance single photon transmission from a trapped ion via quantum frequency conversion," *Phys. Rev. Lett.*, vol. 120, p. 203601, 2018.
[129] T. Legero, T. Wilk, A. Kuhn, and G. Rempe, "Time-resolved two-photon quantum interference," *Appl. Phys. B*, vol. 77, pp. 797–802, 2003.
[130] T. Legero, T. Wilk, M. Hennrich, G. Rempe, and A. Kuhn, "Quantum beat of two single photons," *Phys. Rev. Lett.*, vol. 93, p. 070503, 2004.
[131] T. Walker, S. V. Kashanian, T. Ward, and M. Keller, "Improving the indistinguishability of single photons from an ion-cavity system," *Phys. Rev. A*, vol. 102, p. 032616, 2020.
[132] S. Basiri-Esfahani, C. R. Myers, A. Armin, J. Combes, and G. J. Milburn, "Integrated quantum photonic sensor based on Hong-Ou-Mandel interference," *Opt. Express*, vol. 23, pp. 16008–16023, 2015.
[133] A. Crespi, M. Lobino, J. C. F. Matthews, et al., "Measuring protein concentration with entangled photons," *Appl. Phys. Lett.*, vol. 100, 2012, https://doi.org/10.1063/1.4724105.
[134] S. Daryanoosh, S. Slussarenko, D. W. Berry, H. M. Wiseman, and G. J. Pryde, "Experimental optical phase measurement approaching the exact Heisenberg limit," *Nat. Commun.*, vol. 9, p. 4606, 2018.
[135] R. Okamoto, H. F. Hofmann, T. Nagata, J. L. O'Brien, K. Sasaki, and S. Takeuchi, "Beating the standard quantum limit: phase super-sensitivity ofN-photon interferometers," *New J. Phys.*, vol. 10, 2008, https://doi.org/10.1088/1367-2630/10/7/073033.
[136] T. Nagata, R. Okamoto, L. O'Brien J, K. Sasaki, and S. Takeuchi, "Beating the standard quantum limit with four-entangled photons," *Science*, vol. 316, pp. 726–729, 2007.
[137] B. L. Higgins, D. W. Berry, S. D. Bartlett, H. M. Wiseman, and G. J. Pryde, "Entanglement-free Heisenberg-limited phase estimation," *Nature*, vol. 450, pp. 393–396, 2007.
[138] B. P. Abbott, R. Abbott, T. D. Abbott, et al., "Observation of gravitational waves from a binary black hole merger," *Phys. Rev. Lett.*, vol. 116, p. 061102, 2016.
[139] D. Martens and P. Bienstman, "Comparison between Vernier-cascade and MZI as transducer for biosensing with on-chip spectral filter," *Nanophotonics*, vol. 6, pp. 703–712, 2017.
[140] S. Dante, D. Duval, B. Sepulveda, A. B. Gonzalez-Guerrero, J. R. Sendra, and L. M. Lechuga, "All-optical phase modulation for integrated interferometric biosensors," *Opt. Express*, vol. 20, pp. 7195–7205, 2012.
[141] X. Guan and L. H. Frandsen, "All-silicon interferometer with multimode waveguides for temperature-insensitive filters and compact biosensors," *Opt. Express*, vol. 27, pp. 753–760, 2019.
[142] P. Kozma, F. Kehl, E. Ehrentreich-Forster, C. Stamm, and F. F. Bier, "Integrated planar optical waveguide interferometer biosensors: A comparative review," *Biosens. Bioelectron.*, vol. 58, pp. 287–307, 2014.
[143] A. R. Bastos, C. M. S. Vicente, R. Oliveira-Silva, et al., "Integrated optical mach-zehnder interferometer based on organic-inorganic hybrids for photonics-on-a-chip biosensing applications," *Sensors*, vol. 18, 2018, https://doi.org/10.3390/s18030840.
[144] H. Mukundan, A. S. Anderson, W. K. Grace, et al., "Waveguide-based biosensors for pathogen detection," *Sensors*, vol. 9, pp. 5783–5809, 2009.
[145] Y. Gao, Q. Gan, Z. Xin, X. Cheng, and F. J. Bartoli, "Plasmonic Mach-Zehnder interferometer for ultrasensitive on-chip biosensing," *ACS Nano*, vol. 5, pp. 9836–9844, 2011.
[146] J. Xavier, S. Vincent, F. Meder, and F. Vollmer, "Advances in optoplasmonic sensors – combining optical nano/microcavities and photonic crystals with plasmonic nanostructures and nanoparticles," *Nanophotonics*, vol. 7, pp. 1–38, 2018.
[147] S. Vincent, S. Subramanian, and F. Vollmer, "Optoplasmonic characterisation of reversible disulfide interactions at single

thiol sites in the attomolar regime," *Nat. Commun.*, vol. 11, p. 2043, 2020.
[148] E. Oelker, R. B. Hutson, C. J. Kennedy, et al., "Demonstration of $4.8 \times 10{-}17$ stability at 1 s for two independent optical clocks," *Nat. Photonics*, vol. 13, pp. 714–719, 2019.
[149] S. B. Papp, K. Beha, P. Del'Haye, et al., "Microresonator frequency comb optical clock," *Optica*, vol. 1, 2014, https://doi.org/10.1364/optica.1.000010.
[150] Z. L. Newman, V. Maurice, T. Drake, et al., "Architecture for the photonic integration of an optical atomic clock," *Optica*, vol. 6, 2019, https://doi.org/10.1364/optica.6.000680.
[151] M. A. Taylor, J. Janousek, V. Daria, et al., "Biological measurement beyond the quantum limit," *Nat. Photonics*, vol. 7, pp. 229–233, 2013.
[152] M. A. Taylor, J. Janousek, V. Daria, et al., "Subdiffraction-limited quantum imaging within a living cell," *Phys. Rev. X*, vol. 4, 2014, https://doi.org/10.1103/physrevx.4.011017.
[153] R. C. Pooser and B. Lawrie, "Ultrasensitive measurement of microcantilever displacement below the shot-noise limit," *Optica*, vol. 2, 2015, https://doi.org/10.1364/optica.2.000393.
[154] R. C. Pooser and B. Lawrie, "Plasmonic trace sensing below the photon shot noise limit," *ACS Photonics*, vol. 3, pp. 8–13, 2016.
[155] N. P. Mauranyapin, L. S. Madsen, M. A. Taylor, M. Waleed, and W. P. Bowen, "Evanescent single-molecule biosensing with quantum-limited precision," *Nat. Photonics*, vol. 11, pp. 477–481, 2017.
[156] M. Dowran, A. Kumar, B. J. Lawrie, R. C. Pooser, and A. M. Marino, "Quantum-enhanced plasmonic sensing," *Optica*, vol. 5, 2018, https://doi.org/10.1364/optica.5.000628.
[157] B.-B. Li, J. Bílek, U. B. Hoff, et al., "Quantum enhanced optomechanical magnetometry," *Optica*, vol. 5, 2018, https://doi.org/10.1364/optica.5.000850.
[158] J. S. Lee, S. J. Yoon, H. Rah, et al., "Quantum plasmonic sensing using single photons," *Opt. Express*, vol. 26, pp. 29272–29282, 2018.
[159] R. B. de Andrade, H. Kerdoncuff, K. Berg-Sørensen, T. Gehring, M. Lassen, and U. L. Andersen, "Quantum-enhanced continuous-wave stimulated Raman scattering spectroscopy," *Optica*, vol. 7, 2020, https://doi.org/10.1364/optica.386584.
[160] G. Triginer Garces, H. M. Chrzanowski, S. Daryanoosh, et al., "Quantum-enhanced stimulated emission detection for label-free microscopy," *Appl. Phys. Lett.*, vol. 117, 2020, https://doi.org/10.1063/5.0009681.
[161] C. A. Casacio, L. S. Madsen, A. Terrasson, et al., "Quantum correlations overcome the photodamage limits of light microscopy," arXiv:2004.00178v2 [physics.optics], 2020.
[162] D. I. Lee and T. Goodson, 3rd, "Entangled photon absorption in an organic porphyrin dendrimer," *J. Phys. Chem. B*, vol. 110, pp. 25582–25585, 2006.
[163] S. M. Eaton, J. P. Hadden, V. Bharadwaj, et al., "Quantum micro–nano devices fabricated in diamond by femtosecond laser and ion irradiation," *Adv. Quant. Technol.*, vol. 2, 2019, https://doi.org/10.1002/qute.201970033.
[164] M. W. Doherty, N. B. Manson, P. Delaney, F. Jelezko, J. Wrachtrup, and L. C. L. Hollenberg, "The nitrogen-vacancy colour centre in diamond," *Phys. Rep.*, vol. 528, pp. 1–45, 2013.
[165] R. Brouri, A. Beveratos, J. P. Poizat, and P. Grangier, "Photon antibunching in the fluorescence of individual color centers in diamond," *Opt. Lett.*, vol. 25, pp. 1294–1296, 2000.
[166] C. Kurtsiefer, S. Mayer, P. Zarda, and H. Weinfurter, "Stable solid-state source of single photons," *Phys. Rev. Lett.*, vol. 85, pp. 290–293, 2000.
[167] A. Beveratos, R. Brouri, T. Gacoin, J.-P. Poizat, and P. Grangier, "Nonclassical radiation from diamond nanocrystals," *Phys. Rev. A*, vol. 64, 2001, https://doi.org/10.1103/physreva.64.061802.
[168] V. N. Mochalin, O. Shenderova, D. Ho, and Y. Gogotsi, "The properties and applications of nanodiamonds," *Nat. Nanotechnol.*, vol. 7, pp. 11–23, 2011.
[169] D. D. B. Rao, S. Yang, and J. Wrachtrup, "Generation of entangled photon strings using NV centers in diamond," *Phys. Rev. B*, vol. 92, 2015, https://doi.org/10.1103/physrevb.92.081301.
[170] J.-M. Li, M. Hua, and X.-Q. Yan, "NOON state generation with phonons in acoustic wave resonators assisted by a nitrogen-vacancy-center ensemble," *Ann. Phys.*, vol. 531, 2019, https://doi.org/10.1002/andp.201800430.
[171] T. M. Babinec, B. J. Hausmann, M. Khan, et al., "A diamond nanowire single-photon source," *Nat. Nanotechnol.*, vol. 5, pp. 195–199, 2010.
[172] K. G. Lee, X. W. Chen, H. Eghlidi, et al., "A planar dielectric antenna for directional single-photon emission and near-unity collection efficiency," *Nat. Photonics*, vol. 5, pp. 166–169, 2011.
[173] A. Faraon, C. Santori, Z. Huang, et al., "Quantum photonic devices in single-crystal diamond," *New J. Phys.*, vol. 15, 2013, https://doi.org/10.1088/1367-2630/15/2/025010.
[174] M. Gould, E. R. Schmidgall, S. Dadgostar, F. Hatami, and K.-M. C. Fu, "Efficient extraction of zero-phonon-line photons from single nitrogen-vacancy centers in an integrated GaP-on-Diamond platform," *Phys. Rev. Appl.*, vol. 6, 2016, https://doi.org/10.1103/physrevapplied.6.011001.
[175] E. R. Schmidgall, S. Chakravarthi, M. Gould, et al., "Frequency control of single quantum emitters in integrated photonic circuits," *Nano Lett.*, vol. 18, pp. 1175–1179, 2018.
[176] V. Bharadwaj, O. Jedrkiewicz, J. P. Hadden, et al., "Femtosecond laser written photonic and microfluidic circuits in diamond," *J. Phys. Photonics*, vol. 1, 2019, https://doi.org/10.1088/2515-7647/ab0c4e.
[177] F. Lenzini, N. Gruhler, N. Walter, and W. H. P. Pernice, "Diamond as a platform for integrated quantum photonics," *Adv. Quant. Technol.*, vol. 1, 2018, https://doi.org/10.1002/qute.201870031.
[178] W. R. Algar, A. J. Tavares, and U. J. Krull, "Beyond labels: A review of the application of quantum dots as integrated components of assays, bioprobes, and biosensors utilizing optical transduction," *Anal. Chim. Acta*, vol. 673, pp. 1–25, 2010.
[179] M. Muller, H. Vural, C. Schneider, et al., "Quantum-dot single-photon sources for entanglement enhanced interferometry," *Phys. Rev. Lett.*, vol. 118, p. 257402, 2017.
[180] R. Katsumi, Y. Ota, A. Osada, et al., "Quantum-dot single-photon source on a CMOS silicon photonic chip integrated using transfer printing," *APL Photonics*, vol. 4, 2019, https://doi.org/10.1063/1.5087263.
[181] R. S. Daveau, K. C. Balram, T. Pregnolato, et al., "Efficient fiber-coupled single-photon source based on quantum dots in a photonic-crystal waveguide," *Optica*, vol. 4, pp. 178–184, 2017.

[182] C. L. Dreeßen, C. Ouellet-Plamondon, P. Tighineanu, et al., "Suppressing phonon decoherence of high performance single-photon sources in nanophotonic waveguides," *Quant. Sci. Technol.*, vol. 4, 2018, https://doi.org/10.1088/2058-9565/aadbb8.
[183] Sparrow single-photon source. Available at: https://sparrowquantum.com/ [accessed: Jan. 30, 2019].
[184] P. Lombardi, A. P. Ovvyan, S. Pazzagli, et al., "Photostable molecules on chip: integrated sources of nonclassical light," *ACS Photonics*, vol. 5, pp. 126–132, 2017.
[185] K. Santhosh, O. Bitton, L. Chuntonov, and G. Haran, "Vacuum Rabi splitting in a plasmonic cavity at the single quantum emitter limit," *Nat. Commun.*, vol. 7, p. ncomms11823, 2016.
[186] J. Wrachtrup, "2D materials: single photons at room temperature," *Nat. Nanotechnol.*, vol. 11, pp. 7–8, 2016.
[187] T. T. Tran, C. Zachreson, A. M. Berhane, et al., "Quantum emission from defects in single-crystalline hexagonal boron nitride," *Phys. Rev. Appl.*, vol. 5, 2016, https://doi.org/10.1103/physrevapplied.5.034005.
[188] T. T. Tran, K. Bray, M. J. Ford, M. Toth, and I. Aharonovich, "Quantum emission from hexagonal boron nitride monolayers," *Nat. Nanotechnol.*, vol. 11, pp. 37–41, 2016.
[189] S. Castelletto, F. A. Inam, S. I. Sato, and A. Boretti, "Hexagonal boron nitride: A review of the emerging material platform for single-photon sources and the spin-photon interface," *Beilstein J. Nanotechnol.*, vol. 11, pp. 740–769, 2020.
[190] S. Kim, J. E. Froch, J. Christian, et al., "Photonic crystal cavities from hexagonal boron nitride," *Nat. Commun.*, vol. 9, p. 2623, 2018.
[191] M. K. Boll, I. P. Radko, A. Huck, and U. L. Andersen, "Photophysics of quantum emitters in hexagonal boron-nitride nano-flakes," *Opt. Express*, vol. 28, pp. 7475–7487, 2020.
[192] T. Vogl, G. Campbell, B. C. Buchler, Y. Lu, and P. K. Lam, "Fabrication and deterministic transfer of high-quality quantum emitters in hexagonal boron nitride," *ACS Photonics*, vol. 5, pp. 2305–2312, 2018.
[193] N. R. Jungwirth, B. Calderon, Y. Ji, M. G. Spencer, M. E. Flatte, and G. D. Fuchs, "Temperature dependence of wavelength selectable zero-phonon emission from single defects in hexagonal boron nitride," *Nano Lett.*, vol. 16, pp. 6052–6057, 2016.
[194] G. Grosso, H. Moon, B. Lienhard, et al., "Tunable and high-purity room temperature single-photon emission from atomic defects in hexagonal boron nitride," *Nat. Commun.*, vol. 8, p. 705, 2017.
[195] N. Mendelson, M. Doherty, M. Toth, I. Aharonovich, and T. T. Tran, "Strain-induced modification of the optical characteristics of quantum emitters in hexagonal boron nitride," *Adv. Mater.*, vol. 32, p. e1908316, 2020.
[196] F. Hayee, L. Yu, J. L. Zhang, et al., "Revealing multiple classes of stable quantum emitters in hexagonal boron nitride with correlated optical and electron microscopy," *Nat. Mater.*, vol. 19, pp. 534–539, 2020.
[197] N. Mendelson, Z. Q. Xu, T. T. Tran, et al., "Engineering and tuning of quantum emitters in few-layer hexagonal boron nitride," *ACS Nano*, vol. 13, pp. 3132–3140, 2019.
[198] D. Yim, M. Yu, G. Noh, J. Lee, and H. Seo, "Polarization and localization of single-photon emitters in hexagonal boron nitride wrinkles," *ACS Appl. Mater. Interfaces*, vol. 12, pp. 36362–36369, 2020.
[199] A. W. Schell, H. Takashima, T. T. Tran, I. Aharonovich, and S. Takeuchi, "Coupling quantum emitters in 2D materials with tapered fibers," *ACS Photonics*, vol. 4, pp. 761–767, 2017.
[200] T. Vogl, Y. Lu, and P. Koy Lam, "Room temperature single photon source using fiber-integrated hexagonal boron nitride," *J. Phys. D*, vol. 50, 2017, https://doi.org/10.1088/1361-6463/aa7839.
[201] M. Abdi, M. J. Hwang, M. Aghtar, and M. B. Plenio, "Spin-mechanical scheme with color centers in hexagonal boron nitride membranes," *Phys. Rev. Lett.*, vol. 119, p. 233602, 2017.
[202] A. L. Exarhos, D. A. Hopper, R. N. Patel, M. W. Doherty, and L. C. Bassett, "Magnetic-field-dependent quantum emission in hexagonal boron nitride at room temperature," *Nat. Commun.*, vol. 10, p. 222, 2019.
[203] A. Gottscholl, M. Kianinia, V. Soltamov, et al., "Initialization and read-out of intrinsic spin defects in a van der Waals crystal at room temperature," *Nat. Mater.*, vol. 19, pp. 540–545, 2020.
[204] R. W. Boyd, *Nonlinear Optics*, 3rd ed. USA, Academic Press, Inc., 2008.
[205] D. V. Strekalov, C. Marquardt, A. B. Matsko, H. G. L. Schwefel, and G. Leuchs, "Nonlinear and quantum optics with whispering gallery resonators," *J. Opt.*, vol. 18, 2016, https://doi.org/10.1088/2040-8978/18/12/123002.
[206] S. Tanzilli, H. De Riedmatten, W. Tittel, et al., "Highly efficient photon-pair source using periodically poled lithium niobate waveguide," *Electron. Lett.*, vol. 37, 2001, https://doi.org/10.1049/el:20010009.
[207] G. Fujii, M. Motoya, N. Namekata, S. Inoue, and S. Kurimura, "Generation of narrowband photon-pairs in 1550 nm band using Type-II periodically poled lithium niobate waveguide," in *CLEO/Europe and IQEC 2007 Conference Digest*, Munich, Optical Society of America, 2007.
[208] H. Herrmann, X. Yang, A. Thomas, A. Poppe, W. Sohler, and C. Silberhorn, "Post-selection free, integrated optical source of non-degenerate, polarization entangled photon pairs," *Opt. Express*, vol. 21, pp. 27981–27991, 2013.
[209] M. Fortsch, J. U. Furst, C. Wittmann, et al., "A versatile source of single photons for quantum information processing," *Nat. Commun.*, vol. 4, p. 1818, 2013.
[210] Z. Ma, J. Y. Chen, Z. Li, et al., "Ultrabright quantum photon sources on chip," *Phys. Rev. Lett.*, vol. 125, p. 263602, 2020.
[211] G. Schunk, U. Vogl, D. V. Strekalov, et al., "Interfacing transitions of different alkali atoms and telecom bands using one narrowband photon pair source," *Optica*, vol. 2, 2015, https://doi.org/10.1364/optica.2.000773.
[212] R. Horn, P. Abolghasem, B. J. Bijlani, D. Kang, A. S. Helmy, and G. Weihs, "Monolithic source of photon pairs," *Phys. Rev. Lett.*, vol. 108, p. 153605, 2012.
[213] L. Lanco, S. Ducci, J. P. Likforman, et al., "Backward difference frequency generation in an AlGaAs waveguide," *Appl. Phys. Lett.*, vol. 89, 2006, https://doi.org/10.1063/1.2226996.
[214] X. Guo, C. L. Zou, C. Schuck, H. Jung, R. Cheng, and H. X. Tang, "Parametric down-conversion photon-pair source on a nanophotonic chip," *Light Sci. Appl.*, vol. 6, p. e16249, 2017.
[215] V. D. Vaidya, B. Morrison, L. G. Helt, et al., "Broadband quadrature-squeezed vacuum and nonclassical photon number correlations from a nanophotonic device," *Sci. Adv.*, vol. 6, 2020, https://doi.org/10.1126/sciadv.aba9186.
[216] Y. Zhao, Y. Okawachi, J. K. Jang, X. Ji, M. Lipson, and A. L. Gaeta, "Near-degenerate quadrature-squeezed vacuum generation on a silicon-nitride chip," *Phys. Rev. Lett.*, vol. 124, p. 193601, 2020.

[217] N. Aggarwal, T. J. Cullen, J. Cripe, et al., "Room-temperature optomechanical squeezing," *Nat. Phys.*, vol. 16, pp. 784–788, 2020.
[218] P. Kultavewuti, E. Y. Zhu, L. Qian, V. Pusino, M. Sorel, and J. Stewart Aitchison, "Correlated photon pair generation in AlGaAs nanowaveguides via spontaneous four-wave mixing," *Opt. Express*, vol. 24, pp. 3365–3376, 2016.
[219] J. E. Sharping, K. F. Lee, M. A. Foster, et al., "Generation of correlated photons in nanoscale silicon waveguides," *Opt. Express*, vol. 14, pp. 12388–12393, 2006.
[220] H. Takesue, Y. Tokura, H. Fukuda, et al., "Entanglement generation using silicon wire waveguide," *Appl. Phys. Lett.*, vol. 91, 2007, https://doi.org/10.1063/1.2814040.
[221] M. Zhang, L. T. Feng, Z. Y. Zhou, et al., "Generation of multiphoton quantum states on silicon," *Light Sci. Appl.*, vol. 8, p. 41, 2019.
[222] S. Paesani, Y. Ding, R. Santagati, et al., "Generation and sampling of quantum states of light in a silicon chip," *Nat. Phys.*, vol. 15, pp. 925–929, 2019.
[223] S. Clemmen, K. Phan Huy, W. Bogaerts, R. G. Baets, P. Emplit, and S. Massar, "Continuous wave photon pair generation in silicon-on-insulator waveguides and ring resonators," *Opt. Express*, vol. 17, pp. 16558–16570, 2009.
[224] S. Azzini, D. Grassani, M. J. Strain, et al., "Ultra-low power generation of twin photons in a compact silicon ring resonator," *Opt. Express*, vol. 20, pp. 23100–23107, 2012.
[225] E. Engin, D. Bonneau, C. M. Natarajan, et al., "Photon pair generation in a silicon micro-ring resonator with reverse bias enhancement," *Opt. Express*, vol. 21, pp. 27826–27834, 2013.
[226] Y. Guo, W. Zhang, S. Dong, Y. Huang, and J. Peng, "Telecom-band degenerate-frequency photon pair generation in silicon microring cavities," *Opt. Lett.*, vol. 39, pp. 2526–2529, 2014.
[227] W. C. Jiang, X. Lu, J. Zhang, O. Painter, and Q. Lin, "Silicon-chip source of bright photon pairs," *Opt. Express*, vol. 23, pp. 20884–20904, 2015.
[228] J. A. Steidle, M. L. Fanto, C. C. Tison, Z. Wang, P. M. Alsing, and S. F. Preble, "Efficiently heralded silicon ring resonator photon-pair source," in *Quantum Information and Computation IX*, Baltimore, Maryland, United States, 2016, https://doi.org/10.1117/12.2223941.
[229] X. Lu, W. C. Jiang, J. Zhang, and Q. Lin, "Biphoton statistics of quantum light generated on a silicon chip," *ACS Photonics*, vol. 3, pp. 1626–1636, 2016.
[230] M. Savanier, R. Kumar, and S. Mookherjea, "Photon pair generation from compact silicon microring resonators using microwatt-level pump powers," *Opt. Express*, vol. 24, pp. 3313–3328, 2016.
[231] S. Rogers, X. Lu, W. C. Jiang, and Q. Lin, "Twin photon pairs in a high-Q silicon microresonator," *Appl. Phys. Lett.*, vol. 107, 2015, https://doi.org/10.1063/1.4927540.
[232] D. Grassani, S. Azzini, M. Liscidini, et al., "Micrometer-scale integrated silicon source of time-energy entangled photons," *Optica*, vol. 2, 2015, https://doi.org/10.1364/optica.2.000088.
[233] R. Wakabayashi, M. Fujiwara, K. Yoshino, Y. Nambu, M. Sasaki, and T. Aoki, "Time-bin entangled photon pair generation from Si micro-ring resonator," *Opt. Express*, vol. 23, pp. 1103–1113, 2015.
[234] C. Ma, X. Wang, V. Anant, A. D. Beyer, M. D. Shaw, and S. Mookherjea, "Silicon photonic entangled photon-pair and heralded single photon generation with CAR > 12,000 and g^(2)(0) < 0006," *Opt. Express*, vol. 25, 2017, https://doi.org/10.1364/oe.25.032995.
[235] J. Suo, S. Dong, W. Zhang, Y. Huang, and J. Peng, "Generation of hyper-entanglement on polarization and energy-time based on a silicon micro-ring cavity," *Opt. Express*, vol. 23, pp. 3985–3995, 2015.
[236] C. Ma and S. Mookherjea, "Simultaneous dual-band entangled photon pair generation using a silicon photonic microring resonator," *Quant. Sci. Technol.*, vol. 3, 2018, https://doi.org/10.1088/2058-9565/aab89a.
[237] A. Dutt, K. Luke, S. Manipatruni, A. L. Gaeta, P. Nussenzveig, and M. Lipson, "On-chip optical squeezing," *Phys. Rev. Appl.*, vol. 3, 2015, https://doi.org/10.1103/physrevapplied.3.044005.
[238] R. R. Kumar, M. Raevskaia, V. Pogoretskii, Y. Jiao, and H. K. Tsang, "Entangled photon pair generation from an InP membrane micro-ring resonator," *Appl. Phys. Lett.*, vol. 114, 2019, https://doi.org/10.1063/1.5080397.
[239] X. Wang, C. Ma, R. Kumar, et al., "Photon pair generation using a silicon photonic hybrid laser," *APL Photonics*, vol. 3, 2018, https://doi.org/10.1063/1.5040118.
[240] M. Kues, C. Reimer, J. M. Lukens, et al., "Quantum optical microcombs," *Nat. Photonics*, vol. 13, pp. 170–179, 2019.
[241] S. A. Diddams, L. Hollberg, and V. Mbele, "Molecular fingerprinting with the resolved modes of a femtosecond laser frequency comb," *Nature*, vol. 445, pp. 627–630, 2007.
[242] C. Reimer, M. Kues, P. Roztocki, et al., "On-chip quantum frequency combs," *Opt. Photonics News*, vol. 27, 2016, https://doi.org/10.1364/opn.27.12.000046.
[243] L. Caspani, C. Reimer, M. Kues, et al., "Multifrequency sources of quantum correlated photon pairs on-chip: A path toward integrated Quantum Frequency Combs," *Nanophotonics*, vol. 5, pp. 351–362, 2016.
[244] D. J. Jones, S. A. Diddams, J. K. Ranka, et al., "Carrier-envelope phase control of femtosecond mode-locked lasers and direct optical frequency synthesis," *Science*, vol. 288, pp. 635–640, 2000.
[245] T. Fortier and E. Baumann, "20 years of developments in optical frequency comb technology and applications," *Commun. Phys.*, vol. 2, 2019, https://doi.org/10.1038/s42005-019-0249-y.
[246] T. M. Fortier, P. A. Roos, D. J. Jones, S. T. Cundiff, R. D. Bhat, and J. E. Sipe, "Carrier-envelope phase-controlled quantum interference of injected photocurrents in semiconductors," *Phys. Rev. Lett.*, vol. 92, p. 147403, 2004.
[247] A. L. Gaeta, M. Lipson, and T. J. Kippenberg, "Photonic-chip-based frequency combs," *Nat. Photonics*, vol. 13, pp. 158–169, 2019.
[248] C. Reimer, L. Caspani, M. Clerici, et al., "Integrated frequency comb source of heralded single photons," *Opt. Express*, vol. 22, pp. 6535–6546, 2014.
[249] C. Reimer, M. Kues, P. Roztocki, et al., "Generation of multiphoton entangled quantum states by means of integrated frequency combs," *Science*, vol. 351, pp. 1176–1180, 2016.

[250] M. Kues, C. Reimer, P. Roztocki, et al., "On-chip generation of high-dimensional entangled quantum states and their coherent control," *Nature*, vol. 546, pp. 622–626, 2017.
[251] M. Kost, J. Cai, and M. B. Plenio, "Resolving single molecule structures with Nitrogen-vacancy centers in diamond," *Sci. Rep.*, vol. 5, p. 11007, 2015.
[252] G. Q. Liu, X. Feng, N. Wang, Q. Li, and R. B. Liu, "Coherent quantum control of nitrogen-vacancy center spins near 1000 kelvin," *Nat. Commun.*, vol. 10, p. 1344, 2019.
[253] G. Balasubramanian, I. Y. Chan, R. Kolesov, et al., "Nanoscale imaging magnetometry with diamond spins under ambient conditions," *Nature*, vol. 455, pp. 648–651, 2008.
[254] S. J. DeVience, L. M. Pham, I. Lovchinsky, et al., "Nanoscale NMR spectroscopy and imaging of multiple nuclear species," *Nat. Nanotechnol.*, vol. 10, pp. 129–134, 2015.
[255] P. Neumann, I. Jakobi, F. Dolde, et al., "High-precision nanoscale temperature sensing using single defects in diamond," *Nano Lett.*, vol. 13, pp. 2738–2742, 2013.
[256] G. Kucsko, P. C. Maurer, N. Y. Yao, et al., "Nanometre-scale thermometry in a living cell," *Nature*, vol. 500, pp. 54–58, 2013.
[257] J. F. Barry, M. J. Turner, J. M. Schloss, et al., "Optical magnetic detection of single-neuron action potentials using quantum defects in diamond," *Proc. Natl. Acad. Sci. U.S.A.*, vol. 113, pp. 14133–14138, 2016.
[258] M. Alkahtani, L. Jiang, R. Brick, P. Hemmer, and M. Scully, "Nanometer-scale luminescent thermometry in bovine embryos," *Opt. Lett.*, vol. 42, pp. 4812–4815, 2017.
[259] G. Petrini, E. Moreva, E. Bernardi, et al., "Is a quantum biosensing revolution approaching? Perspectives in NV-assisted current and thermal biosensing in living cells," *Adv. Quant. Technol.*, vol. 3, 2020, https://doi.org/10.1002/qute.202000066.
[260] J. F. Barry, J. M. Schloss, E. Bauch, et al., "Sensitivity optimization for NV-diamond magnetometry," *Rev. Mod. Phys.*, vol. 92, 2020, https://doi.org/10.1103/revmodphys.92.015004.
[261] C. Bradac, W. Gao, J. Forneris, M. E. Trusheim, and I. Aharonovich, "Quantum nanophotonics with group IV defects in diamond," *Nat. Commun.*, vol. 10, p. 5625, 2019.
[262] J. N. Becker and C. Becher, "Coherence properties and quantum control of silicon vacancy color centers in diamond," *Phys. Status Solidi*, vol. 214, 2017, https://doi.org/10.1002/pssa.201770170.
[263] B. K. Ofori-Okai, S. Pezzagna, K. Chang, et al., "Spin properties of very shallow nitrogen vacancy defects in diamond," *Phys. Rev. B*, vol. 86, 2012, https://doi.org/10.1103/physrevb.86.081406.
[264] A. O. Sushkov, I. Lovchinsky, N. Chisholm, R. L. Walsworth, H. Park, and M. D. Lukin, "Magnetic resonance detection of individual proton spins using quantum reporters," *Phys. Rev. Lett.*, vol. 113, p. 197601, 2014.
[265] Y. X. Liu, A. Ajoy, and P. Cappellaro, "Nanoscale vector dc magnetometry via ancilla-assisted frequency up-conversion," *Phys. Rev. Lett.*, vol. 122, p. 100501, 2019.
[266] F. Alghannam and P. Hemmer, "Engineering of shallow layers of nitrogen vacancy colour centres in diamond using plasma immersion ion implantation," *Sci. Rep.*, vol. 9, p. 5870, 2019.
[267] C. Osterkamp, M. Mangold, J. Lang, et al., "Engineering preferentially-aligned nitrogen-vacancy centre ensembles in CVD grown diamond," *Sci. Rep.*, vol. 9, p. 5786, 2019.
[268] M. Alkahtani and P. Hemmer, "Charge stability of nitrogen-vacancy color centers in organic nanodiamonds," *Opt. Mater. Express*, vol. 10, 2020, https://doi.org/10.1364/ome.392503.
[269] I. Schwartz, J. Scheuer, B. Tratzmiller, et al., "Robust optical polarization of nuclear spin baths using Hamiltonian engineering of nitrogen-vacancy center quantum dynamics," *Sci. Adv.*, vol. 4, p. eaat8978, 2018.
[270] A. Equbal, K. Tagami, and S. Han, "Pulse-shaped dynamic nuclear polarization under magic-angle spinning," *J. Phys. Chem. Lett.*, vol. 10, pp. 7781–7788, 2019.
[271] C. Lei, S. Peng, C. Ju, M. H. Yung, and J. Du, "Decoherence control of nitrogen-vacancy centers," *Sci. Rep.*, vol. 7, p. 11937, 2017.
[272] J. Holzgrafe, J. Beitner, D. Kara, H. S. Knowles, and M. Atatüre, "Error corrected spin-state readout in a nanodiamond," *Npj Quant. Inf.*, vol. 5, 2019, https://doi.org/10.1038/s41534-019-0126-2.
[273] I. Lovchinsky, A. O. Sushkov, E. Urbach, et al., "Nuclear magnetic resonance detection and spectroscopy of single proteins using quantum logic," *Science*, vol. 351, pp. 836–841, 2016.
[274] N. Aharon, A. Rotem, L. P. McGuinness, F. Jelezko, A. Retzker, and Z. Ringel, "NV center based nano-NMR enhanced by deep learning," *Sci. Rep.*, vol. 9, p. 17802, 2019.
[275] D. Kim, M. I. Ibrahim, C. Foy, M. E. Trusheim, R. Han, and D. R. Englund, "A CMOS-integrated quantum sensor based on nitrogen–vacancy centres," *Nat. Electron.*, vol. 2, pp. 284–289, 2019.
[276] S. Maayani, C. Foy, D. Englund, and Y. Fink, "Distributed quantum fiber magnetometry," *Laser. Photonics Rev.*, vol. 13, 2019, https://doi.org/10.1002/lpor.201900075.
[277] S. Zeng, D. Baillargeat, H. P. Ho, and K. T. Yong, "Nanomaterials enhanced surface plasmon resonance for biological and chemical sensing applications," *Chem. Soc. Rev.*, vol. 43, pp. 3426–3452, 2014.
[278] E. Kretschmann and H. Raether, "Notizen: radiative decay of non radiative surface plasmons excited by light," *Z. Naturforsch.*, vol. 23, pp. 2135–2136, 1968.
[279] M. Sarkar, M. Besbes, J. Moreau, et al., "Hybrid plasmonic mode by resonant coupling of localized plasmons to propagating plasmons in a Kretschmann configuration," *ACS Photonics*, vol. 2, pp. 237–245, 2015.
[280] L. Li, Y. Liang, J. Guang, et al., "Dual Kretschmann and Otto configuration fiber surface plasmon resonance biosensor," *Opt. Express*, vol. 25, pp. 26950–26957, 2017.
[281] S. Frustaci and F. Vollmer, "Whispering-gallery mode (WGM) sensors: review of established and WGM-based techniques to study protein conformational dynamics," *Curr. Opin. Chem. Biol.*, vol. 51, pp. 66–73, 2019.
[282] J. Proust, J. Martin, D. Gerard, J. L. Bijeon, and J. Plain, "Detecting a zeptogram of pyridine with a hybrid plasmonic-photonic nanosensor," *ACS Sens.*, vol. 4, pp. 586–594, 2019.
[283] C. Wang, L.-Q. Chen, Y.-M. Chen, and C.-W. Lin, "Hot electron based surface plasmon resonance sensor with Au-TiO2-Ti planar micro-comb structure Schottky diodes," in *Plasmonics in Biology and Medicine XVI*, San Francisco, California, United States, SPIE BiOS, 2019.
[284] A. K. Sharma, R. Jha, and B. D. Gupta, "Fiber-optic sensors based on surface plasmon resonance: A comprehensive review," *IEEE Sens. J.*, vol. 7, pp. 1118–1129, 2007.

[285] J. R. Mejia-Salazar and O. N. Oliveira, Jr., "Plasmonic biosensing," *Chem. Rev.*, vol. 118, pp. 10617–10625, 2018.
[286] P. L. Stiles, J. A. Dieringer, N. C. Shah, and R. P. Van Duyne, "Surface-enhanced Raman spectroscopy," *Annu. Rev. Anal. Chem.*, vol. 1, pp. 601–626, 2008.
[287] Y. Yang, J. Shi, G. Kawamura, and M. Nogami, "Preparation of Au–Ag, Ag–Au core–shell bimetallic nanoparticles for surface-enhanced Raman scattering," *Scripta Mater.*, vol. 58, pp. 862–865, 2008.
[288] R. M. Stöckle, Y. D. Suh, V. Deckert, and R. Zenobi, "Nanoscale chemical analysis by tip-enhanced Raman spectroscopy," *Chem. Phys. Lett.*, vol. 318, pp. 131–136, 2000.
[289] J. R. Anema, J. F. Li, Z. L. Yang, B. Ren, and Z. Q. Tian, "Shell-isolated nanoparticle-enhanced Raman spectroscopy: expanding the versatility of surface-enhanced Raman scattering," *Annu. Rev. Anal. Chem.*, vol. 4, pp. 129–150, 2011.
[290] J. F. Li, Y. F. Huang, Y. Ding, et al., "Shell-isolated nanoparticle-enhanced Raman spectroscopy," *Nature*, vol. 464, pp. 392–395, 2010.
[291] J. F. Li, J. R. Anema, T. Wandlowski, and Z. Q. Tian, "Dielectric shell isolated and graphene shell isolated nanoparticle enhanced Raman spectroscopies and their applications," *Chem. Soc. Rev.*, vol. 44, pp. 8399–8409, 2015.
[292] E. Kim, M. D. Baaske, and F. Vollmer, "In situ observation of single-molecule surface reactions from low to high affinities," *Adv. Mater.*, vol. 28, pp. 9941–9948, 2016.
[293] S. Subramanian, H. Y. Wu, T. Constant, J. Xavier, and F. Vollmer, "Label-free optical single-molecule micro- and nanosensors," *Adv. Mater.*, vol. 30, p. e1801246, 2018.
[294] E. Kim, M. D. Baaske, I. Schuldes, P. S. Wilsch, and F. Vollmer, "Label-free optical detection of single enzyme-reactant reactions and associated conformational changes," *Sci. Adv.*, vol. 3, p. e1603044, 2017.
[295] P. Narang, R. Sundararaman, and H. A. Atwater, "Plasmonic hot carrier dynamics in solid-state and chemical systems for energy conversion," *Nanophotonics*, vol. 5, pp. 96–111, 2016.
[296] H. Shan, Y. Yu, X. Wang, et al., "Direct observation of ultrafast plasmonic hot electron transfer in the strong coupling regime," *Light Sci. Appl.*, vol. 8, p. 9, 2019.
[297] B. J. Lawrie, P. G. Evans, and R. C. Pooser, "Extraordinary optical transmission of multimode quantum correlations via localized surface plasmons," *Phys. Rev. Lett.*, vol. 110, p. 156802, 2013.
[298] A. Huck, S. Smolka, P. Lodahl, et al., "Demonstration of quadrature-squeezed surface plasmons in a gold waveguide," *Phys. Rev. Lett.*, vol. 102, p. 246802, 2009.
[299] M. Tame and C. Lee, "Plasmonics and sensing beyond classical limits," in *Quantum Nanophotonic Materials, Devices, and Systems 2019*, San Diego, California, United States, SPIE Nanoscience + Engineering, 2019.
[300] Y. Chen, C. Lee, L. Lu, et al., "Quantum plasmonic N00N state in a silver nanowire and its use for quantum sensing," *Optica*, vol. 5, 2018, https://doi.org/10.1364/optica.5.001229.
[301] B. Huttner and S. M. Barnett, "Quantization of the electromagnetic field in dielectrics," *Phys. Rev. A*, vol. 46, pp. 4306–4322, 1992.
[302] T. G. Philbin, "Canonical quantization of macroscopic electromagnetism," *New J. Phys.*, vol. 12, 2010, https://doi.org/10.1088/1367-2630/12/12/123008.
[303] W. Zhu, R. Esteban, A. G. Borisov, et al., "Quantum mechanical effects in plasmonic structures with subnanometre gaps," *Nat. Commun.*, vol. 7, p. 11495, 2016.
[304] J. Ma, Z. Wang, and L. W. Wang, "Interplay between plasmon and single-particle excitations in a metal nanocluster," *Nat. Commun.*, vol. 6, p. 10107, 2015.
[305] S. Lerch and B. M. Reinhard, "Quantum plasmonics: optical monitoring of DNA-mediated charge transfer in plasmon rulers," *Adv. Mater.*, vol. 28, pp. 2030–2036, 2016.
[306] Y. Zhu, Z. Li, Z. Hao, et al., "Optical conductivity-based ultrasensitive mid-infrared biosensing on a hybrid metasurface," *Light Sci. Appl.*, vol. 7, p. 67, 2018.
[307] Z. Qian, J. Ren, F. Zhang, X. Duan, Q. Gong, and Y. Gu, "Nanoscale quantum plasmon sensing based on strong photon-exciton coupling," *Nanotechnology*, vol. 31, p. 125001, 2020.
[308] C.-H. Dong, X.-F. Ren, R. Yang, et al., "Coupling of light from an optical fiber taper into silver nanowires," *Appl. Phys. Lett.*, vol. 95, 2009, https://doi.org/10.1063/1.3270530.
[309] F. Marquier, C. Sauvan, and J.-J. Greffet, "Revisiting quantum optics with surface plasmons and plasmonic resonators," *ACS Photonics*, vol. 4, pp. 2091–2101, 2017.
[310] M. Pelton, S. D. Storm, and H. Leng, "Strong coupling of emitters to single plasmonic nanoparticles: exciton-induced transparency and Rabi splitting," *Nanoscale*, vol. 11, pp. 14540–14552, 2019.
[311] G. Zengin, M. Wersall, S. Nilsson, T. J. Antosiewicz, M. Kall, and T. Shegai, "Realizing strong light-matter interactions between single-nanoparticle plasmons and molecular excitons at ambient conditions," *Phys. Rev. Lett.*, vol. 114, p. 157401, 2015.
[312] H. Leng, B. Szychowski, M. C. Daniel, and M. Pelton, "Strong coupling and induced transparency at room temperature with single quantum dots and gap plasmons," *Nat. Commun.*, vol. 9, p. 4012, 2018.
[313] Y. Zou, G. Song, R. Jiao, G. Duan, and L. Yu, "Strong coupling between a quasi-single molecule and a plasmonic cavity in the trapping system," *Nanoscale Res. Lett.*, vol. 14, p. 74, 2019.
[314] C. Ciracì, R. Jurga, M. Khalid, and F. Della Sala, "Plasmonic quantum effects on single-emitter strong coupling," *Nanophotonics*, vol. 8, pp. 1821–1833, 2019.
[315] C. E. Petoukhoff, K. M. Dani, and D. M. O'Carroll, "Strong plasmon-exciton coupling in Ag nanoparticle-conjugated polymer core-shell hybrid nanostructures," *Polymers*, vol. 12, 2020, https://doi.org/10.3390/polym12092141.
[316] T. P. Rossi, T. Shegai, P. Erhart, and T. J. Antosiewicz, "Strong plasmon-molecule coupling at the nanoscale revealed by first-principles modeling," *Nat. Commun.*, vol. 10, p. 3336, 2019.
[317] X. C. Yu, B. B. Li, P. Wang, et al., "Single nanoparticle detection and sizing using a nanofiber pair in an aqueous environment," *Adv. Mater.*, vol. 26, pp. 7462–7467, 2014.
[318] J. D. Swaim, J. Knittel, and W. P. Bowen, "Tapered nanofiber trapping of high-refractive-index nanoparticles," *Appl. Phys. Lett.*, vol. 103, 2013, https://doi.org/10.1063/1.4829659.
[319] N. P. Mauranyapin, L. S. Madsen, L. Booth, et al., "Quantum noise limited nanoparticle detection with exposed-core fiber," *Opt. Express*, vol. 27, pp. 18601–18611, 2019.
[320] I. Ament, J. Prasad, A. Henkel, S. Schmachtel, and C. Sonnichsen, "Single unlabeled protein detection on

individual plasmonic nanoparticles," *Nano Lett.*, vol. 12, pp. 1092–1095, 2012.
[321] P. Zijlstra, P. M. Paulo, and M. Orrit, "Optical detection of single non-absorbing molecules using the surface plasmon resonance of a gold nanorod," *Nat. Nanotechnol.*, vol. 7, pp. 379–382, 2012.
[322] S. S. Acimovic, M. A. Ortega, V. Sanz, et al., "LSPR chip for parallel, rapid, and sensitive detection of cancer markers in serum," *Nano Lett.*, vol. 14, pp. 2636–2641, 2014.
[323] J. Zhu, S. K. Ozdemir, Y.-F. Xiao, et al., "On-chip single nanoparticle detection and sizing by mode splitting in an ultrahigh-Q microresonator," *Nat. Photonics*, vol. 4, pp. 46–49, 2009.
[324] M. L. Gorodetsky, A. A. Savchenkov, and V. S. Ilchenko, "Ultimate Q of optical microsphere resonators," *Opt. Lett.*, vol. 21, pp. 453–455, 1996.
[325] S. Arnold, M. Khoshsima, I. Teraoka, S. Holler, and F. Vollmer, "Shift of whispering-gallery modes in microspheres by protein adsorption," *Opt. Lett.*, vol. 28, pp. 272–274, 2003.
[326] F. Vollmer, D. Braun, A. Libchaber, M. Khoshsima, I. Teraoka, and S. Arnold, "Protein detection by optical shift of a resonant microcavity," *Appl. Phys. Lett.*, vol. 80, pp. 4057–4059, 2002.
[327] M. Baaske and F. Vollmer, "Optical resonator biosensors: molecular diagnostic and nanoparticle detection on an integrated platform," *ChemPhysChem*, vol. 13, pp. 427–436, 2012.
[328] M. R. Foreman, W. L. Jin, and F. Vollmer, "Optimizing detection limits in whispering gallery mode biosensing," *Opt. Express*, vol. 22, pp. 5491–5511, 2014.
[329] S. Subramanian, S. Vincent, and F. Vollmer, "Effective linewidth shifts in single-molecule detection using optical whispering gallery modes," *Appl. Phys. Lett.*, vol. 117, 2020, https://doi.org/10.1063/5.0028113.
[330] M. A. Santiago-Cordoba, S. V. Boriskina, F. Vollmer, and M. C. Demirel, "Nanoparticle-based protein detection by optical shift of a resonant microcavity," *Appl. Phys. Lett.*, vol. 99, 2011, https://doi.org/10.1063/1.3599706.
[331] M. A. Santiago-Cordoba, M. Cetinkaya, S. V. Boriskina, F. Vollmer, and M. C. Demirel, "Ultrasensitive detection of a protein by optical trapping in a photonic-plasmonic microcavity," *J. Biophot.*, vol. 5, pp. 629–638, 2012.
[332] M. D. Baaske, M. R. Foreman, and F. Vollmer, "Single-molecule nucleic acid interactions monitored on a label-free microcavity biosensor platform," *Nat. Nanotechnol.*, vol. 9, pp. 933–939, 2014.
[333] M. D. Baaske and F. Vollmer, "Optical observation of single atomic ions interacting with plasmonic nanorods in aqueous solution," *Nat. Photonics*, vol. 10, pp. 733–739, 2016.
[334] M. R. Foreman and F. Vollmer, "Level repulsion in hybrid photonic-plasmonic microresonators for enhanced biodetection," *Phys. Rev. A*, vol. 88, 2013, https://doi.org/10.1103/physreva.88.023831.
[335] M. R. Foreman and F. Vollmer, "Theory of resonance shifts of whispering gallery modes by arbitrary plasmonic nanoparticles," *New J. Phys.*, vol. 15, 2013, https://doi.org/10.1088/1367-2630/15/8/083006.
[336] Y. Wu and F. Vollmer, "Whispering gallery mode biomolecular sensors," in *Cavity-enhanced Spectroscopy and Sensing*, Berlin, Heidelberg, Springer, 2014, pp. 323–349.
[337] G. Schunk, J. U. Furst, M. Fortsch, et al., "Identifying modes of large whispering-gallery mode resonators from the spectrum and emission pattern," *Opt. Express*, vol. 22, pp. 30795–30806, 2014.
[338] T. B. Pittman, Y. H. Shih, D. V. Strekalov, and A. V. Sergienko, "Optical imaging by means of two-photon quantum entanglement," *Phys. Rev. A*, vol. 52, pp. R3429–R3432, 1995.
[339] R. S. Bennink, S. J. Bentley, and R. W. Boyd, ""Two-Photon" coincidence imaging with a classical source," *Phys. Rev. Lett.*, vol. 89, p. 113601, 2002.
[340] A. Valencia, G. Scarcelli, M. D'Angelo, and Y. Shih, "Two-photon imaging with thermal light," *Phys. Rev. Lett.*, vol. 94, p. 063601, 2005.
[341] F. Ferri, D. Magatti, A. Gatti, M. Bache, E. Brambilla, and L. A. Lugiato, "High-resolution ghost image and ghost diffraction experiments with thermal light," *Phys. Rev. Lett.*, vol. 94, p. 183602, 2005.
[342] B. I. Erkmen and J. H. Shapiro, "Ghost imaging: what is quantum, what is not," arXiv:quant-ph/0612070, 2006.
[343] A. Meda, E. Losero, N. Samantaray, et al., "Photon-number correlation for quantum enhanced imaging and sensing," *J. Opt.*, vol. 19, 2017, https://doi.org/10.1088/2040-8986/aa7b27.
[344] P. A. Morris, R. S. Aspden, J. E. Bell, R. W. Boyd, and M. J. Padgett, "Imaging with a small number of photons," *Nat. Commun.*, vol. 6, p. 5913, 2015.
[345] S. Lloyd, "Enhanced sensitivity of photodetection via quantum illumination," *Science*, vol. 321, pp. 1463–1465, 2008.
[346] S. H. Tan, B. I. Erkmen, V. Giovannetti, et al., "Quantum illumination with Gaussian states," *Phys. Rev. Lett.*, vol. 101, p. 253601, 2008.
[347] E. D. Lopaeva, I. Ruo Berchera, I. P. Degiovanni, S. Olivares, G. Brida, and M. Genovese, "Experimental realization of quantum illumination," *Phys. Rev. Lett.*, vol. 110, p. 153603, 2013.
[348] G. B. Lemos, V. Borish, G. D. Cole, S. Ramelow, R. Lapkiewicz, and A. Zeilinger, "Quantum imaging with undetected photons," *Nature*, vol. 512, pp. 409–412, 2014.
[349] F. Pepe, F. Di Lena, A. Garuccio, G. Scarcelli, and M. D'Angelo, "Correlation plenoptic imaging with entangled photons," *Technologies*, vol. 4, 2016, https://doi.org/10.3390/technologies4020017.
[350] F. M. Di Lena, F. Pepe, A. Avella, et al, "Correlation plenoptic imaging with entangled photons," in *Quantum Technologies 2018*, Strasbourg, France, SPIE, 2018.
[351] T. Gregory, P.-A. Moreau, E. Toninelli, and M. J. Padgett, "Imaging through noise with quantum illumination," arXiv: 1907.09370 [quant-ph], 2019, https://doi.org/10.1364/qim.2019.t5a.65.
[352] G. Scarcelli and S. H. Yun, "Entangled-photon coincidence fluorescence imaging," *Opt. Express*, vol. 16, pp. 16189–16194, 2008.
[353] A. R. Guzman, M. R. Harpham, O. Suzer, M. M. Haley, and T. G. Goodson, 3rd, "Spatial control of entangled two-photon absorption with organic chromophores," *J. Am. Chem. Soc.*, vol. 132, pp. 7840–7841, 2010.
[354] T. Ono, R. Okamoto, and S. Takeuchi, "An entanglement-enhanced microscope," *Nat. Commun.*, vol. 4, p. 2426, 2013.
[355] R. Tenne, U. Rossman, B. Rephael, et al., "Super-resolution enhancement by quantum image scanning microscopy," *Nat. Photonics*, vol. 13, pp. 116–122, 2018.

[356] J. M. Cui, F. W. Sun, X. D. Chen, Z. J. Gong, and G. C. Guo, "Quantum statistical imaging of particles without restriction of the diffraction limit," *Phys. Rev. Lett.*, vol. 110, p. 153901, 2013.
[357] D. Gatto Monticone, K. Katamadze, P. Traina, et al., "Beating the Abbe diffraction limit in confocal microscopy via nonclassical photon statistics," *Phys. Rev. Lett.*, vol. 113, p. 143602, 2014.
[358] O. Schwartz, J. M. Levitt, R. Tenne, S. Itzhakov, Z. Deutsch, and D. Oron, "Superresolution microscopy with quantum emitters," *Nano Lett.*, vol. 13, pp. 5832–5836, 2013.
[359] M. P. Landry, P. M. McCall, Z. Qi, and Y. R. Chemla, "Characterization of photoactivated singlet oxygen damage in single-molecule optical trap experiments," *Biophys. J.*, vol. 97, pp. 2128–2136, 2009.
[360] S. Waldchen, J. Lehmann, T. Klein, S. van de Linde, and M. Sauer, "Light-induced cell damage in live-cell super-resolution microscopy," *Sci. Rep.*, vol. 5, p. 15348, 2015.
[361] U. Mirsaidov, W. Timp, K. Timp, M. Mir, P. Matsudaira, and G. Timp, "Optimal optical trap for bacterial viability," *Phys. Rev. E - Stat. Nonlinear Soft Matter Phys.*, vol. 78, p. 021910, 2008.
[362] G. S. Atkinson, E. J. Allen, G. Ferranti, A. R. McMillan, and J. C. F. Matthews, "Quantum enhanced precision estimation with bright squeezed light," arXiv:2009.12438v1 [quant-ph], 2020.
[363] D. V. Voronine, N. Altangerel, E. S. Fry, et al., "The dawn of quantum biophotonics," in *El-Gomati M, Zubairy MS. Optics in Our Time*, M. D. Al-Amri, Ed., Cham, Springer International Publishing, 2016, pp. 147–176.
[364] D. S. Simon, "Quantum sensors: improved optical measurement via specialized quantum states," *J. Sens.*, vol. 2016, pp. 1–13, 2016.
[365] S. Asaad, V. Mourik, B. Joecker, et al., "Coherent electrical control of a single high-spin nucleus in silicon," *Nature*, vol. 579, pp. 205–209, 2020.
[366] N. Zhao, J. L. Hu, S. W. Ho, J. T. Wan, and R. B. Liu, "Atomic-scale magnetometry of distant nuclear spin clusters via nitrogen-vacancy spin in diamond," *Nat. Nanotechnol.*, vol. 6, pp. 242–246, 2011.
[367] N. Zhao, J. Honert, B. Schmid, et al., "Sensing single remote nuclear spins," *Nat. Nanotechnol.*, vol. 7, pp. 657–662, 2012.
[368] Z. Wang, N. Wang, Z. Li, F. Xiao, and J. Dai, "Human high intelligence is involved in spectral redshift of biophotonic activities in the brain," *Proc. Natl. Acad. Sci. U. S. A.*, vol. 113, pp. 8753–8758, 2016.
[369] P. Zarkeshian, S. Kumar, J. Tuszynski, P. Barclay, and C. Simon, "Are there optical communication channels in the brain?" arXiv: 1708.08887 [physics.bio-ph], 2017.
[370] S. Shi, P. Kumar, and K. F. Lee, "Generation of photonic entanglement in green fluorescent proteins," *Nat. Commun.*, vol. 8, p. 1934, 2017.
[371] J. Klatzow, J. N. Becker, P. M. Ledingham, et al., "Experimental demonstration of quantum effects in the operation of microscopic heat engines," *Phys. Rev. Lett.*, vol. 122, p. 110601, 2019.